Università degli Studi di Siena

Dipartimento di Scienze Fisiche, della Terra e dell'Ambiente
Sezione di Fisica

Development of a Solid-State Imaging Probe for Radio-Guided Surgery

Tesi di Dottorato di Ricerca in Fisica Sperimentale
In Partial fulfillment of the Requirements for the Ph. D. Degree in Experimental Physics

Candidate
Arta Sulaj
ARTA SULAJ
Signed 22/09/2021

Supervisor and Tutor
Pier Simone Marrocchesi

Ciclo di Dottorato XXXII

Contents

Abstract

This thesis describes the development and the characterisation of a novel CMOS digital imaging sensor for the detection of ionizing radiation and its prototypal implementation in a handheld instrument (beta probe) providing, in real time, high resolution images of a radiation field containing localized β^- - sources. One of the possible applications of the beta probe is radioguided surgery (RGS) where a radioisotope is administered to the patient and a scan of the surgery field is performed along a safety margin around the resection.

In the first chapter a short review is given of the state-of-the-art of RGS and of other complementary imaging techniques employed as advanced diagnostic tools.

The second chapter describes the working principle of the new sensor, a pixelated double-layered CMOS device allowing in-pixel coincidence between pairs of vertically integrated pixels. The characterization of the first sensor prototype and the results obtained with laboratory tests and with a dedicated particle beam test are also reported, together with a description of the second version of the sensor and of the first prototypes of the beta probe, which were developed by the ASAP collaboration, within the framework of the R&D activities supervised by the Scientific Commission 5 of INFN (Istituto Nazionale di Fisica Nucleare).

The following chapter describes a thorough simulation which was implemented in GEANT4 to study the expected performance of the probe under different conditions in a realistic scenario of RGS, mimicking the spatial distribution and activity of a set of discrete sources, and taking into account tissue absorption.

Chapter four describes a set of measurements that were carried out in our laboratory where the probe was tested using a radioactive source and the dark count rate was measured under a number of different conditions.

Finally, some preliminary conclusions are drawn on the detector performance and on the expected improvements with more advanced versions of the sensor and probe. Also, the limitations to the application of this technique in RGS, mainly driven by the maximum dose that can be administered to the patient, are discussed.

Chapter 1

Introduction to Radioguided Surgery

The precise localization and complete surgical removal of all, or part, of an organ or tissue is a well established invasive procedure in the treatment of cancer. To avoid recurrences, it is very important to remove all the malignant tissue during surgery. Because of that, usually surgeons define a safety margin surrounding the tumorous tissue and the resection is done around this margin. The excised sample is then sent to the pathology labs for a check of the presence of tumor cells. Unfortunately, the response of the pathologist is not always negative. It is possible to have a more efficient surgical treatment using preoperative imaging information. Anatomical and/or functional imaging modalities like computed tomography (CT), magnetic resonance imaging (MRI), ultrasound and molecular imaging modalities, as well as single-photon emission computed tomography (SPECT) and positron emission tomography (PET) have become standard tools to help in the diagnosis, monitoring and treatment. Patient scans usually provide 3D map of the disease (placed in the context of the patient's anatomy) that surgeons can use as reference and guidance during an intervention [1]. These advanced imaging techniques can be used for tracking (the tumoral volume and the surgical tools) and in clinical applications, like needle placement, navigated resection, etc. Due to their relative high cost, complicated logistic, large volume, and long acquisition times, these imaging system have some difficulties in the widespread adoption in clinical settings. Therefore, freehand tracking imaging may prove to be a more viable intraoperative imaging solution. One of these techniques is radioguided surgery (RGS). During surgery tracers are used mainly aid in the detection of the target structures and better identify their borders (usually using SPECT and PET imaging). So, radioguided surgery consists in the concept of utilizing a radiation detection device in the surgery room in a real-time configuration to identify regions with a higher concentration of radioisotope that has been administrated to a patient, providing the surgeon with critical and real-time information regarding the exact location of the desease. Since its first proposal in the 1940s, the use of radioguided surgery has evolved into a well-estabilished discipline in the practice of surgery. This method has significantly revolutionized the surgical management of various diseases, as breast cancer, melanoma, and parathyroid disease. Radioguided surgery allows the surgeon to minimize the degree of surgical invasiveness associated with many commonplace diagnostic and therapeutic surgical procedures, while still maintaining maximum treatment-related benefits to the patient [2].

1.1 Physics of radioguided surgery

Radioguided surgery requires a significant amount of technology for its implementation. In particular the measurement apparatus consists of the radioisotope, the compound that contains the labeled marker and the radiation detector. The radioisotope must have suitable chemical properties to form a stable labeled compound, an appropriate half-life and the emitted radiation must be compatible with the employed detector and the patient safety. The compound needs to be extracted from the blood into the tumor and the amount in the tumor has to be significantly higher than in the surrounding tissue. Furthermore, it must be extracted into and remain in the tumor with a time course that is consistent with the requirements of the surgery and the half-time of the isotope. At last but not least, the detector system needs to have a high detection efficiency of the emitted radiation, insensitivity to background radiation, good energy resolution to discriminate against background radiation, collimation to shield against background radiation and a good spatial resolution to resolve tumor from adjacent background tissue [3].

1.1.1 Half-lives

Considering the use of radioactive drugs for both diagnostic and therapeutic purposes, there are three half-lives that are important: physical, biological end effective one. The physical and biological half-lives are important since they relate directly to the disappearance of radioactivity from the body by two separate pathways (respectively, radioactive decay and biological clearance). Instead the effective half-life takes into account not only elimination from the body but also the radioactive decay. This half life is used when there is a question about residual activity in the body or in radiation dosimetry calculations. In the next subsections there is a short description of each the three half-lives.

1.1.1.1 Physical half-life

Radioactivity is a manifestation of the weak nuclear force and it is a process in which a nucleus of an unstable atom transforms into a more stable one by releasing energy in the form of particles and/or photon radiation. A common representation of stable and unstable nuclides is the mass/atomic number plot (Fig. 1.1), where all existing nuclides are plotted and marked according to the main decay modes.

According to quantum theory, the probability that a single radioactive atom decay follows a exponential law. In general, the number of radioactive atoms N(t) at time t, with an amount $N(t_0)$ at a given initial time point t_0 is given by

$$N(t) = N(t_0) \cdot e^{-\lambda t}$$

where the rate of decays per second (λ) of a radioactive material is its activity and is characteristic for each nuclide. There is a connection between this physical quantity and another one called half-life ($T_{\frac{1}{2}}$) that is the time required for the number of radioactive atoms N to decrease to one half of its initial value:

$$N(T_{\frac{1}{2}}) = \frac{N(0)}{2}$$

and the relationship between λ and half-life time $T_{\frac{1}{2}}$ is:

$$\lambda = \frac{ln2}{T_{\frac{1}{2}}}$$

In the SI system, the unit used to denote one decay per second is the *Becquerel* (Bq), in honor of the discoverer of radioactivity, and the older (but still used) unit *Curie* (Ci), in honor of Marie and Pierre Curie who were pioneers in the understanding of radioactivity. The equivalence among these units is: 1 Ci = 3.7 $\cdot 10^{10}$ Bq. Typical radioactivity values in radioguided surgery range from kBq to MBq or μCi to mCi.

The range of physical half-lives is boundless. There are isotopes with half-lives of nsec, μsec, msec, sec, hr, min, days, weeks, months, years, centuries, millennia and even as long as a billion years (half-life of ^{40}K= 1.28 $\cdot 10^9$ years). Most of those time units would not be very useful for diagnostic or therapeutic studies. The isotopes useful in this field and commercially available range from 75 sec (^{82}Rb) to 50.5 days (^{89}Sr) with all others in between those two values.

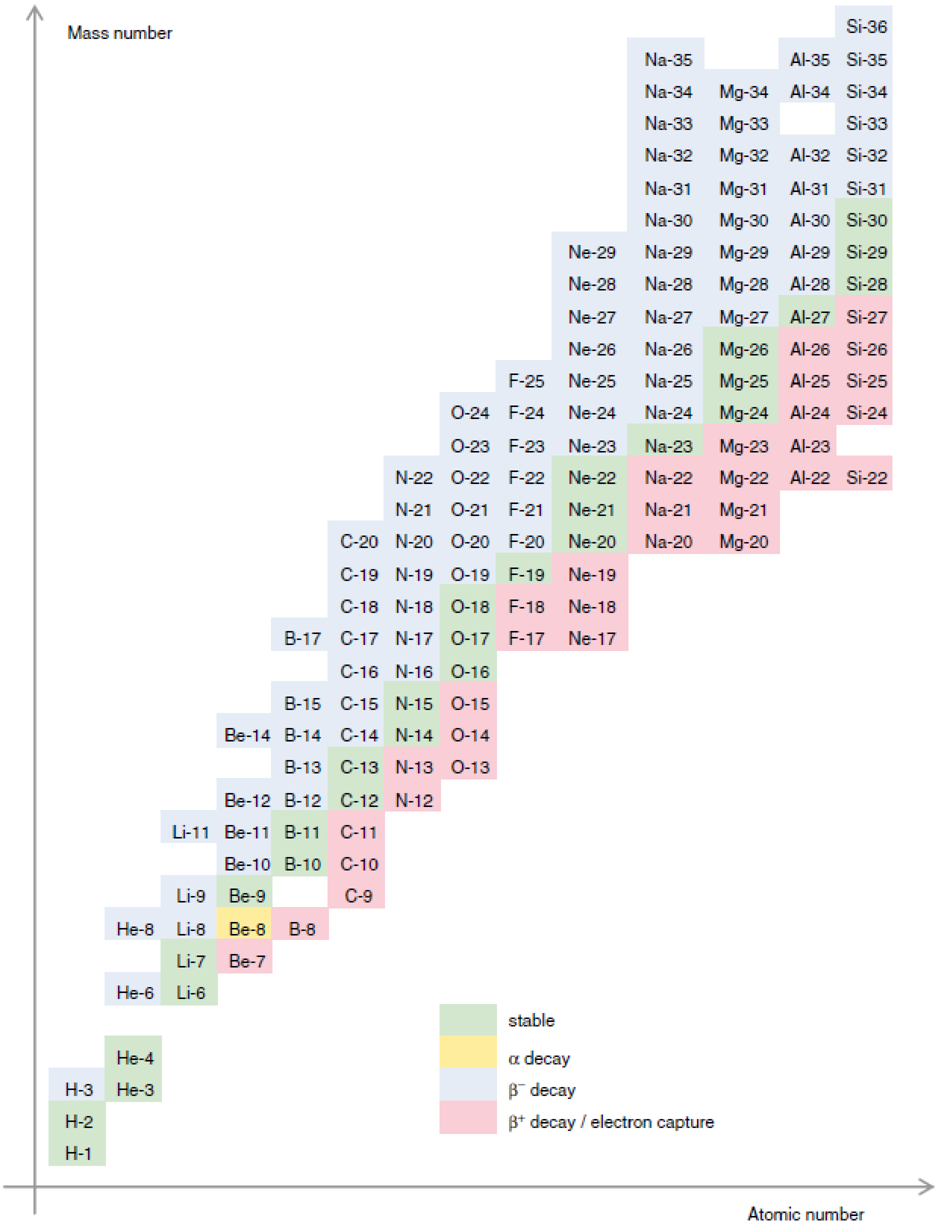

Figure 1.1: Mass/atomic number plot for the first 15 elements of the periodic table. In the abscissa axis is shown the atomic number and the ordinate axis there is the mass number. The different colours indicate the main decay mode of the corresponding nuclide [4].

1.1.1.2 Biological half-life

The biological half-life (t_{biol}) is the period of time required to reduce the amount of a drug in an organ or the body to one half its original value due only of the biological elimination. This concept is used when the rate of removal is roughly exponential. Typically, the biological half-life refers to the body's natural clearance mediated by the activity of the liver and through the excretion of a given substance through the kidneys and intestines. For radioactive compounds, it is necessary to calculate the biological half life because the mass of the isotope is usually on the nanogram (ng) scale, when distributed throughout the body concentrations are in the picogram/ml (pg/ml) range, especially in the target organ, much too small to measure directly. Instead, for non-radioactive compounds, it is possible to measure it directly. For example, assuming that a person is not allergic to a specific drug (e.g penicillin), we could give 1,000 mg of the drug and then measure the amount present in the blood pool and in the urine since it is administered such a large amount of the drug. Biological half-life for commercially available radiopharmaceuticals is typically in the range of sec (ventilation study) to days (phosphate based bone agents). The two most important external factors that affected it are hepatic and renal function. If kidneys are not working well, there will expect to see a high background activity on the scans. Also important is level of hydration: a poorly hydrated patient, even with normal renal function, will have a high background activity since limited urine is being produced, making it difficult to eliminate isotope that has not localized in the target organ. Each individual organ in the body has its own biological half time and the whole body also has its own, representing the weighted average of all internal organs and the blood pool. It is therefore very important to have a frame of reference, usually, drug package inserts often refer to the half-time of clearance of a drug from the blood pool or through the kidneys.

1.1.1.3 Effective half-life

The effective half life (t_{eff}) is defined as the period of time required to reduce the radioactivity level of an internal organ or of the whole body to exactly one half its original value due to both elimination and decay. It can be measured directly, for example, using a detection device at a fixed position to count the patient multiple times until the reading decreases to half of the initial reading. The range of t_{eff} typically varies from sec to hours and it is affected by the same external factors that affect the biological one since they are dependent. The mathematical relationship of these three half-lives is:

$$\frac{1}{t_{eff}} = \frac{1}{t_{phys}} + \frac{1}{t_{biol}}$$

and it is used to mathematically solve for the desired half-life, but there are three special cases that help to clarify the concept of effective half-life:

- if t_{phys} » t_{biol} then $t_{eff} \simeq t_{biol}$

  e.g ^{133}Xe for pulmonary ventilation study, where t_{phys} = 5.3 days and t_{biol} = 15 sec, the study is over within a few minutes. The physical half-life is so long compared to the biological one, so the effective half-life equals the biological one.

- if t_{biol} » t_{phys} then $t_{eff} \simeq t_{phys}$

  e.g. ^{99m}Tc compound for a liver scan (Tc-SC), where t_{phys} = 6.0 h and t_{biol} = infinitely long, because Tc-SC never clear the liver. So, the only half-life that matters is the physical one.

- if $t_{biol} = t_{phys}$ then t_{eff} = $\frac{t_{phys}}{2}$ = $\frac{t_{biol}}{2}$

  e.g Tc-MMA, a ^{99m}Tc compound for pulmonary perfusion imaging, t_{phys} = 6 h, t_{biol}= 6 h, then t_{eff} = 3 h.

1.1.2 Statistics

Radioactive decay is a random process and therefore statistical fluctuations occur in the measured counts or count rates arising from radioactive decays. Thus, if an intraoperative probe is used to repeatedly measure the counts (or the count rates) due to the activity of a tumor volume slightly different values are recorded during subsequent measurements. According to the Poisson distribution, if a given measurement yields N counts, the standard deviation, σ, of the number of counts is:

$$\sigma = \sqrt{N}$$

and the percentage standard deviation is:

$$\%\sigma = \frac{100\%}{\sqrt{N}}$$

If the number of measurements is large, the distribution of the count measurements approximates a Gaussian distribution, and therefore 68%, 95%, and 99% of the measurements will lie, respectively within 1 standard deviation $(N \pm \sigma)$, 2 standard deviations $(N \pm 2\sigma)$ and 3 standard deviations $(N \pm 3\sigma)$ of the mean value. If N counts are recorded during a measuring time Δt, the average counting rate during that interval is:

$$R = \frac{N}{\Delta t}$$

and the uncertainty in the counting rate R is:

$$\sigma_R = \sqrt{\frac{R}{\Delta t}}$$

If the count rate measured over a target region (eg, tumor volume) is R_g, the background count rate R_b and the counting interval Δt, the standard deviation of the target-region net count rate, $R_n = R_g - R_b$, is:

$$\sigma_{R_n} = \sqrt{\frac{1}{\Delta t}}\sqrt{R_g + R_b} \tag{1.1}$$

based on the propagation of the error associated with the measured target count rates and background count rate.

Suppose two samples are recorded with counts N_1 and N_2, respectively. The difference (N_1–N_2) may be due to an actual difference between sample activities or may be simply the result of random variations in counting rates. There is no way to know with absolute certainty that a given difference is or is not caused by random error. However, it is possible to evaluate the "statistical significance" of the difference by comparing it with the expected random error.

In general, differences of less than 2σ [i.e., $(N_1 - N_2) < 2\sqrt{N_1 + N_2}$] are considered to be of marginal or no statistical significance because there is at least a 5 % chance that such a difference is simply caused by random error. Differences greater than 3σ are considered significant (<1% chance caused by random error), whereas differences between 2σ and 3σ are in a questionable category, perhaps deserving repeated measurements or longer measuring times to determine their significance [5]. So it is possible to assess statistical significance of the measurements by the comparison of the observed difference to the expected random error.

In particular, lets see the effect of the background. All nuclear counting instruments have background counting rates, caused by electronic noise, detection of cosmic rays, natural radioactivity in the detector itself, etc. From the equation 1.1, the uncertainty in R_n is:

$$\sigma_{R_n} = \frac{\sqrt{R_g + R_b}}{\sqrt{\Delta t}} \tag{1.2}$$

replacing $R_g = R_n + R_b$ in 1.2, the standard deviation of the target-region net count rate (R_n) can be written as:

$$\sigma_{R_n} = \frac{\sqrt{R_n + 2R_b}}{\sqrt{\Delta t}} \tag{1.3}$$

The minimum detectable activity (MDA) of a radionuclide for a particular counting system and counting time Δt is the activity that increases the recorded counts by an amount that is statistically significant in comparison with random variations in background counts that would be recorded during the same measuring time. In this instance, statistically significant means a counting rate increase of 3σ [5]. Therefore, the counting rate for the MDA is:

$$MDA = 3\sigma_{R_b} = 3\sqrt{\frac{R_b}{t}} \tag{1.4}$$

Knowing the background counting rate of the detector (R_b) that is used (measured in cps or cpm), the sensitivity of the detector (S_d), measured in cps/Bq or cpm/Bq, and the time of acquisition (t), the MDA can be expressed in Bq, using 1.4:

$$MDA = 3S_d \cdot \sqrt{\frac{R_b}{t}} \tag{1.5}$$

So, in 1.4 the MDA is measured in counts and in 1.5 in Becquerel.

To determine the target net count rate (in cps), $R_n = R_g - R_b$, necessary to achieve a given statistical confidence, that is, a given net count-rate percent uncertainty $\%\sigma_{R_n}$. The counting interval time (in sec) $\Delta t_{\%\sigma}$ for both the target and the background count rate measurements is:

$$\Delta t_{\%\sigma} = \frac{r+1}{\frac{R_g}{r}(r-1)^2}\left(\frac{100\%}{\%\sigma_{R_n}}\right)^2 \tag{1.6}$$

or

$$\Delta t_{\%\sigma} = \frac{r+1}{R_b(r-1)^2}\left(\frac{100\%}{\%\sigma_{R_n}}\right)^2 \tag{1.7}$$

where r is the target gross count rate-to-background count rate ratio (often referred to as the “tumor-to-background ratio”):

$$r = \frac{R_g}{R_b}$$

Applying a given percentage uncertainty (e.g. $\%\sigma_{R_n}$ = 5%) the equation 1.6 or 1.7 can be used to calculate, as a function of the target gross count rate-to-background count rate ratio and the target gross count rate, the minimum target and background counting intervals (in seconds) to reliably detect the target.

As the count rate ratio and the target gross count rate increase, it takes less time to acquire a sufficient number of counts to achieve a statistically significant difference between the target and the background count rates.

Instead of using equal counting times for the sample and background measurements, using different collection times could be statistically advantageous. The difference between two counting rates R_g and R_b (the gross sample and background counting rate, that are estimated from preliminary measurements) is determined with the smallest statistical error if the total counting time $t = t_b + t_g$ is divided according to:

$$\frac{t_g}{t_b} = \sqrt{\frac{R_g}{R_b}} \tag{1.8}$$

If $R_g \sim R_b$, approximately equal counting times are preferred; however, if the background counting rate is small $R_b << R_g$ it is better to devote most of the available time to counting the sample. Thus a small statistical advantage is gained by using an optimal division rather than equal counting times (e.g. if r=9, using equation 1.6 , the percentage uncertainty in R_n becomes 4.5 % instead vs 5.0 % if are used different counting times according to 1.8, instead of equal times).

1.1.3 Radiation detection in the human body

The principles of the radioactivity and its interaction with matter govern the way in which radiation is emitted and emerge from the patient and explain the process of detection, a key part of radioguided surgery. In order to avoid injuries to incorrect structures and unnecessary extension of the search for hot lesions, it is vital that surgeons have an understanding of the major effects of radiation in the body and the potential pitfalls arising from the underlying physics. Since the task of radioguided surgery is to detect radioactive sources in the human body, the effects to be considered can be distinguished according to the type of emission traced. The effect of geometry is, however, common for all types of radiation. Approximately, the amount I_D of radiation that a detector of diameter D receives from a source of intensity I_0 placed at a distance d is proportional to the quotient of their squares:

$$I_D \propto I_0 \cdot \frac{D^2}{d^2}$$

so the farther away the source is, the less radiation will be detected. It is still necessary for the surgeon to know approximately how deep is necessary to go as small faint sources of activity may be detectable only at a close distance. This effect is purely geometric and is called, in the radioguided surgery jargon, the solid angle effect.

The radioguided procedures are based on γ, X-ray and β particles detection. Independent of the origin of the γ rays (γ decay, bremsstrahlung, or annihilation of β^+ particles) or the type of detector (γ probe or γ camera), the main interactions of γ or X-ray radiation with matter are absorption and scatter.

Absorption due to the photoelectric effect and geometry explains why sources in tissue farther away from the detector seem less active than closer sources with the same activity and solid angle. Because of, the density of tissue is significantly lower than the densities of the collimator and detector materials, in tissue, the attenuation due to it, is not as high as in shielding material, collimators, or even the detector itself, but it still has a major impact on this field.

In tissue, Compton scatter is the predominant contributor to scatter in the energy range considered (maximum few MeV), causing photons to change trajectory and lose energy. In practice this means that if a γ detector is pointed at a structure which is not radioactive, it may still show a response to radiation due to photon scatter from a nearby structure. Appropriate choice of the energy window may reduce this effect but it cannot be completely eliminated.

If β particles are to be detected at close distance (next to the solid angle effect) the sum of all interactions that the particle undergoes can be seen as the penetration. The penetration of β particles cannot be modeled easily in tissue, but a good approximation is the empiric formula of Katz and Penfold [6], where the tissue-independent range R in g/cm^2 of a β particle of energy E in MeV is given by:

$$R = \begin{cases} 0.412E^{1.265-0.0945\ln E} & 0.01 < E < 2.5MeV \\ 0.530E - 0.106 & 2.5 < E < 20MeV \end{cases}$$

The β particles have a continuous energy spectrum with an average energy at approximately one-third of the maximum energy. As a consequence, for most relevant nuclides the penetration will be only a few millimeters. A thin layer of tissue can thus cover a radioactive source, so care should be taken not to overlook radioactive target tissue if a complete resection is needed.

Radiation detectors are not particularly useful for radioguided surgery if they are not properly shielded and collimated. Shielding entails surrounding part of the detector with a strong absorbing material to avoid the radiation detection from regions at which the detector is not pointing. For γ rays, the materials most commonly used for shielding are wolfram (W) and lead (Pb). The choice between these materials depends mainly on cost, thickness, shape to be built and weight. W has a stronger stopping power than Pb (a thinner layer of wolfram is needed to stop the same amount of γ rays than lead); it is also harder and denser. However, it is significantly more expensive and harder to process. Furthermore the Pb is toxic, so it needs to be properly covered for use in medicine. Shielding is much easier for β particles: only a few millimeters of aluminium (Al) are sufficient to stop most β particles used in radioguided surgery.

Collimation is used to shape the radiation sensitive region in front of a radiation detector in the context of the detection of γ rays, since β particles follow random paths and as such cannot be collimated. Indeed it is almost impossible to determine their origin, and shaping the region where they are detected is highly complex. For gamma probes the choice of collimator involve a compromise between sensitivity and spatial resolution. The sensitivity is commonly given as the counts per second (cps) detected by the gamma probe from a source of 1 MBq situated at a certain distance. The spatial resolution is frequently given as the full-width half maximum of a point source at a certain distance. Instead for gamma cameras (2D array of detectors), collimation is a far more complex issue owing to the availability of different collimator options. In general, two types are used: parallel hole collimators and pin-hole collimators. Pinhole collimators use the concept of a camera obscura, producing a high-resolution images of close objects and magnify them, while far objects are depicted as small spots. The main problems with these collimators are their lack of sensitivity and the distortion effect, which may induce difficulties in interpretation. Parallel hole collimators are used more frequently as they do not introduce any distortion, but on the other hand, they have a limited field of view. Indeed only objects directly in front of them are seen, and these objects are trimmed if they are partly outside this field of view. So, since only parallel incoming rays are considered, sensitivity is almost not a function of distance. The choice of a particular collimator is basically dictated by the size of the organ or targed to be imaged. So, the sensitivity depends on the collimator detector geometry: in particular, the sensitivity increases as the square of the collimator hole size and decreases as the square of the hole length. Source to collimator distance is inversely quadratic related to the sensitivity of pinhole collimators and theoretically independent for a parallel-hole collimator, but in reality a minimal decrease in sensitivity due to scattering will be detected at larger distances. A high sensitivity is important in the operating room to image low activities, because the image acquisition times can be reduced using high sensitivity systems, but a good quality image is also related to the capacity of the detector to reject diffuse (scattered) photons by applying a proper energy window that mainly selects the direct gamma photons coming from the source. The energy resolution of the detector is expressed as the FWHM of the ^{99m}Tc or ^{57}Co photopeak (140 or 122 keV, respectively) and plays an important role: the lower (better) it is, the stricter the selection in photon energy can be. In conclusion, a large energy window is needed for detectors having a broad energy photopeak (large FWHM) to keep the sensitivity of the detector, but, a larger energy window will misinterpreted scattered photons for direct photons and therefore reduce the contrast and overall quality of your image.

The spatial resolution of a system can be expressed as intrinsic and extrinsic resolution. The intrinsic resolution refers to how well the detector localizes an interaction (in the scintillator or semiconductor crystals or itself), instead the extrinsic resolution is a combination of the intrinsic resolution and collimator resolution. Spatial resolution, expressed as the full width at half maximum (FWHM), is linear inversely related the source to collimator distance for both pinhole and parallel hole collimators. At short distances, gamma camera systems fitted with a pinhole collimator have a higher resolution than when parallel collimators are used.

There are some pitfalls that are needed to take into account during radioguided surgery: fast measurements, fast movements, shine-through and shadowing.

The integration of the measurements over a period of time is relevant to radioguided surgery because of only minimal amounts of radioactivity are used and integration times are in the range of 0.5 – 10 s. In practice, the structures for which the surgeon is looking commonly have count rates in the range of 10–30 cps. In this case, a faint source can easily be overlooked if the detector is moved rapidly above it. For example, if a source emitting 30 cps is pointed at the source for 1 s and there is a background activity of 20 cps, there is an almost 50 % chance that a surgeon will miss it if it is used a discrimination threshold of 10 cps. Even if the discrimination threshold is only 5 cps, the likelihood of missing the source is about 15 %.

It must be considered that rapid movement can also smear the radioactivity over an area, making it impossible for the user to distinguish a faint spot over a larger low-radioactivity area. The solution is to move the detector slowly, if possible remaining for a few seconds above structures that potentially have activity. If it is expected that a low activity will be detected, then a longer integration time should be used and the detector should be held steady in the same position for the duration of this integration time.

The problem called shine-through is explained by the fact that due to improper handling of the detector, one structure is thought to be radioactive while the true radioactive structure is shining through it (Fig. 1.2). The structure that shines through does not have to be the target structure. In procedures like sentinel lymph node biopsy, a procedure in which a radioactive lymph node is extracted from the axilla, it is also possible for the injection site to be the source of the counts. Usually the real radioactive lymph node lies directly behind it and somewhat deeper.

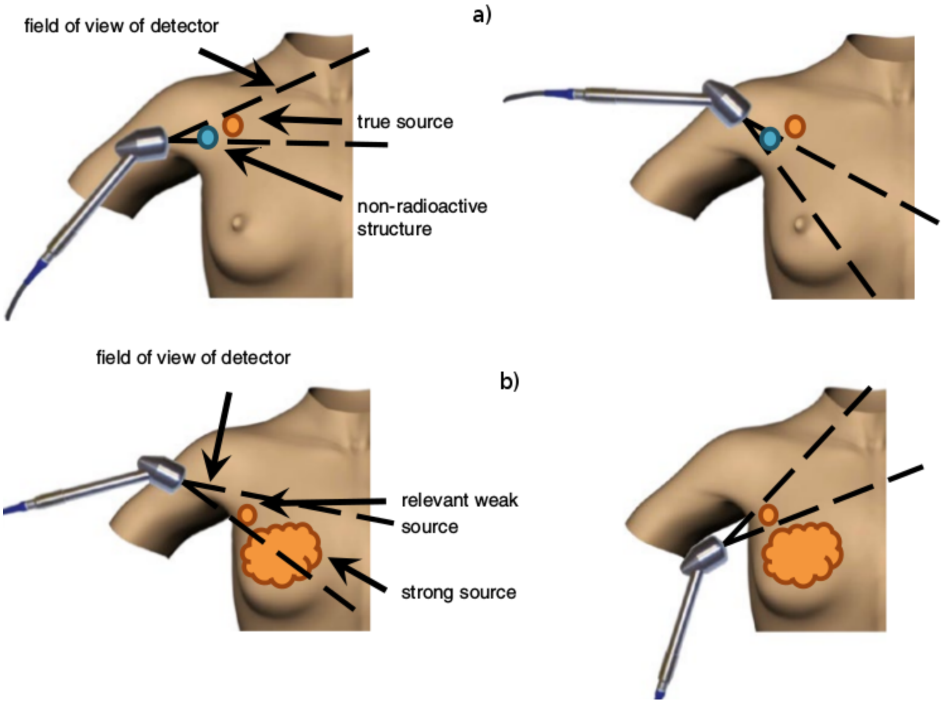

Figure 1.2: **a)**: Example of shine-through and how to avoid it. *Left*: Two structures are within the field of view of the detector, but only the deeper one is radioactive. *Right*: In order to avoid potential resection of a nonradioactive structure, the angle of the detector has to be changed such that it points away from potential sources, thereby ensuring that the structure is indeed radioactive structure, the angle of the detector has to be changed such that it points away from potential sources, thereby ensuring that the structure is indeed radioactive. **b)**: Example of shadowing and how to avoid it. *Left*: Two structures are within the field of view of the detector, but only the closer, smaller one is relevant. *Right*: In order to avoid missing this structure, the angle of the detector has to be changed such that it points away from the strong source (the strong source should not be in the field of view of the detector) before abandoning scanning of the anatomy of interest (from [4]).

The opposite effect of shine-through is the shadowing effect. In this case, a faint radioactive source is missed by the surgeon since it is too close to a hot radioactive source which shadows it. This is an extremely common occurrence in radioguided surgery as the biological uptake of structures such as the liver or activity at the injection site (in the case of sentinel lymph node biopsy) may disguise small structures that contain less radioactivity and are potentially of more importance than the shadowing structure. For both these pitfalls is to proper use, for example, the gamma detector, as well as the use of preoperative imaging, e.g., planar scintigraphy or SPECT/CT, or 3D intraoperative imaging such as freehand SPECT may help the surgeon to obtain a clearer view of the source of the radiation and thus avoid resection of a nonradioactive structure.

In general, a deeper understanding of the physics of radioguided surgery allows a good surgeon to become a good radioguided surgeon, ensuring excellent performance to the benefit of patients.

1.2 Nuclides used in radioguided surgery

The interactions of the emitted particle of the radionuclides with matter play a relevant role in the way in which the radioactive source is detected during the surgical procedure. The choice for the ideal radionuclide is based on the balance between the clinical requirements and the ability to attach the radionuclide to the tracer. For the selection of an isotope, radiation exposure of the patient and of the medical personnel is also a major factor that needs to be taken into account. The dose received by the staff may also limit the amount of procedures that they can perform on a yearly basis (Tab. 1.1) [7].

The patient dose clearly increases with increased gamma-radiation energy or by applying β-particle emitting isotopes. For example, an effective dose of 0.94 mSv for 100 MBq of ^{99m}Tc (γ energy = 141 keV) can be compared with 8.1 mSv for 150 MBq of ^{111}In (γ energy=171 and 245 keV) and 7.0 mSv for 370 MBq of ^{18}F (β^{+} energy = 634 keV) or 13 Sv for 550 MBq of ^{131}I (β^{-} energy = 606 keV, γ energy = 364 keV). A relatively higher patient dose is generally justified by the benefits that are obtained from an accurate imaging, radiation therapy and/or the radioguided surgery. Besides the advantages for a better assessment of the status of the patient, medical personnel has no obvious benefit from the chosen procedure or type of radionuclide used except for achieving an accurate resection. However, during the surgical procedures (multiple hours) they stand in close to the patient and expose themselves to tracer-based radiation.

To stay in the limits of maximum exposures (20, 5 and 1 mSv per year), the number of procedures performed by the medical personnel during a year depends from the radionuclide chosen, as it shown in the table 1.1. An important factor in these calculations is the half-life of the isotope and the time lapse between injection and the radioguided surgery procedure. When the accumulation of the radiotracer allows a longer time between injection and radioguided surgery procedure, a large reduction in the radiation exposure for medical personnel can be obtained (it is shown in the table 1.1) but on the other hand a strong signal is needed to achieve the required contrast in the image.

The radiation from the most frequently used isotopes can be grouped into three different types: γ-radiation, positron radiation and electron radiation. The isotopes that are γ-emitting

Isotope	Half time	Radiation	Energy (MeV)	Injected dose (MBq)	RGS time post injection (h)	Effective dose per patient (mSv)	Effective dose personnel (μSvh^{-1})
^{18}F	110 min	β^+	0.634	370 (FDG)	1	7	5.0
					6		5.3
				700 (FDG)	1	13.3	66.3
					6		10.0
^{32}P	14.3 days	β^-	0.690	–	–	–	–
^{57}Co	271.8 days	β^-	0.014	37	24	77.7	2.3
		γ	0.122 0.136				
^{67}Ga	3.26 days	β^-	0.084	150	6	15	3.7
		γ	0.093 0.184 0.300				
^{68}Ga	β^+	67.7 min	1.90	180	2	–	6.3
^{89}Zr	78.4	β^+	0.389	37	72	22.2	3.4
		γ	0.909				
^{90}Y	64 h	β^-	2.3	200	12	–	12.3
^{99m}Tc	6.0 h	γ	0.141	100	1	0.94	1.9
					24		0.14
				700	1	6.6	13.6
					24		0.95
^{111}In	2.80 days	γ	0.171 0.245	150	24	8.1	10.1
^{123}I	13.2 days	β^-	0.023 0.127	100	4	1.23	3.6
		γ	0.027 0.031 0.159		24		1.3
^{124}I	4.18 days	β^+	1.5, 2.1	180	168	–	9.6
		γ	0.603 1.69				
^{125}I	60.1 days	γ	0.027 0.035	7	48	1.5	0.2
^{131}I	8.02 days	β^-	0.606	100	2	14	6.5
		γ	0.364	550	24	$13 \cdot 10^3$	33.2
				4000	120	$96 \cdot 10^3$	171
^{201}Tl	73 h	γ	0.071 0.167	70	1	15.4	1.2

Table 1.1: Radionuclides clinically applied for RGS

allow whole body imaging using planar scintigraphy and/or single-photon emission tomography (SPECT). In particular the ones that emit low-to-medium energy (27-245 keV) photons (e.g.^{99m}Tc ,^{111}In and ^{125}I) have been widely used in radioguided surgery because of their: (1) availability, (2) compatibility with clinically available gamma detectors, (3) well-developed chemical procedures for introducing these nuclides into radiotracers, and (4) energy-depedent tissue attenuation. A high-energy γ-emitter has a higher tissue penetration, improving the accuracy of preoperative imaging but also results into a higher background signals during the radioguided surgery, and it needs a thickly shielded detector to improve the spatial resolution. The combination of a low-to-medium energy γ emission with a short-to-medium half-life of the radionuclide results in a limited radiation burden for both patient and medical personnel [7].

The selective detection of β paticles can improve the resolution in radioguided surgery but their use increases the radiation dose to the patient and medical personnel (mainly by positron emitters). To overcome this problem and in order to implement procedures in radioguided surgery in an everyday clinical practice it is needed to improve the specificity and the sensitivity of the imaging modalities. These improvements would allow the administration of lower dosages of these radiotracers.

In the next subsections,the main characteristics of the radiotracers used in radioguided surgery are described.

1.2.1 Gamma emmitters

The most widely applied and available γ emitter isotope is ^{99m}Tc. It has a half-life of 6h and emits photons of 141 keV. Pertechnetate ($^{99m}TcO_4^-$) can be collected from $^{99}Mo/^{99m}Tc$ generators by elution with saline and there is a range of possibilities for conjugation of this isotope to generate several radiotracers [7].

Numerous materials (organic and inorganic particles) have been applied to form radiocolloids for local injection that can be used for radioguided SLN biopsies. The ^{99m}Tc-labeled compounds can also be administered intravenously. The most simple form is the "free" ^{99m}Tc-pertechnetate that can be accumulated in the thyroid, due to its resemblance to iodine. The ^{99m}Tc-labeled bisphosphonates have been applied for radioguided biopsies and surgery of bone lesions, because of the bisphosphonates have a high affinity for the hydroxyapatite, the mineral present in bones. The ^{99m}Tc has also been conjugated to receptor targeting peptides and these radiotracers can be used for RGS of pancreatic neuroendocrine tumors and ovarian cancer.

^{111}In is a γ emitter with energy 171 and 245 keV (optimum range for commercial γ camera) and a half-life of 2.8 days. Compared to ^{99m}Tc the radiation burden (for patient and medical personnel) is higher due to the longer half-life and higher photon energy. This radionuclide is produced by proton irradiation of ^{112}Cd and can be incorporated in radiotracers via bifunctional chelates (such DTPA and DOTA). For neuroendocrine tumors, thyroid carcinoma and meningiomas are widely used ^{111}In-labeled somatostatin analogues [7].

^{57}Co mainly emits photons of 122 ad 136 keV and has a long half-life of 271.8 days. Because of its long half-life and the emission of low-energy β^--particles, the radiation burden for patient is high. This radioisotope is produced by proton irradiation of natural iron and nickel. ^{57}Co-labeled bleomycin is used for detection of lung tumors.

^{67}Ga is a γ emitter (93, 184 and 300 keV) with a half-life of 3.26 days and β^- particles; the result is a considerable radiation burden for patient. This radioisotope is produced by charge particles irradiation of ^{68}Zn. After production, the gallium is coupled with citric acid to form gallium citrate which in itself is administered as radiotracer. It is used as radiotracer to detect inflammatory lesions.

In radioguided surgery four radionuclides of iodine are utilized: ^{123}I, ^{125}I and ^{131}I that emit photons and ^{124}I that is a positron emitter. In this regard, various radiopharmaceutical agents have been developed using radionuclides of iodine in conjunction with monoclonal antibody carriers as well as receptor-specific carriers and tissue-specific carriers.

^{123}I emits photons of 27, 31 and 159 keV and β^- particles of 23 and 127 keV, with a half-life of 13.2 h. Due to its short half-life, the radiation burden is relatively low. ^{123}I is produced by proton irradiation of ^{124}Xe and the radioiodination, with all isotopes of iodine, is mainly performed by electrophilic substitution, which requires the generation of I^+ species. ^{123}I has been used for radioguided surgery for the thyroid cancer. Because ^{131}I is less expensive, better available and also often used for the therapy, this isotope often replaces ^{123}I in thyroid-related procedures.

^{125}I emits low-energy photons (35 keV) and has a half-life of 60.1 days. It is not suitable for diagnostic nuclear medicine imaging due to its low gamma photon emission energy, which results in weak tissue penetration and high soft tissue attenuation, having a poor image quality. However, its characteristics make it highly advantageous in gamma probe detection of tumor in radioguided surgery. The long physical half-life of this radioisotope has been shown to be advantageous to reach optimal pharmacokinetics and to accomplish maximal tumor localization with maximum background washout [8].

^{131}I has a physical half-life of 8 days and emits both γ and β^- radiation, respectively, of 364 and 606 keV. It is produced by neutron irradiation of natural tellurium. Because of the β^- radiation and in combination with the accumulation of the iodine in the thyroid, resulted in the therapeutic use of this isotope against thyroid malignancies. In particular in therapeutic applications for obliteration of thyroid tissue and for radioguided surgery for guiding the resection of recurrent thyroid cancer after diagnostic imaging.

^{201}Tl emits photons of 71 and 167 keV and its half-life is of 73 h. It is produced by proton irradiation of ^{203}Tl, which yields ^{201}Pb then decaying into ^{201}Tl. An intravenous injection of TlCl (Thallous chloride) has been used in one radioguided surgery case of parathyroid adenoma.

1.2.2 β^+ emitters

A prominent part of nuclear medicine, and radiochemistry, focuses on radionuclides that emits positrons in combination with positron emission tomography (PET). The emitted positrons travel a maximum of a couple of mm through human tissue before they annihilate with an electron emitting two opposite photons of 511 keV. Compared to SPECT imaging, the PET imaging has a higher sensitivity and spatial resolution. Because of these advantages, and their abundant clinical use, positron emitters been considered for radioguided surgery, even though the advantages that apply in the case of whole body imaging cannot be directly translated to radioguided surgery. Instead of the localization of high-energy photons, an interesting alternative is the selective detection of the positrons themselves. The study reported in [9] is the first demonstration of the utility of beta probes for the intraoperative detection of radiolabeled antibodies targeting cancer. In this article it is demonstrated that the beta probe may offer superior specificity for real-time localization of small tumor deposits, compared to gamma probes. In the article [9] it is found that the beta counts over sites of tumor were 2.7–6.3 times higher than background counts, whereas gamma counts were only 1.5–3.7 times higher than background counts, demonstrating the expected higher tumor specificity of the beta probe.

The most widely used β^+ emitter is 18-Fluorine (^{18}F), which has a relatively short physical half-life (110 minutes). The radioactive decay of ^{18}F is predominantly (97%) by positron emission. These emitted particles have a maximum energy of 634 keV, so they can travel only a short distance (< 2 millimeters) inside the biological tissue before they interact with an electron, to generate two high-energy photons of 511 keV. Because of the low energy of positrons the effective dose for the patient is relatively low, however, the high-energy photons result in a relatively high radiation burden for the medical personnel.

The resultant detection of ^{18}F during radioguided surgery can occur either performing a direct detection of the positrons by a positron probe or indirectly detecting the annihilation photons using a gamma probe.

This radiotracer is produced by proton irradiation of $H_2{}^{18}O$ or ${}^{18}O_2$ and can be covalently incorporated into radiotracers via nucleophilic or electrophilic introductions. The 2-Deoxy-2-${}^{18}F$ fluoro-D-glucose (${}^{18}F$-FDG) is the most widely applied tracer in modern nuclear medicine and can be used to highlight areas with a high metabolic activity, and it is used in radioguided surgery because of its widespread use and tumor accumulating characteristics.

${}^{68}Ga$ emits positrons of 1.9 MeV and has a half-life of 67.7 min. A high radiation burden can be expected based on the high-energy β^+ particles and the 511 keV photons generated by positron annihilation. For the medical personnel the radiation burden is caused by the 511 keV photons and is therefore similar for most positron emitters. This radiotracer is produced by a ${}^{68}Ge/{}^{68}Ga$ generator that can be maintained at location, e.g., a nuclear facility in a medical center. For radioguided surgery applications, similar advantages and disadvantages can be expected as described for ${}^{18}F$. From the chemical perspective, ${}^{68}Ga$ can, however, be more easily incorporated in a radiotracer via chelation by a bifunctional chelate conjugated to the targeting moiety. Due to the requirement of a chelate in combination with a short half-live, ${}^{68}Ga$ has been predominantly used in combination with peptide constructs. For radioguided surgery applications this tracer incorporated in the somatostatin analogues DOTA-NOC and DOTA-octreotate (DOTA- TATE) and successfully used for gastroenteropancreatic neuroendocrine tumors.

${}^{89}Zr$ has both β^+ and γ emissions of 389 and 909 keV, respectively, and has a half-life of 78.4 h. Therefore, it has a considerable radiation burden for the patient and the radiation dose for the medical personnel is slightly higher compared to other positron emitters due to the additional γ emission. This isotope is produced by proton irradiation of ${}^{89}Y$ and can be incorporated in a radiotracer via the bifunctional chelate desferrioxamine.

In a pilot study with ${}^{89}Zr$-desferioxamine-nanocolloid for sentinel node mapping by Heuveling et al. [10], the authors claim that, by using a β selective probe, RGS based on ${}^{89}Zr$ -desferrioxamine-nanocolloid should provide a similar or better intraoperative detection, compared to ${}^{99m}Tc$ -nanocolloid, especially for localization of a sentinel node near the injection site. This was however not (yet) shown.

${}^{124}I$ emits photons of 0.6 and 1.7 MeV and positrons of 1.5 and 2.1 MeV; it has a half-life of 4.18 days. A high radiation burden can be expected based on the high-energy emissions and long half-life. It is produced by proton irradiation of ${}^{124}Te$. The conjugation chemistry for this isotope is similar to that of the other iodine isotopes.

Although ${}^{124}I$ is mainly used for PET imaging, this isotope has been applied in radioimmunoguided surgery by tracing both the positrons and the high-energy photons (511 keV) originating from ${}^{124}I$ -labeled antibodies against A33 transmembrane glycoprotein (huA33) and against carbonic anhydrase IX (cG250) [9].

1.2.3 β^- emitters

Electron-emitting radionuclides have been applied for radiosurgery for two reasons. The first reason is the clinical application of β^- emitters for radiotherapy, which allows radioguided surgery toward the residual lesion based on other emissions of the radionuclide. The second reason is the very limited range of the β^- particles in tissue.

Any uptake in nearby healthy tissue or radiation of a nearby injection site is attenuated before reaching the detector. This would result in a lower background and a better visualization of the margins around the lesion of interest. Unfortunately a (pure) β^- emitter does not allow preoperative whole body imaging for surgical planning to have an approximate location of the lesion of interest, but high-energy electrons can produce bremsstrahlung photons that can be used for SPECT imaging.

^{32}P emits electrons of 690 keV and has a half-life of 14.3 days. It is produced by neutron irradiation of ^{32}S. One of the first studies on radioguided surgery reported in 1949, applying a Geiger-Müller device, was performed with $^{32}P - PO_4^{2-}$. The accumulation and turnover of the phosphate ion were found higher in tumor tissue compared to healthy brain tissue, thereby allowing the identification of cerebral gliomas in 14 patients.

^{90}Y emits electrons of 2.3 MeV and has a half-life of 64 h. The high-energy β emission results in a high radiation burden for the patient, and therefore, this isotope is mainly used for therapeutic purposes. However, the additional X-ray generation and the use of high therapeutic dosages cause considerable radiation exposure for the medical personnel. ^{90}Y is a decay product of ^{90}Sr , which is produced upon uranium and plutonium fission. Small scale ^{90}Y generators based on ^{90}Sr have been developed, which can be used for the production of ^{90}Y with high specific activity. These generators can be operated at the local nuclear facility of medical centers. Although 90 Y is almost purely a β emitter, SPECT imaging has been performed based on bremsstrahlung, which originates from the loss of kinetic energy from the high-energy electrons resulting in the emission of photons.

^{90}Y can be incorporated in radiotracers by binding it to the bifunctional chelate DOTA, which can be conjugated to a variety of targeting moieties. Recently the use of a β-specific probe in combination with the ^{90}Y -labeled somatostatin analogue DOTA-TOC was suggested for the detection of meningioma and high-grade glioma . In this study, PET imaging was performed with ^{68}Ga -DOTA-TOC and provided quantitative information about the uptake of the tracer. Based on this information, the required dosage of ^{90}Y-DOTA-TOC was calculated to discriminate the lesion of interest from the surrounding healthy tissue with a β^- specific probe [11]. Based on this preoperative ^{68}Ga-based imaging and calculations, the authors concluded that RGS based on ^{90}Y-DOTA-TOC should be possible [11].

1.3 Navigation work flow

Navigation is a term that describes any workflow where patient scans, real time tracking and computer aided planning are combined into real time spatial information required for the orientation and the guidance to reach the target location during an intervention. With this technology is possible to precisely indicate where structures of interest are located relative to the surgical tools in 3D, even when the structures of interest are covered by tissue and cannot be seen during surgery.

The surgical removal of all, or part, of an organ, tissue or structure is very important in treating diseases like cancer to avoid recurrences. The surgeon during the complete tumour removal, has to avoid the spillage and possible spread of tumour cells. To achieve this, usually, the surgeon define a safety margin surrounding the tumour and perform the resection around this margin, removing all tissue inside the safety margin. The identification of the boundary between the diseased and healthy tissues can be addressed by the use of anatomical and/or functional imaging modalities, often combined with contrast agents, and molecular imaging modalities like single photon emission computed tomography (SPECT) and positron emission tomography (PET). Due to their relatively high price, large volume, complicated logistics and relatively long acquisition times, it is questionable if these imaging systems will find widespread adoption in clinical settings. Tracked freehand imaging may prove to be a more viable intraoperative imaging solution. Radioguided interventions are interventions that make use of tracers, especially radioactive tracers that allow for SPECT and PET imaging. Tracers mainly aid in the detection of target structures and in more precise refinement of their borders. They can be used both: preoperatively, enabling SPECT/CT and PET/CT scans, and intraoperatively, providing real-time acoustic or visual feedback from radiation.

In [1] there are identified three navigation workflow variants in clinical practice. The first variant is navigation on preoperative scans alone, which is usually seen in interventions with no significant tissue deformation during surgery. The same type of navigation can also be used to bring surgical instruments close to the target location in laparoscopic surgeries. This variant of navigation is the most straightforward and probably most widely used navigation variant, however, in some cases can become quite imprecise, especially in the later stages of an intervention, where significant tissue deformation and patient movement may have taken place. The second navigation variant combines navigation on preoperative scans with intraoperative scans. In this case, the navigation on preoperative scans only provides rough guidance, and intraoperative scans are taken, whenever more precision is needed. With the integration of intraoperative imaging into a workflow, such navigation can, however, be applied in a much broader range of settings. The last variant consists of the navigation on intraoperative scans alone. This variant has become practical with the recent emergence of tracked freehand imaging. Recall that both tracked tools and images from tracked freehand imaging are in the same coordinate system, meaning no registration between patient scans and surgical tools is required, thus leading to a simpler navigation workflow [1].

The navigation workflow consist of three main steps: preoperative imaging and planing, registration and intraoperative navigation. In figure 1.3 there is a schematic overview of a typical navigation workflow.

The tracking systems are an essential component in all navigation workflows as they define the intraoperative coordinate system during an intervention. Combined with registrations, these estimates the placement of tracked tools, patient scans and, if available, computer-aided planning in the same coordinate system. The purpose of tracking surgical tools is to determine their position relative to the patient's anatomy and the diseased tissue therein as such to better guide the surgeon during the procedure. The preoperative imaging data set (typical navigation workflow) has to be coupled to the interventional intraoperative coordinate system. To achieve this preoperative and intraoperative co-registration is to place a special tracker at the same position on the patient during preoperative imaging and during the intervention. The composition of the tracker depends on the tracking technology that will be used, because of it has to be visible both to the tracking system and easily segmented from the preoperative scan. This object has to hold enough information for the tracking system to establish all six degrees of freedom of the tracker in the space: three degrees for the position and three for the orientation. So, trackers can be attached to surgical tools or to portions of patient's anatomy. Once segmented, the position of the tracker relative to the patient can be calculated, leading to a registration between the coordinates of the patient and the tracker and the surgical tool [1].

Most navigation workflows make an implicit assumption about the body that is being tracked is a rigid body (it has exactly the same shape any time during preoperative imaging and during surgery). This assumption may sometimes be unrealistic and can lead to mistakes, because if the object being tracked is not a rigid body, the tracking approaches can be inadequate. It is always

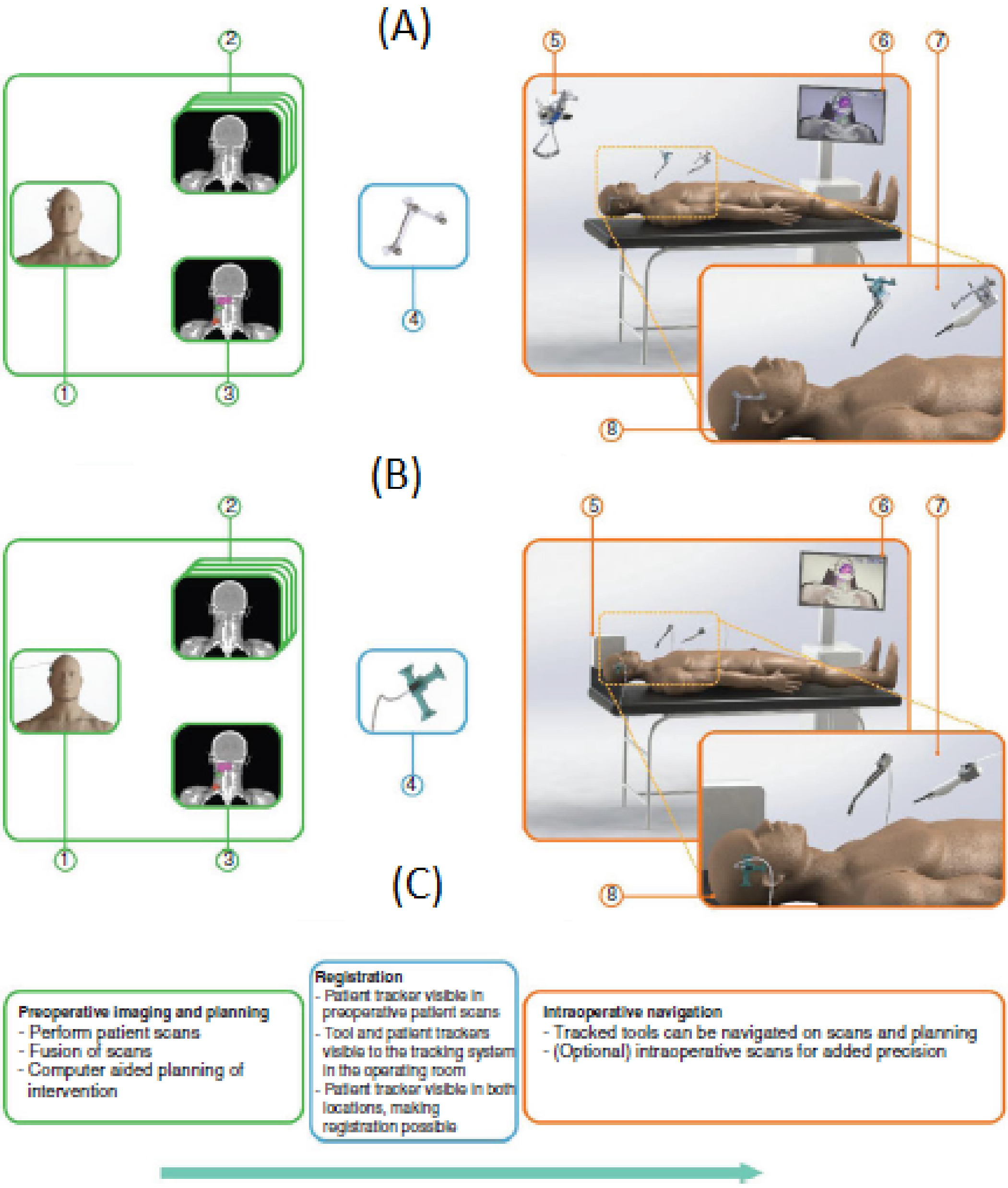

Figure 1.3: Overview of typical navigation workflow (A) ad (B) describes the tracking, respectively optical and electromagnetic one. (C) describes the sequence of steps in a typical workflow. (1) patient with tracker, (2) multiple patient scans, (3) computer-aided planning, (4) tracker visible in preoperative and intraoperative coordinate systems, (5) tracking system, (6) navigation platform, (7) tracked tools and (8) patient with tracker on the table [1].

reasonable to verify the precision of any registration between preoperative and intraoperative coordinates prior to and during an intervention. Redundant fiducials/trackers can be used to measure body deformation; if the spatial configuration changes during tracking, this information can be useful to correct tracking errors during navigation. On the other hand, images acquired with tracked freehand imaging are automatically located in the intraoperative coordinate system, rendering a registration between preoperative and intraoperative coordinates unnecessary. As a consequence, navigating tools in tracked freehand imaging scans is fairly straightforward. Intraoperative imaging can also be used to help verify the progress of a procedure, to cope with patient movement and sometimes even to quickly perform 3D intraoperative scans of the region of interest [1].

The connection between coordinate systems (i.e. preoperative with patient scans and intraoperative with tracking information), allowing objects from both coordinate systems to be shown in a single coordinate system, is called a registration. Registration methods can be separated into two types: rigid and elastic. The rigid registration consists of a composition of rotation and translation. It is relatively easy to understand, fairly simple to verify, correct, and often precise enough for the intended application, but it is limited in the degrees of freedom that it can accommodate. Registrations that can handle arbitrary deformations (random tissue movements) are called elastic or deformable registrations. Due to their complexity, these registrations cannot be described by a transformation matrix, instead, they are described by deformation fields. Elastic registrations are the topic of image analysis papers for decades already, but their use in clinical practice has been very limited thus far. The main reason for this is that there is a trade-off between flexibility (the ability to handle arbitrary deformations) and robustness (the ability to consistently yield reasonably precise registrations).

With tracking and registration we are able to see the position of the tracked surgical tools overlaid on patient scans. It is not possible to establish the distance and the preferred route towards the target only this information. Computer-aided planning software provides the navigation platform with the additional information needed to achieve both distance and route estimates, segmenting the target structure in the patient scans and providing this segmentation to the navigation platform.

There are two types of segmentations, manual and semi-automatic, that are currently the tools of choice in clinical practice. Manual segmentations require manual drawings of the contours and interior of all structures that have to be segmented and its main advantage is that the user has complete control over what label each voxel in the 3D preoperative scan gets. However, it can be extremely time consuming, especially for high-resolution 3D scans and also, it suffer from the highest interobserver variability. A semiautomatic segmentation is a manual segmentation with some automatic assistance. It requires less user input and can be performed significantly faster and with higher reproducibility than manual segmentations. A fully automatic segmentation is a segmentation that requires no user interaction. Its advantage is that it doesn't neither need to be performed nor supervised by a trained medical specialist. Experienced human operators, although usually superior to automatic methods, are subject to time constraints and susceptible to boredom, unlike machines. These are not limiting when a single segmentation of a target structure has to be performed, but can become an issue when repetitive or more extensive segmentations are required, but let's take in mind that segmentations always have to be critically evaluated by an expert.

1.4 Preoperative imaging techniques

The most advanced preoperative diagnostic imaging techniques provide the surgeon with more precise information on the location and extent of the neoplastic disease. The most used imaging techniques are: computed tomography (CT), magnetic resonance imaging (MRI), ultrasound (US), single photon emission computed tomography (SPECT), Positron emission tomography (PET), SPECT/CT and PET/CT.

Molecular imaging techniques (i.e PET, SPECT) are used to generate maps of functional and biochemical activity in target tissues in vivo providing the anatomical definition of structures. The CT and MRI images have a high spatial resolution and display the anatomy and morphological changes in great detail. Their main drawback is their low contrast resolution, as a consequence of which it is not possible to differentiate between viable tumour tissue and surgery, radiotherapy or chemotherapy related changes. In contrast, PET and SPECT have a high contrast resolution, and by supplying functional information on the biological and molecular characteristics of the tumour they help in differentiating viable tumour from treatment related changes.

PET/CT is defined as an integrated or multimodality technique that employs a combination of a PET and a CT system (that are described in the next paragraphs) with a single, conjoined patient handling system. It allows sequential acquisition of corresponding PET and CT portions of the examination with the patient in the same position for both examinations and enables co-registration both data sets. SPECT/CT cameras in which both the SPECT gamma camera system and the CT camera system have been integrated into one gantry have been available since the late 1990s. The SPECT/CT systems allow for the fusion of the nuclear medicine SPECT images with the CT images. This results in a better image showing both the physiological aspects of the disease and anatomical information. SPECT imaging allows assessment of tumour malignancy based on the functional imaging aspect, while SPECT/CT plays an important role in localisation of the tumour for the purpose of surgery. After surgery and/or radiotherapy, SPECT and SPECT/CT are used to help monitor the disease by evaluating differences at the tumour site that can indicate gliosis, radiation necrosis or tumour recurrence. SPECT permits the functional imaging of tumours of an indeterminate nature in order to evaluate their significance.

1.4.1 Computed tomography (CT)

The Computed Tomography (CT) makes use of computer-processed combinations of many X-ray measurements taken from different angles to produce tomographic images of specific areas of a scanned object. The density at a given point on an image represents the X-ray attenuation within the patient along a line between the X-ray focal spot and the point on the detector corresponding to the point on the image. Computed tomography operates by using an X ray generator that rotates around the object and the X-ray detectors are positioned on the opposite side of the circle from the source. A single transmission measurement through the patient made by a single detector at a given moment in time is called a ray. A series of rays that pass through the patient at the same orientation is called a projection or view. There are two projection geometries that have been used in CT imaging: parallel beam geometry and fan beam geometry. In the first type all the rays in a projection are parallel to each other, in the second one the rays at a given projection angle diverge and have the appearance of a fan. All modern CT scanners incorporate fan beam geometry in the acquisition and reconstruction process. The purpose of the CT scanner hardware is to acquire a large number of transmission measurements through the patient at different positions. Once the scan data has been acquired, the data must be processed using a form of tomographic reconstruction, which produces a series of cross-sectional images. After CT reconstruction, each pixel in the image is represented by a high precision floating point number ($\mu(x,y)$), but the most computer display hardware makes use of integer images. Consequently, after CT reconstruction, but before storing and displaying, CT images are normalized and truncated to integer values. The number CT(x,y) in each pixel, (x,y), of the image is converted using the following expression [12]:

$$HU(x,y) = 1000\,\frac{\mu(x,y) - \mu_{water}}{\mu_{water}}$$

where μ_{water} is the attenuation coefficient of water, and CT(x,y) is the CT number (or Hounsfield unit) that ends up in the final clinical CT image. The value of μ_{water} is about 0.195 for the x ray beam energies typically used in CT scanning. This normalization results in CT numbers ranging from about -1000 to +3000, where -1000 corresponds to air, soft tissues range from -300 to -100, water is 0, and dense bone and areas filled with contrast agent range up to +3,000. Dense material (e.g bone) can cause artifacts, which are caused by abrupt transitions between low and high density materials, which results in data values that exceed the dynamic range of the processing electronics.

The radiation dose for a particular study depends on multiple factors: volume scanned, patient build, number and type of scan sequences, and desired resolution and image quality.

1.4.2 Magnetic resonance imaging (MRI)

Nuclear Magnetic Resonance (NMR) is the spectroscopic study of the magnetic properties of the nucleus of the atom. The protons and neutrons of the nucleus have a magnetic field associated with their nuclear spin and charge distribution. Resonance is an energy coupling that causes the individual nuclei, when placed in a strong external magnetic field, to selectively absorb, and later release, energy unique to those nuclei and their surrounding environment. The detection and analysis of the NMR signal has been extensively studied since the 1940s as an analytic tool in chemistry and biochemistry research and it is not an imaging technique until in the early 1970s. Then it was realized that magnetic field gradients could be used to localize the NMR signal and to generate images that display magnetic properties of the proton, reflecting clinically relevant information [12]. Therefore this technique became magnetic resonance imaging (MRI) instead of nuclear magnetic resonance. MRI is a rapidly changing and growing image modality; its high contrast sensitivity to soft tissue differences and the inherent safety to the patient resulting from the use of non ionizing radiation have been key reasons why MRI has supplanted many CT and projection radiography methods.

Conventional MRI involves radiofrequency excitations combined with magnetic field gradients (one for each direction) to localize the signal from individual volume elements (voxels) in the patient. Magnetic field gradients are obtained by superimposing the magnetic fields of one or more coils with a precisely defined geometry and its strength varies linearly versus distance over a predefined field of view (FOV). Spatial resolution, contrast sensitivity, and signal noise ratio (SNR) parameters form the basis for evaluating the MR image characteristics. The spatial resolution is dependent on the FOV, which determines pixel size, the gradient field strength, which determines the FOV, the receiver coil characteristics (head coil, body coil, various surface coil designs), the sampling bandwidth, and the image matrix. In general, MR provides spatial resolution approximately equivalent to that of CT, with pixel dimensions on the order of 0.5 to 1.0 mm for a high contrast object and a reasonably large FOV (>25 cm). A 25 cm FOV and a 256 X 256 matrix will have a pixel size on the order of 1 mm. In small FOV acquisitions with high gradient strengths and surface coils, the effective pixel size can be smaller than 0.1 to 0.2 mm (of course, the FOV is extremely limited). Slice thickness in MRI is usually 5 to 10 mm.

Each tissue returns to its equilibrium state after excitation by the independent relaxation processes of T_1 (spin-lattice; that is, magnetization in the same direction as the static magnetic field) and T_2 (spin-spin; transverse to the static magnetic field). To create a T_1 weighted image, magnetization is allowed to recover before measuring the MR signal by changing the repetition time (TR). This image weighting is useful for assessing the cerebral cortex, identifying fatty tissue, characterizing focal liver lesions, and in general obtaining morphological information, as well as for post-contrast imaging. To create a T_2 weighted image, magnetization is allowed to decay before measuring the MR signal by changing the echo time (TE). This image weighting is useful for detecting edema and inflammation, revealing white matter lesions, and assessing zonal anatomy in the prostate and uterus.

With continuous improvements in image quality, acquisition methods, and equipment design, MRI is the modality of choice to examine anatomic and physiologic properties of the patient. There are drawbacks, including high equipment and siting costs, scan acquisition complexity, relatively long imaging times, significant image artifacts, and patient claustrophobia problems [12].

1.4.3 Ultrasound (US)

Ultrasound describes sound waves of frequencies exceeding the range of human hearing (larger than 20 kHz) and their propagation in a medium. In medical field, ultrasound imaging is a modality that uses ultrasound energy and the acoustic properties of the body to produce an image from stationary and moving tissues. It is based on the mechanical interaction of pulses of high frequency sound waves and their returning echoes, to have a gray-scale tomographic image of tissues. The generation of the sound pulses and the detection of the echoes are attained with a transducer, which also directs the ultrasound pulse along a linear path through the patient. Along a given beam path, the depth of an echo-producing structure is determined from the time between the pulse emission and the echo return. This time depends from the characteristics of the tissue in which the wave goes through and the amplitude of the echo is encoded as a gray-scale value. In particular, the wave speed is determined by the ratio of the bulk modulus and the density of the medium:

$$v = \sqrt{\frac{B}{\rho}}$$

where B, the bulk modulus, is a measure of the stiffness of a medium and its resistance to being compressed and its SI unit is $kg/(m\ s^2)$, ρ, the density in kg/m^3 and the speed of sound, v, in m/s. A highly compressible medium, such as air, has a low speed of sound, while a less compressible medium, such as bone, has a higher speed of sound. A less dense medium has a higher speed of sound than a denser medium (e.g., dry air vs. humid air). The difference in the speed of sound at tissue boundaries is a fundamental cause of contrast in an ultrasound image.

The resolution of the ultrasound image and the attenuation of the ultrasound beam energy depend on the wavelength and frequency. The ultrasound frequency is unaffected by changes in sound speed, thus the wavelength is dependent on the medium. Ultrasound wavelength determines the spatial resolution achievable along the direction of the beam. A high frequency ultrasound beam (so, a small wavelength) provides superior resolution and image detail than a low frequency beam. However, the depth of beam penetration is reduced at higher frequency, so a lower frequency ultrasound has longer wavelength and less resolution, but a greater penetration depth. Ultrasound frequencies selected for imaging are determined by the imaging application: for thick body parts (e.g., abdominal imaging), a lower frequency ultrasound wave is used (3.5 to 5 MHz) to image structures at significant depths, whereas for small body parts or organs close to the skin surface (e.g., thyroid, breast), a higher frequency is employed (7.5 to 10 MHz). Most medical imaging applications use frequencies in the range of 2 to 10 MHz and the speed of sound ranges from 300 m/s (air) to 4080 m/s (skull bone). The soft tissue has speed of sound around 1500 m/s.

Ultrasound provides to two-dimensional tomographic imaging, anatomic distance and volume measurements, motion studies, blood velocity measurements, and three-dimensional imaging.

1.4.4 Single photon emission computed tomography (SPECT)

Single Photon Emission Computed Tomography (SPECT) generates transverse images describing the distribution of x or γ ray emitting nuclides in patients. Standard planar projection images are acquired from an arc of 180 degrees (usually cardiac SPECT) or 360 degrees (most noncardiac SPECT) about the patient. The majority of SPECT systems use one or more scintillation camera heads, that revolve about the patient, acquiring projection images from evenly spaced angles. Each projection image is acquired in a computer, in frame mode heads of a

SPECT system produced ideal projection images (i.e., no attenuation by the patient and no degradation of spatial resolution with distance from the camera). Projection images from opposite sides of the patient would be mirror images and projection images over a 180 degree arc would be sufficient for transverse image reconstruction, using either filtered backprojection, as does the computer in an x ray CT system, or iterative reconstruction methods.

SPECT projection images are usually acquired in either a 64 x 64 or a 128 x 128 pixels format. Using too small a pixel format reduces the spatial resolution of the projection images. Using too few projections creates radial streak artifacts in the reconstructed transverse images. In particular, the spatial resolution deteriorates as the radius of the camera orbit increases. The camera heads on older SPECT systems followed circular orbits around the patient while acquiring images. This type of orbits is satisfactory for SPECT imaging of the brain, but cause a loss of spatial resolution in body imaging because the circular orbit causes the camera head to be many centimeters away from the surface of the body during the anterior and posterior portions of its orbit. Newer SPECT systems provide non circular orbits (also called "body contouring") that keep the camera heads in close proximity to the surface of the body throughout the orbit to have a higher spatial resolution [12].

In SPECT, attenuation greatly reduces the number of photons from activity in the half of the patient opposite the camera head, and this information is greatly blurred by the distance from the collimator. There are available approximate methods for attenuation correction. One of the most common, the Chang method, assumes a constant attenuation coefficient throughout the patient, but the attenuation is not uniform throughout the patient and, in the thorax in particular, it is very nonuniform. These approximate methods cannot compensate for nonuniform attenuation, for this reason, several manufacturers provide SPECT cameras with radioactive sources to measure the attenuation through the patient. The sources are used to acquire transmission data from projections around the patient and next the transmission projection data are reconstructed to provide maps of tissue attenuation characteristics across transverse sections of the patient, similar to X ray CT images. Finally, these attenuation maps are used during the SPECT image reconstruction process to provide attenuation corrected SPECT images [12].

The spatial resolution of a SPECT system can be measured by acquiring a SPECT study of a line source, such as a capillary tube filled with a solution of technetium ^{99m}Tc placed parallel to the axis of rotation. The National Electrical Manufacturers Association (NEMA) specifies a cylindrical plastic water filled phantom, 22 cm in diameter, containing three line sources for measuring spatial resolution. The full width at half maximum (FWHM) measures of the line sources are determined from the reconstructed transverse images. The NEMA spatial resolution measurements are primarily determined by the collimator used. The tangential resolution for the peripheral sources (typically 7 to 8 mm FWHM for low energy, high resolution and ultra high resolution parallel hole collimators) is much superior to the central resolution (typically 9.5 to 12 mm). The tangential resolution for the peripheral sources is better than the radial resolution (typically 9.4 to 12 mm) for the peripheral sources. The NEMA spatial resolution measurements fail to show the advantage of SPECT systems with two or three camera heads; double and triple head cameras will permit the use of higher resolution collimators for clinical studies than will single-head cameras [12].

Therefore, these FWHMs measured using the NEMA protocol are not necessarily representative of clinical performance, because these spatial resolution studies are done in different conditions (i.e.using longer imaging and closer orbits than would be possible in a patient). Patient studies may require the use of lower resolution (higher efficiency) collimators than the one used in the NEMA measurement to obtain adequate image statistics. In addition, the filters used before backprojection for clinical studies have lower spatial frequency cutoffs than do the ramp filters used in NEMA spatial resolution measurements .

1.4.5 Positron Emission Tomography (PET)

SPECT imaging, was introduced in the 1970s, and it enables the creation of a 3D image from multiple gamma camera images taken by cameras continuously rotating around an area of interest. The 3D images obtained using SPECT offer improved sensitivity and resolution compared with 2D images and are easier to compare with MRI and CT images. SPECT also permits better tumour localisation as the 3D imaging component allows different views (sagittal, coronal and transaxial) to be displayed, thereby offering improved visualisation of the abnormality. Both techniques are exceptionally sensitive (PET more so than SPECT); they can detect picomolar or even femtomolar concentrations of radiolabelled compounds and enable the dynamic acquisition of relatively fast kinetics (of the order of seconds for PET). For example, PET/SPECT having these properties, can facilitate the quantitative measurement of rapid physiological/pharmacological processes of biomolecules in the living brain, and other organs.

Positron Emission Tomography (PET) is imaging technique based on the detection (in coincidence) of back to back gammas produced by the annihilation of positron emitting nuclides in patients. Several rings of detectors surround the patient and the PET scanners use annihilation coincidence detection instead of collimation to obtain projections of the activity distribution in the target. The PET system's computer then reconstructs the transverse images from the projection data, as does the computer of an X ray CT or SPECT system.

There are two widely used techniques of reconstruction: Filtered Back Projection (FBP) and Maximum-Likelihood Expectation-Maximization (MLEM) algorithms.

Modern whole-body PET systems achieve a spatial resolution slightly better than 5 mm FWHM of the line spread function (LSF) in the center of the detector ring when measured by the NEMA standard. There are three factors that primarily limit the spatial resolution of PET scanners: the intrinsic spatial resolution of the detectors, the distance traveled by the positrons before annihilation, and the fact that the annihilation photons are not emitted in exactly opposite directions from each other. The intrinsic resolution of the detectors is the major factor determining the resolution in current scanners. The spatial resolution of a PET system is best in the center of the detector ring and decreases slightly (FWHM increases) with distance from the center, because of the considerable thickness of the detectors and the current PET systems cannot determine the depth in the crystal where an interaction occurs. Uncertainty in the depth of interaction causes uncertainty in the line of response for annihilation photons that strike the detectors obliquely. Photons emitted from the center of the detector ring can only strike the detectors head-on, but many of the photons emitted from activity away from the center strike the detectors from oblique angles.

1.5 Intraoperative imaging techniques

One of the most important benefits of intraoperative imaging for the surgical procedure is the assessment of remaining activity in the surgical field at the end of the procedure, in order to attempt to identify any missed tumoral volume. A strict intraoperative protocol is necessary to study how man additional volumes are found by intraoperative imaging. The operational characteristics, system sensitivity and spatial resolution, are key parameters in characterizing the performance of the detectors used for intraoperative imaging. For detecting a small amount of radioactivity from the target tissue, high sensitivity is necessary. On the other hand, to identify a small focus of activity (e.g. in a lymph node) adjacent to a larger, higher activity focus of non-specific activity (e.g. at the injection site), excellent spatial resolution is essential [13].

For example, in the sentinel lymph node (SLN) biopsy, first, the surgeon removes the SLNs by localizing them using only the gamma probe. When no further radioactive nodes are detected by the gamma probe (negative gamma probe screening), the surgical field is scanned using the portable or handheld gamma camera searching for possible “missed” radioactive lymph nodes. In the article [14] there are described the principal intraoperative imaging techniques used in the surgical tumoral field. The main techniques used are: vital dyes, portable gamma camera and hand-held probes.

1.5.1 Vital dyes

For SLN mapping, preoperative lymphoscintigraphy and intraoperative gamma-probe search combined with intraoperative blue dye injection and visual guidance has shown to be the optimum method for decreasing false negative results and for increasing sensitivity [15], [14]. Few minutes before the operation, a coloured substance is injected in proximity to the tumor; it is absorbed by the lymphatic vessels and henced by the node, that gain a blue pigment. Several studies have established the validity of blue dyes as markers for SLN mapping [16]. It has a relatively high detection rates in every clinical although slightly lower than those achieved with radiocolloids. The blue dyes cannot be seen from the skin surface, which makes them impractical as a stand-alone method and requires therefore the use of radiocolloids as well. Another disadvantage is temporary skin or areolar blue tattooing in patients with breast conservation surgery, when the dye is injected superficially. Finally, blue dyes can induce anaphylactic reactions in 0.15-2% of patients [14].

1.5.2 Gamma probes and β probes

Gamma probes for radioguided surgery require high spatial resolution and high sensitivity. The first to allow for a more precise localization of small lymph nodes, the second to obtain a radioguided surgical resection of tumors. Recent developments of hand-held gamma probes based on wireless technology eliminate the cables. Using the preoperative images and skin markings as guides, the gamma probe can be used to select the optimum location for incision [14]. After that, the surgeon uses the probe to guide dissection to the hot SLNs or radiolabeled tumor tissue and explores the surgical bed with the probe after node excision to confirm removal of the hot nodes or remaining activity. It is desirable using thin probes (e.g., 10 mm in diameter) in order to better identify the activity source in a reduced surgical space. Deeply located SLNs are difficult to detect because of tissue attenuation and because the large amount of radioactivity at the injection site may hide nearby located SLNs.

Gamma probes can also be used to localize non-palpable breast cancers or other lesions, based on the detection of previously injected radiotracers into the tissue or tumor (radioguided occult lesion localization, ROLL). Currently, there are new possibilities to explore and to be possibly integrated in this issue. An interesting development based on the hand-held probes is the combination of these intraoperative nuclear devices with position and orientation tracking systems to have a 3D visualization of the traditional acoustic signal of the gamma probe [14].

The methods used in radioguided surgery make use of γ emitted tracers and γ radiation detection probe. To extend the applicability of radioguded surgery there are exploited innovative techniques using *beta* radiation [17], [18], [19], [20] . The electrons penetrate only few mm in the tissue, resulting both in lower required radiopharmaceutical activity and the possibility to apply this technique also to cases with a large uptake of nearby healthy organs,where the approach with γ radiation suffers due to the non negligible background [21]. Low background rate is correlated with the low medical exposure to radiation too.

The hand-held probes used intraoperatively only have a single detector. It works well, and it certainly is a valuable tool, however, it presents several limitations:

- it does not provide imaging documentation for the medical record;
- its usefulness is highly dependent on correct probe positioning and thus is highly operator dependent;
- its counting rate is highly dependent on the distance between the probe tip and the radioactive source.

Imaging devices must meet several requirements to be employed in the intraoperative practice: a portable and stable design, no delay between image acquisition and display, and possibility for continuous monitoring, spatial orientation on screen, real-time quantification and display of the counts recorded [14].

1.6 Clinical applications

Radioguided surgery and especially sentinel lymph node (SLN) biopsy is currently the standard accepted standard for patients with early-stage breast cancer and cutaneous melanoma.

The sentinel lymph node (SLN) is the first lymph node draining the tumor. SLN biopsy is a widely accepted procedure in the clinical setting since it provides important prognostic information, which helps patient management, and avoids the side effects of complete lymph node dissection. The rationale of identifying and removing the SLN relies on the low probability of subsequent metastatic nodes in case of a negative histological exam performed in the SLN.

The sentinel lymph node is the hypothetical first lymph node (or group of nodes) that drains a tumoral volume. The malignant cells are transported by the lymphatic fluid from a primary tumor to a particular lymph node, where they are trapped. Such a metastasis may then generate further nodal metastases downstream through the efferent lymph vessel or may disseminate to distant sites via the bloodstream and it is postulated that the sentinel lymph node is the target organs primarily reached by metastasizing cancer cells from the tumor. The spread of some forms of cancer usually follows an orderly progression, spreading first to regional lymph nodes, then the next echelon of lymph nodes, and so on, since the flow of lymph is directional, meaning that some cancers spread in a predictable fashion from where the cancer started. In these cases, if the cancer spreads it will spread first to lymph nodes (lymph glands) close to the tumor before it spreads to other parts of the body. The concept of sentinel lymph node surgery is to determine if the cancer has spread to the very first draining lymph node (called the "sentinel lymph node") or not. If the sentinel lymph node does not contain cancer, then there is a high likelihood that the cancer has not spread to any other area of the body. The sentinel node procedure consists of the identification, removal and analysis of the sentinel lymph nodes of a particular tumour.

The sentinel lymph node procedures are used in many clinical fields. In the beginning, the SLN was pursued by visualization of the afferent lymph vessel using the blue dye technique, i.e., by tracing the blue-stained lymphatics to the lymph node after intradermal injection of blue dye at the primary melanoma site.

The primary tumor may drain through two separate lymph ducts to two different lymph nodes that may not necessarily be visualized simultaneously, although both are directly at risk of receiving tumor cells. When the dynamic process is observed during lymphoscintigraphy, it became clear that a more general definition was needed to include all eventualities. Describing the SLN as “any lymph node receiving direct lymphatic drainage from the primary tumor site” includes the metastatic node in the draining node field that was not seen on the lymphoscintigrams and was not staining blue.

However, this definition missed the pathophysiological foundation of the SLN concept. For instance, the definition of a SLN being a blue-stained node may lead to the removal of too many lymph nodes because the blue dye is not retained in a lymph node and will also stain nodes downstream that are not directly at risk of harboring tumor cells (so-called “second-tier” nodes). The definition of the SLN being the most radioactive node may lead to the removal of too few lymph nodes because separate lymphatic vessels originating in a tumor may drain to two lymph nodes, and one is likely to contain more of the tracer than the other.

The definition that reflects the physiology of lymphatic drainage and the concept of stepwise spread of cancer through the lymphatic system requires the nuclear medicine physician to perform dynamic imaging to visualize the afferent lymph vessel or vessels. The surgeon needs to have the skill and experience to find and dissect the fragile blue lymph duct through a small incision in a confined space in a lymph node basin that may be quite deep. Finding the correct node requires close cooperation from the nuclear medicine physician and the surgeon.

Chapter 2

Development of an advanced solid-state CMOS avalanche detector

This chapter is dedicated to the description of the APiX (Avalanche PiXel) detector and of the experimental conditions during a beam test at CERN and during laboratory tests for its characterization. In the following we first describe the detector concept, the characterization of the first prototype, the beam test results and the radiation tolerance tests. Then we describe the second prototype and the first implementations of an RGS probe prototype.

2.1 The APiX sensor concept

The general structure of the APiX detector consists of a pair of semiconductor layers integrated vertically to provide operation in coincidence. The detector consists of two units: a master chip and a slave chip (of smaller size) bump bonded to the former. Each chip is a pixel avalanche sensor structured into vertically aligned avalanche cells. On the first sensor layer, the avalanche cell operates in breakdown mode to detect ionizing particles. On the second layer, another avalanche sensor element, also operating in breakdown mode, independently detects the ionizing particle seen by the first avalanche sensor element. The two pixels are vertically aligned and they produce a signal in coincidence.

A logic element, electrically interconnected to the first and second avalanche sensors, processes the signal created by the coincident breakdown of the first and second avalanche sensor elements. As a consequence, the signal can be distinguished from dark count events in both sensor elements and from the signals produced by background photons. The logic determines if top and bottom avalanche cells in the APiX pixel are simultaneously activated, flagging the detection of a charged particle passing through the pixels pair. The dark counts generated by thermal electron/hole pair production are strongly suppressed by the coincidence, because the spontaneous breakdown is a stochastic process in each avalanche detector's cell.

Another possible source of background events is the optical cross-talk between adjacent pixels. During the avalanche processes, optical photons are produced which can be detected in the nearby cells, originating a signal indistinguishable from the detection of a charged particle. This effect can be overcome by implementing trenches in between adjacent pixels and filling them with optically isolating material. The trenches are narrow and occupy relative small amount of the pixel area, therefore affecting the geometrical efficiency of the detector only to a limited extent [22].

This sensor structure provides a position sensitive avalanche pixel array, including an interconnection of the two layers of the substrate, and the logic elements for providing output signals to the readout electronics. The output signals contain the information corresponding to the number and the position of pixel pairs activated during a charged particle flux exposure.

The detector operates in breakdown mode having an avalanche current increasing exponentially. The process is controlled by a high resistivity quenching element placed in series with each avalanche structure. As the current through the sensor cell increases, the voltage drop across the quenching resistor also increases until the voltage applied to the avalanche structure falls below the breakdown voltage. The negative feedback mechanism introduced by the quenching resistor causes a quenching of the avalanche process and its termination. In this configuration, the avalanche cell reaches an intrinsic gain up to 10^6. Due to the high intrinsic gain of the avalanche sensors, the detected radiation in the APiX pixel generates a pair of signals from the two aligned avalanche cells whose amplitude are well above the electronics noise.

The nature of these signals can be considered semi-digital, because the amplitude of the output signal is not defined by the number of carriers created in the sensitive volume, but defined by the avalanche process. When an ionizing particle is detected by the APiX pixel the two signals generated in the two paired avalanche pixels show only that these sensor elements were both activated. The signals are identical and independent of the energy deposited by the charged particle in the avalanche structures; they depend only on the characteristic parameters of the avalanche structure.

Using a CMOS technology the thickness of the detector is small enough to allow the ionizing radiation to penetrate across both layers and to interact in the two vertically aligned pixels.

The APiX structure is composed of an array of a few thousand of such pixels, with variable size and shape according to the target application. The logic output of the activated cell-pair allows the determination of the impact position of the detected charged particle. In addition, the sum of the logic outputs of all pixels allows the measurement of the total number of detected charged particles, hence providing information on the flux of charged particles with very high sensitivity. The total thickness of the APiX sensor can be shrinked down to the order of ten microns, including the electronics,a feature that can make this detector competitive for low material budget applications [22].

2.2 The first prototype of APiX detector

The first prototype of APiX detector was designed and fabricated in the framework of the APiX2 project funded by INFN in Italy. A two-tier prototype sensor was implemented in a commercial 150 nm CMOS process, and the two tiers designed to be independently tested before their vertical integration.

Each layer is partitioned in a 48 x 16 pixel array with 50 x 75 μm^2 pixels with different active areas (ranging from 43 x 45 μm^2 to 30 x 30 μm^2 with a maximum geometrical fill factor of 51.6 %) and integrated front-end electronics. Two types of Geiger-mode detectors have been used, with one half of the pixels implemented as p+/nwell (type 1) junction and the other as p-well/n-iso (type 2) junction. The type 1 detector has a p^+/n-well active region, with a guard ring formed by an undoped region at the borders. The n-well is electrically contacted through a deep n-iso implantation, which isolates the avalanche active region from the substrate. In the type 2 device, the avalanche region consists in a p-well/n-iso junction, where a region free from well implantation forms a virtual guard ring. A p^+ region is implanted on the device surface to form an ohmic contact with the metalization and to prevent the electrons generated at the silicon/oxide surface from reaching the space-charge region and contributing to the device dark count.

Both devices have a circular geometry with 10 μm active-area diameter. The anodes of the passively quenched pixels were connected to a 5 V quenching transistor with externally tunable gate voltage, which provides a constant-current recharge. The cathodes were biased with a high voltage, needed for Geiger-mode operation. A 5 V clamping transistor separates the device from a 1.8 V comparator with tunable threshold. The use of 5 V front-end transistors allowed the avalanche pixels to be tested with excess voltages larger than 6 V, limited by the transistor drain breakdown voltage [23].

The thickness of the active volume is very narrow, of order of 1 μm. The detectors have been covered with a metal shield to avoid optical cross-talk between different layers, but a few pixels have been left unshielded to enable optical tests. The detector front-end is the same in both layers, and includes a quenching transistor, a comparator and a programmable monostable for pulse shortening. The coincidence resolution time depends on the monostable pulse width, that can be set to three different nominal values of 750 ps, 1.5 ns or 10 ns. A configuration register is used to independently enable or disable the pixels with an arbitrary pattern. The bottom half-pixel also includes a coincidence detector and digital electronic circuits for data storage (1 bit/pixel) and readout. A schematic diagram of the pixel is presented in Fig. 2.1 and in Fig. 2.2 a micrograph of the bottom chip (on the left) is shown together with a concept view of the complete sensor (on the right). The final assembly is connected to the package through standard wire bonds from the bottom chip, while power, analog and digital signals are supplied from the bottom to the top chip through bump bonding pads.

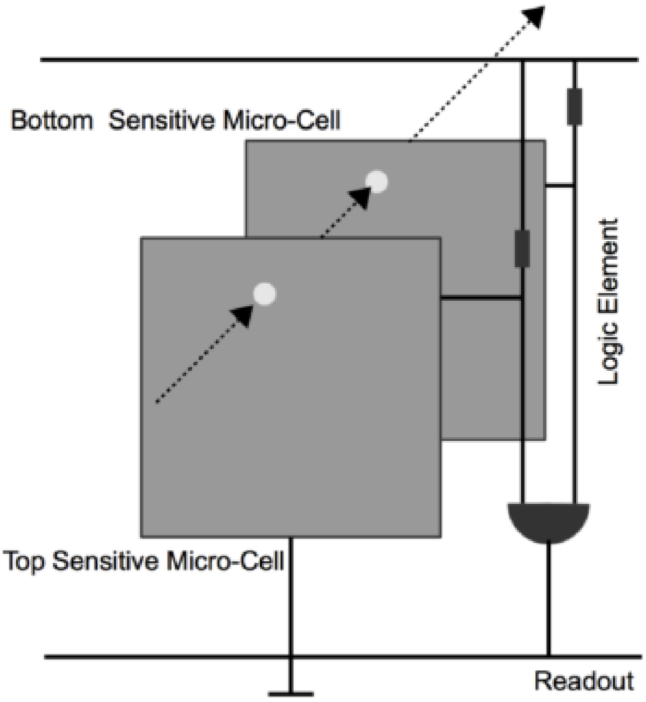

Figure 2.1: A schematic diagram of the view of APiX detector.

2.3 Characterization

Before proceeding to vertical integration, a few samples of top and bottom chips were tested for the electrical and pixels characterization. Electrical tests showed the correct functionality of both avalanche detectors and electronics in the two chips [24]. Characterization tests shows

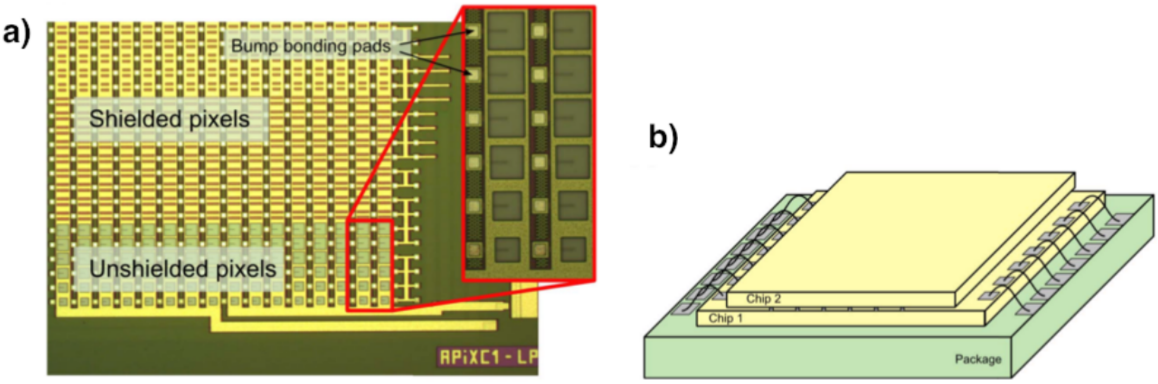

Figure 2.2: (a) A micrograph of the bottom chip (partial view) with detail of a group of pixels (b) Concept view of the vertically-integrated sensor [24]

that there is a breakdown voltage non-uniformity lower than 20 mV was found (inside the same chip) and the optical cross-talk is in the range of a few percent between neighboring pixels (at 3.0 V over-voltage) [25].

2.3.1 Dark Count Rate

The Dark Count Rate (DCR) measurements were conducted on detectors with an active junction of type pwell/deep nwell (detector Type 2) at different temperatures for two different excess voltages. In the figure 2.3 are shown the DCR distribution of the pixels of the separate layers (in black) and the distribution of the DCR in coincidence (colour lines). The coincidence measurements are done for 3 different settings of the pixel monostable circuit (red, blue and green colour, respectively for 10 ns, 1.5 ns and 0.75 ns the coincidence resolution time of the monostable).

These tests give a median DCR of 3 kHz/pixel, (corresponding to 1.5 Hz/ μm^2) at 3.3 V over-voltage and at 20 °C [25]. The average coincidence DCR (CR_{coinc}), in absence of crosstalk, can be written as function of the DCR of the single layers and the time resolution of the monostable:

$$CR_{coinc} = DCR_1 \cdot DCR_2 \cdot 2\Delta T \tag{2.1}$$

where DCR_1 and DCR_2 are the DCR of the two layers, separately, and ΔT is the coincidence resolution time defined by the monostable pulse width. The coincidence Dark Count Rate depends on the DCR statistics of the single detectors, that it is strongly affected by the distribution of defects in the sensor active volume. Monte Carlo analysis has showed that the main limitations to the detection efficiency are the thickness of the top-chip substrate and the geometrical fill factor of the detectors [24] .

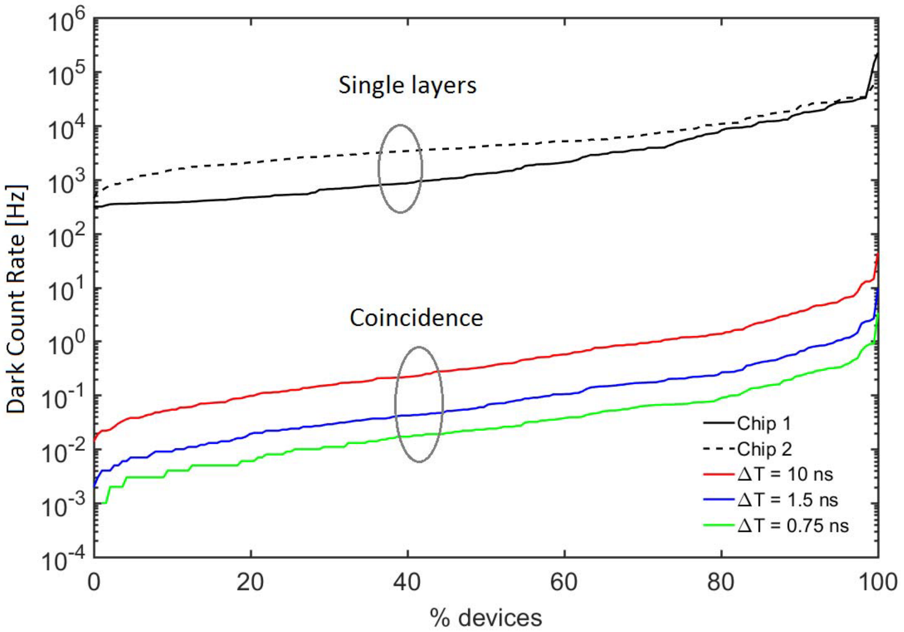

Figure 2.3: The Dark Count Rate (DCR) distribution of the pixels measured separately in the two chips (in black) and distribution of the DCR in coincidence (colour lines). The coincidence measurements are done for three different settings of the pixel monostable circuit (red, blue and green colour, respectively for 10 ns, 1.5 ns and 0.75 ns time integration). These tests are done at T=20 °C and at 1 V of overvoltage.

The coincidence DCR distribution is shown as a function of the overvoltage (VEX) bias and of the temperature in figures 2.5 and 2.4. The coincidence DCR increases with the voltage and temperature because they affect the DCR of the single layer.

2.3.2 Crosstalk

Signal crosstalk between one pixel and the neighbouring ones was investigated with a series of measurements whereby the dependence on different parameters (in particular on the detector thickness) was studied [26]. Samples with different substrate thickness were measured with the goal of understanding the role of the substrate in the crosstalk process. Both types of devices (Type 1 and Type 2) were analyzed by measuring two 8 x 24 pixel subarrays with uniform

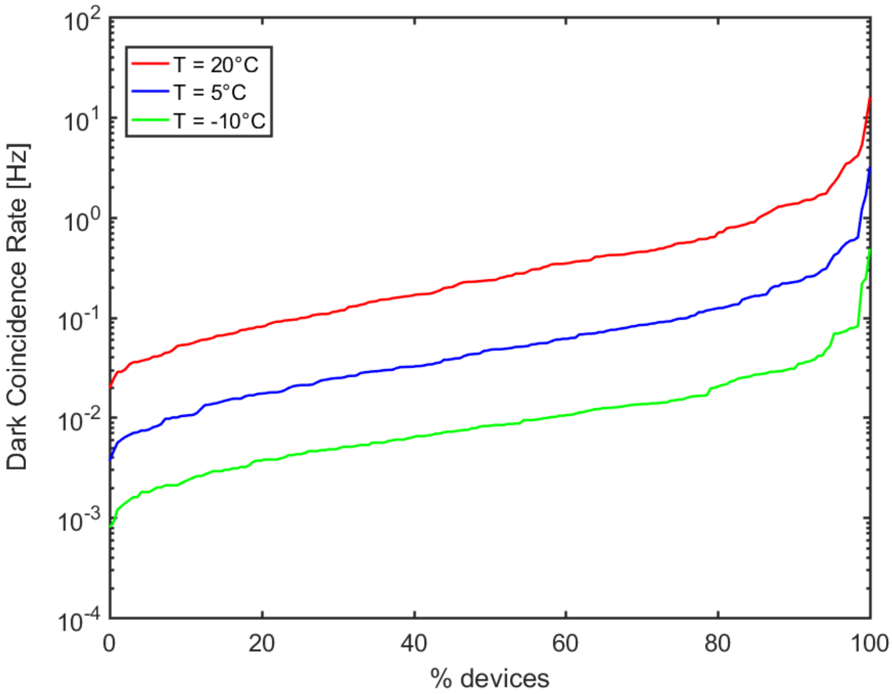

Figure 2.4: DCR coincidence distribution of the pixels as a function of temperature at overvoltage = 2 V and Δ T = 0.75 ns.

detector type and size. The avalanche detectors in the subarrays have the maximum active area of 43 x 45 μm^2, while the measured dies have three different thicknesses of 280 μm, 50 μm and 25 μm. The analysis of crosstalk is reported as a function of the distance between emitter and detectors. A high DCR pixel at the border of the array was employed as an emitter of secondary photons while the rest of the array was scanned a pixel at a time.

In presence of cross talk, the coincidence rate can not be expressed by the equation 2.1, but by the formula:

$$CR_m = CR_{coinc} + k \cdot (DCR_1 + DCR_2) \tag{2.2}$$

where CR_m is the measured coincidence rate and k the crosstalk coefficient. Replacing 2.1 in 2.2 we can calculate the crosstalk coefficient using 2.3.

$$k = \frac{CR_m - 2\Delta T \cdot DCR_1 \cdot DCR_2}{DCR_1 + DCR_2} \tag{2.3}$$

Figures 2.6, 2.7 and 2.8 show the value of the crosstalk coefficient as a function of different distances between detector and emitter.

The crosstalk coefficient decreases rapidly when detectors are at a low distance from the

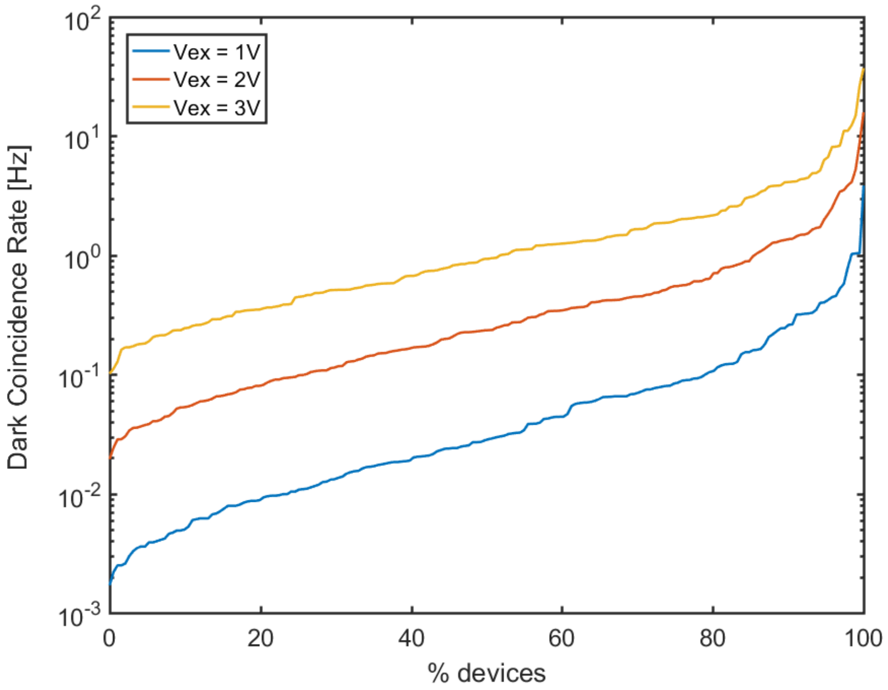

Figure 2.5: DCR coincidence distribution of the pixels as a function of the overvoltage (VEX) at T=20 °C and Δ T = 0.75 ns [24].

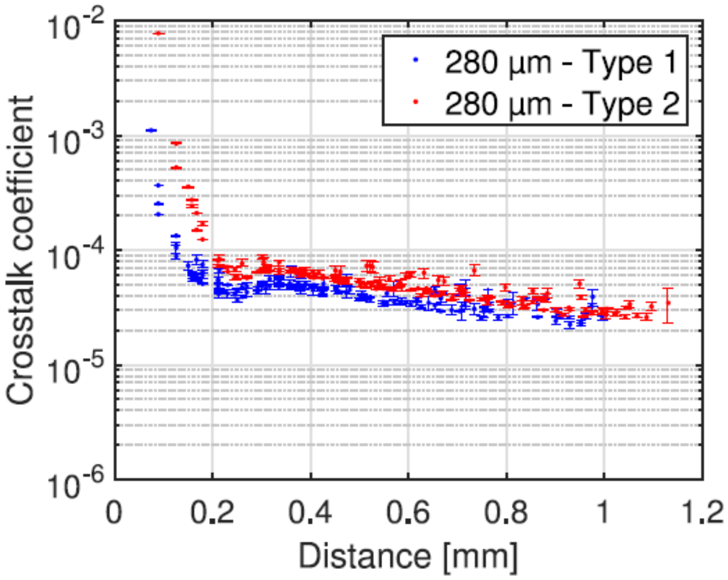

Figure 2.6: Crosstalk coefficient as a function of detector distance for 280 μm substrate thickness [26].

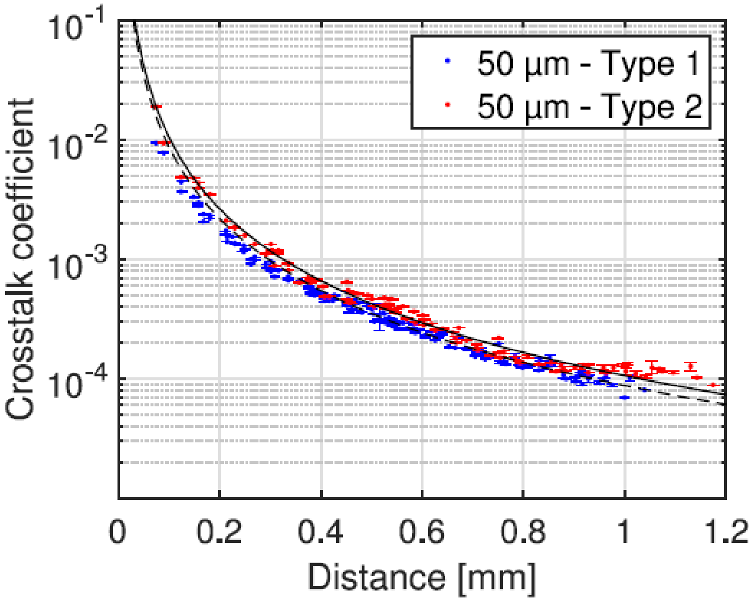

Figure 2.7: Crosstalk coefficient as a function of detector distance for 50 μm substrate thickness. Dashed and continuous black line are $\frac{1}{r^2}$ fitting curves for both types of devices. [26].

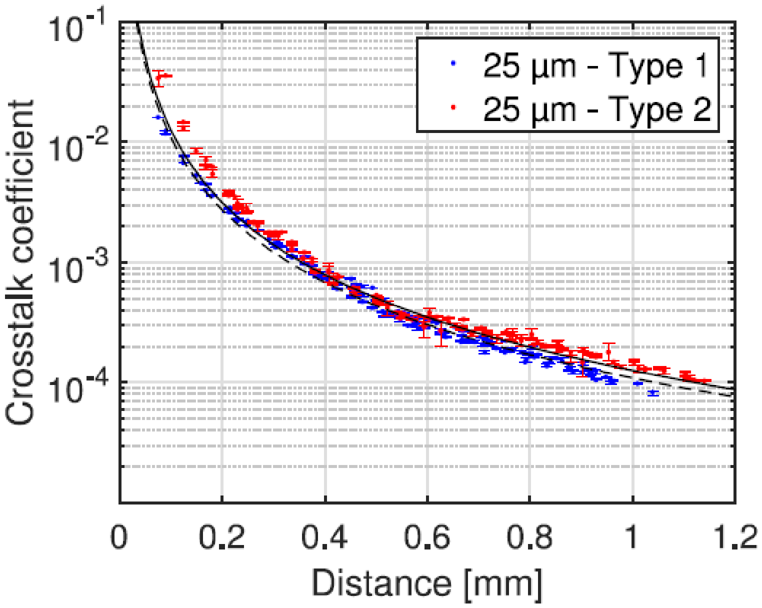

Figure 2.8: Crosstalk coefficient as a function of detector distance for 25 μm substrate thickness. Dashed and continuous black line are $\frac{1}{r^2}$ fitting curves for both types of devices.[26].

emitter, while at higher distances the decrease is less pronounced. In 280 μm thick devices in Fig. 2.6 the crosstalk coefficient does not decrease monotonically, but rather shows a secondary peak at a distance of about 350 μm for both device types. This peak can be explained considering the presence of direct and indirect crosstalk. This secondary peak is not present for thinner samples, since the distance between neighboring pixels is in the order of or even larger than the thickness of the substrate, and the substrate behaves as a 2D wave guide for secondary photons. Due to the waveguide effect, the crosstalk coefficient is expected to be proportional to $\frac{1}{r^2}$, where r is the distance between the emitter and the detector. This model has been used to interpolate the experimental data in Figs. 2.7 and 2.8. The comparison between Type 1 and Type 2 devices substantiates the presence of higher values of the crosstalk coefficient for Type 2 devices [26].

2.4 Beam test results

The first beam test carry out to study the performances of APiX detector was at CERN SPS in October 2016. There were collected more than 6 million triggers in a series of runs with pions beams of 50, 100,150, 200 and 300 GeV energy. The beam test layout consisted of two independent ApiX sensors embedded into a silicon-strip Beam Tracker (BT) aligned on the beam line as is schematically shown in figure 2.9. In particular the BT included a total of 10 silicon-strip sensors with a pitch of 720 μm out of which to allow for a precise track reconstruction and 4 dedicated high-resolution (HR) sensors with a smaller pitch of 80 μm were positioned immediately upstream and downstream of the APiX sensors, respectively.

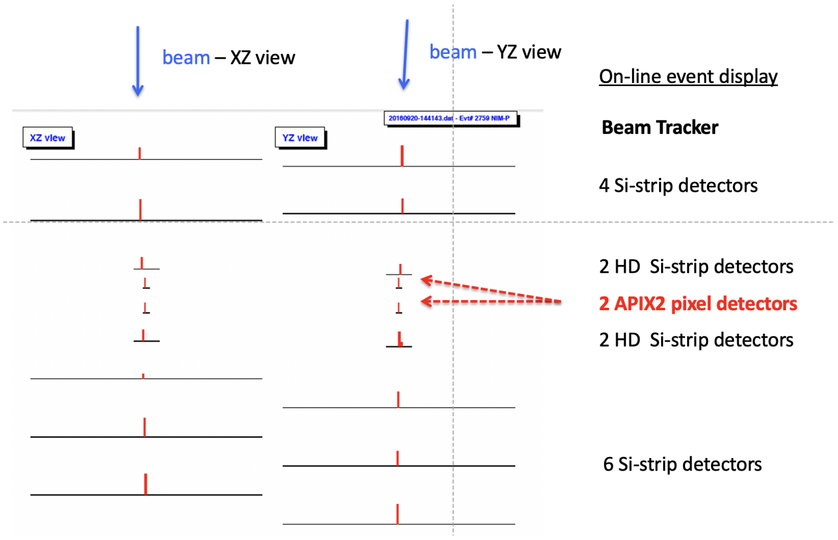

Figure 2.9: Schematic layout of the beam tracker at the CERN beam test [27].

The HR sensors were mechanically mounted close to each other, at a distance of 2.5 cm along the beam. An X-Y micrometer translation stage allowed their relative alignment which was optimized after a few iterations during the beam test. The silicon detectors allowed the reconstruction of the tracks of the beam particle by means of 7 independent position measurements per view (XZ or YZ, the beam propagating along the positive Z axis) [25].

The trajectory were reconstructed by calculating their coordinates as the center of gravity of the cluster of hits formed by the one with the largest signal in the layer (the "seed" one) and its two adjacent neighbors. Track quality was enforced by a chi-square cut. The impact points (IP) of the beam particle on the detector plane was extrapolated by the fitted tracks, allowing the identification of the pixel that had been hit [27].

The reconstructed position of the IP allowed to define 6 different regions in each sensor where the measurement of the efficiency was carried out as is shown in figure 2.10.

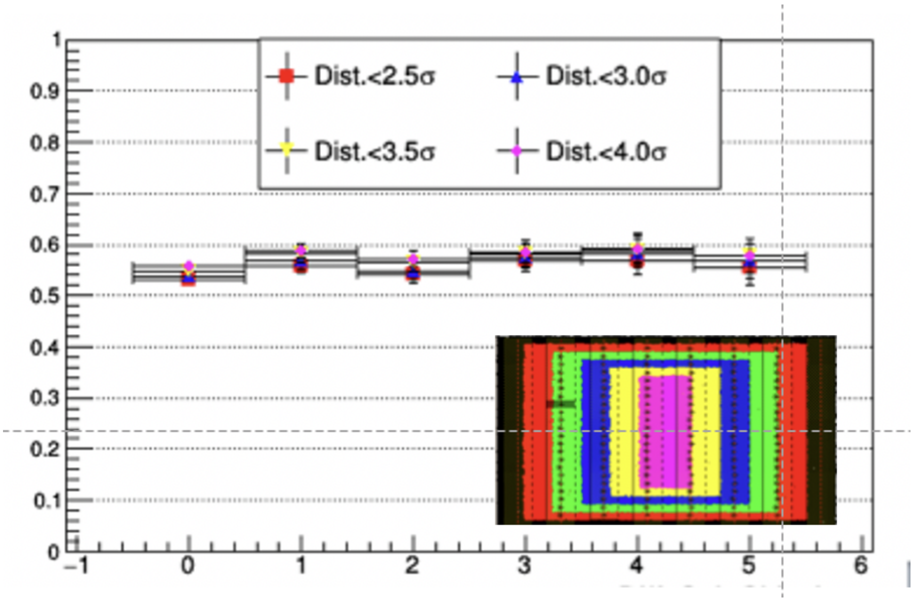

Figure 2.10: Measured efficiency in 6 different fiducial areas covered by the reconstructed track impact point on the detector. [27].

The resolution on the extrapolated track impact point turned out to be of the order of 150 μm, as is shown in figure 2.11. It is not adequate to match the finer granularity of the APiX pixels because of the poor performance of the HD sensors during the test. In order to over come this hardware problem, during the offline analysis of the data, the precision on the impact point position was enhanced by using the known coordinates of the pixel being hit on one of the two APiX sensors while testing the efficiency of the second sensor, and viceversa. In this way, 6 different regions in either detector were mapped for the measurement of the efficiency

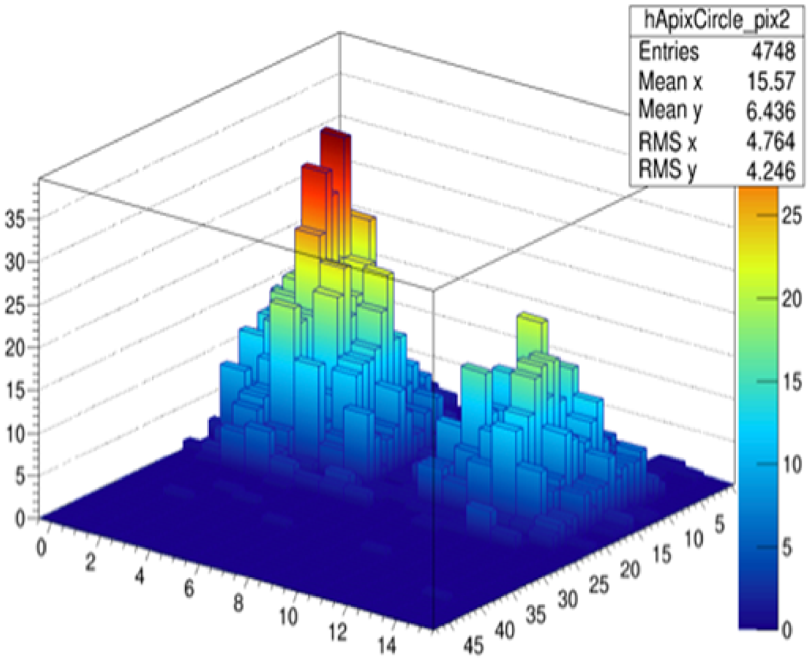

Figure 2.11: Reconstruct image of two adjacent structures separated by˜150 μm from the data taken at CERN beam test. [27].

as shown in figure 2.10. The residual between the impact point and the pixel under test was calculated for each event and normalized with its standard error (RMS) on the impact point position. In figure 2.10 is shown the detection efficiency measured on the given fiducial region, from the largest 0 (black colour) to the smallest 5 (pink colour). For each region, it is plotted using 4 different markers on each data point refer to as many different event selections whereby the distance between the impact point and the pixel under test. In particular the distance was ranging from 2.5 σ to 4 σ. Averaging over the different measurements during the CERN beam test, the resulting efficiency turns out to be (56.2 ± 5) %.

This result indicates that the detection efficiency is mainly limited by the geometrical Fill-Factor (FF) that can be estimated, to first order, by taking into account the chip dead areas where the pixel electronics and guard-ring are located [24]. Differently from optical sensors (i.e. SiPMs) where the fill-factor (FF) is limited by the geometry of light absorbing structures, in this case a more accurate prediction of the FF requires a thorough computer simulation of the spatial distribution of the ionization generated inside the sensor[27].

2.5 Radiation tolerance tests

An accurate characterization, in terms of DCR, of SPADs array tolerance to ionizing and non ionizing radiation was performed as described in [28]. The tests were carried out on 6 detectors (“APIXFAB0” single-tier chips) with Geiger cells similar to “Type 1”, fabricated in 180 nm CMOS technology with 36 x 40 μm^2 of active area. In particular 2 chips were irradiated with X-rays up to a maximum dose of 1 Mrad (SiO_2) using a 10 keV RP-149 X-ray Semiconductor Irradiation System from Seifert available at the Physics and Astronomy Department of the University of Padova (Italy) and the other remaining 4 were exposed to neutrons at the INFN Laboratori Nazionali di Legnaro. The energy of the neutrons was between 0.5 and 3 MeV generated by a 5 MeV proton beam impinging on a beryllium target. The maximum fluence reached was 10^{11}, 1 MeV neutron equivalent cm^2, and measurements of DCR were performed before and after annealing at 60 °C for 80 minutes [25].

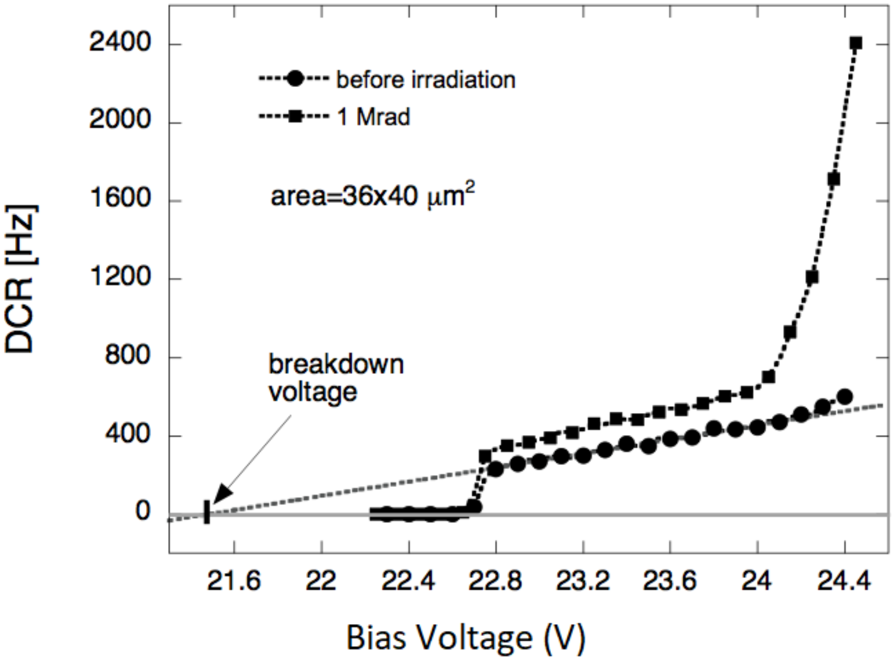

Figure 2.12: Dark count rate as a function of the voltage applied to the SPAD cathode before and after X-ray irradiation: with circle symbol are represented the data before irradiation and in square the data after irradiation [28]

In figure 2.12 is shown the DCR as a function of the voltage applied to the SPAD cathode before and after exposure to a total ionizing dose of 1 Mrad (in SiO_2). Less than 2.5 V of overvoltage (below about 24 V of bias) a slight increase in the DCR is observed, this is likely due to a radiation-induced increase in the density of defects at the interface below the passivating oxide. Increasing the overvoltage (applying above 24 V) there is a much steeper increase that may be related to a radiation-induced breakdown phenomenon in a secondary junction [25].

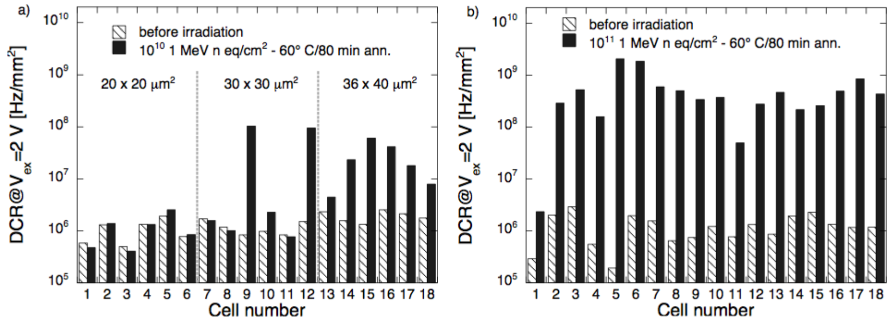

Figure 2.13: The DCR distribution at an excess voltage of 2 V normalized to the sensor area, for two sets of chips exposed to fluences of 10^{10} (on the left) and 10^{11} (on the right) 1 MeV neutron equivalent cm^2 respectively and subjected to the annealing procedure. Pre (columns in white) and after (columns in black) irradiation values are compared for different cells. The DCR increase, after irradiation, can be reasonably assumed to be proportional to the sensitive volume of the detector and to the neutron fluence [28]

.

In Fig. 2.13 shown the DCR at an excess voltage of 2 V normalized to the sensor area, for two sets of chips exposed to fluences of 10^{10} (on the left) and 10^{11} (on the right) 1 MeV neutron equivalent cm^2 respectively and subjected to the annealing procedure. Pre (columns in white) and after (columns in black) irradiation values are compared for different cells. The DCR increase, after irradiation, can be reasonably assumed to be proportional to the sensitive volume of the detector and to the neutron fluence. This is in agreement with the expected stochastic nature of neutron damage, that is likely due to the creation of deep level defects in the bulk of the Devices Under Test (DUTs). For DUTs exposed to the smaller fluence, cells with the smallest area do not show any significant DCR increase, while most of the cells with the largest area feature an increase in the DCR of one order of magnitude or more. A very large increase in DCR, up to about 3 GHz/mm^2, was instead measured in devices exposed to the larger fluence [25].

2.6 The second APiX prototype

The new chip is an evolution of the previous one successfully tested by the APiX2 collaboration. The two sensor chips, as in the first prototype, are bump bonded on top of each other in order to make a dual-tier structure, but the chips can also be tested independently. The design explores new features regarding the in-pixel electronics, fill factor improvement and matrix complexity.

The chips are designed in a standard 150 nm CMOS technology. The so called "father" (at the bottom) and "son" chip (at the top) dimensions are 6 mm x 5 mm and 5.4 mm x 5 mm respectively and they share the same electronics. Once they are bump bonded (one the mirrored version of each other in view of their vertical integration) all the input signals, the reference and supply voltages, the sensor bias voltages and coincidence output signal are provided to the father chip and delivered to the son chip through the bump bonding contacts.

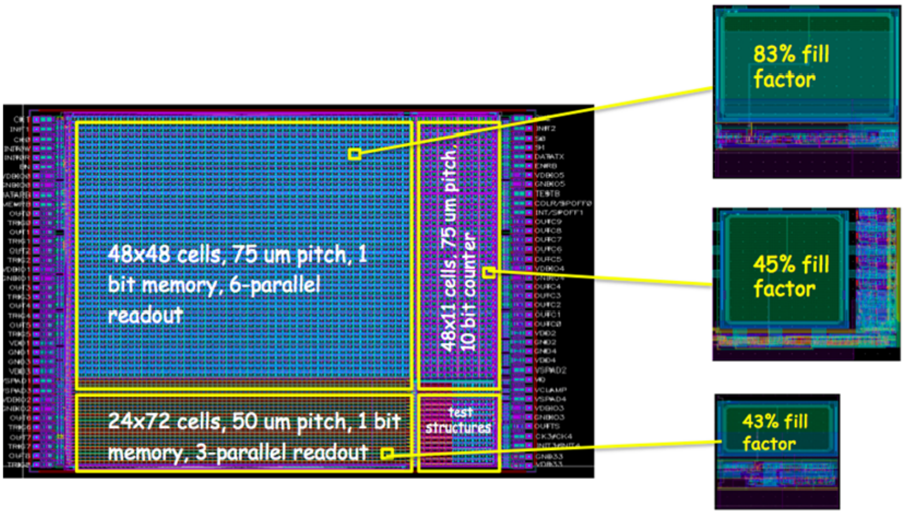

Figure 2.14: Schematic layout of the partitioning of the second prototype[27]

The whole array is divided into four sub-matrices as schematically shown in Fig. 2.14. Three of them, with a 75 μm x 75 μm pitch, are composed of, respectively, 48 x 48 pixels, 12 x 48 pixels, 11 x 15 pixels, respectively, and the forth one of 24 x 72 pixels with a 50 μm x 50 μm pitch, including different test structures: active quenching front-end electronics, pixels with different sensitive area and different process splitting. The pixel selection of a given sub-matrix is performed by programming dedicated row and column shift registers and each array can be individually disabled by switching off the electronics supply. The chips layout design has been carried out in such a way to improve and maximize the fill factor in the arrays 1, 2 and 3. In particular, a fill factor of 66% was reached in the array 1, whereas a fill factor of 44% and 39% was obtained in the array 2 and 3 respectively.

2.7 The first prototype of the probe

One of the possible applications of the APiX sensor is for the imaging of radioactive β-sources that are currently employed as tumor markers in nuclear medicine. The goal of our team is to develop a hand-held probe, to be used in radio-guided surgery, with the capability to provide real-time imaging of the spatial distribution of β-emitters. A preliminary study has been carried out with computer simulations based on the GEANT4 code as described in chapter 3 of this thesis. Using a 3D printer, a hand-held probe was built in which the APiX chip is installed. In particular the sensor is fixed on a PCB-flat cable as shown in Fig. 2.15. In the back of the PCB are welded five capacitors to filter the digital noise from the acquisition system. This flat element (that looks like a "bracelet" as we call it) is encased in a "pencil-like" plastic shell, as shown in Fig. 2.7. This final first prototype probe has a length of 14 cm and a front section of 2.0 x 4.0 cm^2. The chip is fixed as close as possible to the front surface of the window and this distance is 0.5 mm.

Figure 2.15: The PCB flat cable on which the APiX detector is fixed: front view (top) and rear view (bottom).

This capton flat cable brings out the signals of the chip and using 2 HDMI cables these signals are sent to an interface PCB 2.18, and from there to the remaining acquisition system. All the signals were readout by a Ladder Controller (LAC) board that formats the sub-events and supervises the distribution of physics and calibration triggers. The LAC board is interfaced via USB to the main DAQ, running on a PC under Linux. In Fig. 2.18 the two interface boards used in the setup to take data in the laboratory are shown.

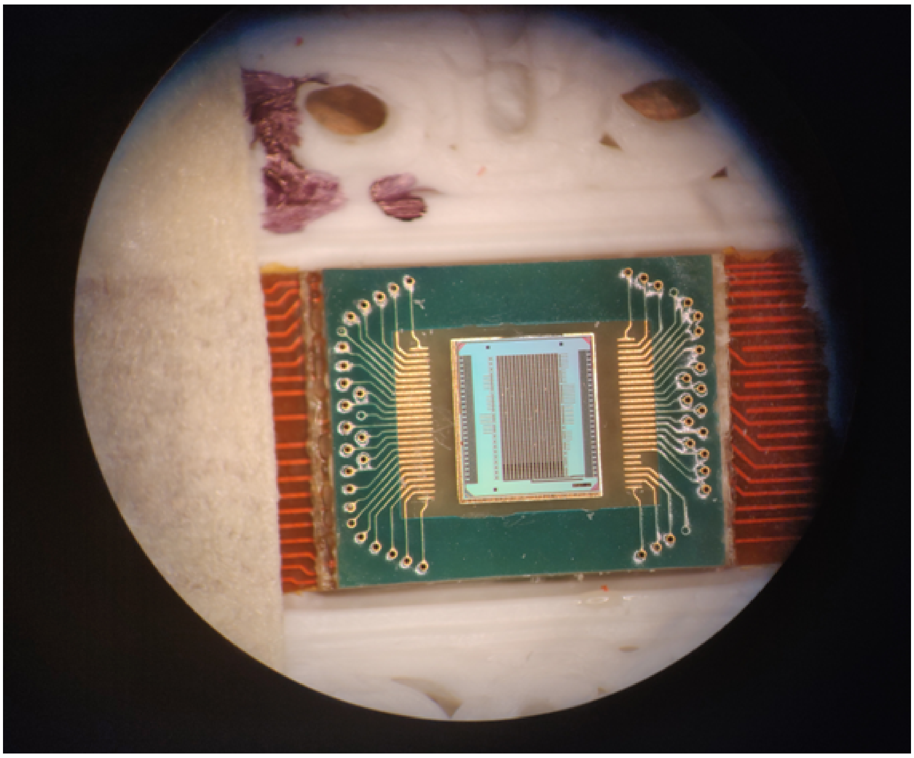

Figure 2.16: Microscope view of the front APiX chip microbonded on the flat PCB cable.

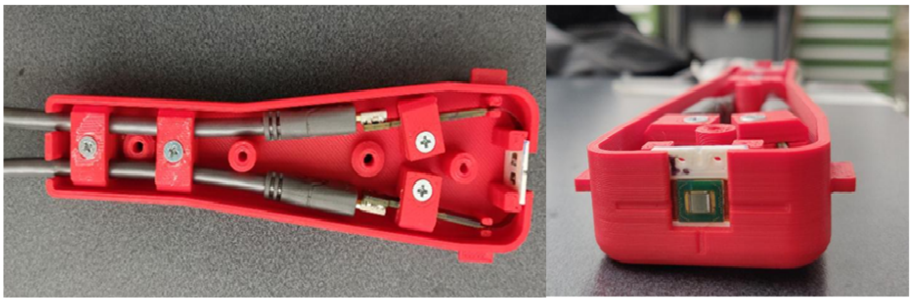

Figure 2.17: The first prototype of the hand-held probe: (left) a longitudinal view, the flat pcb cable (on which the APiX sensor is microbonded) and the two HDMI cables fixed inside the probe; (right) a front view of the probe.

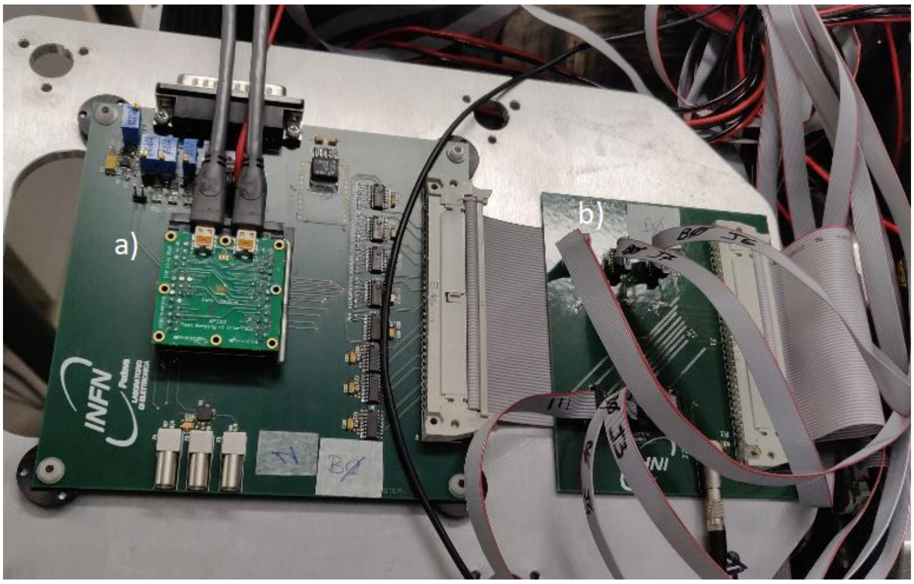

Figure 2.18: The two interface boards: a) the probe ZIF interface board, where the signals are sent to a second board using two HDMI cables; b) ZIF - LAC interface board.

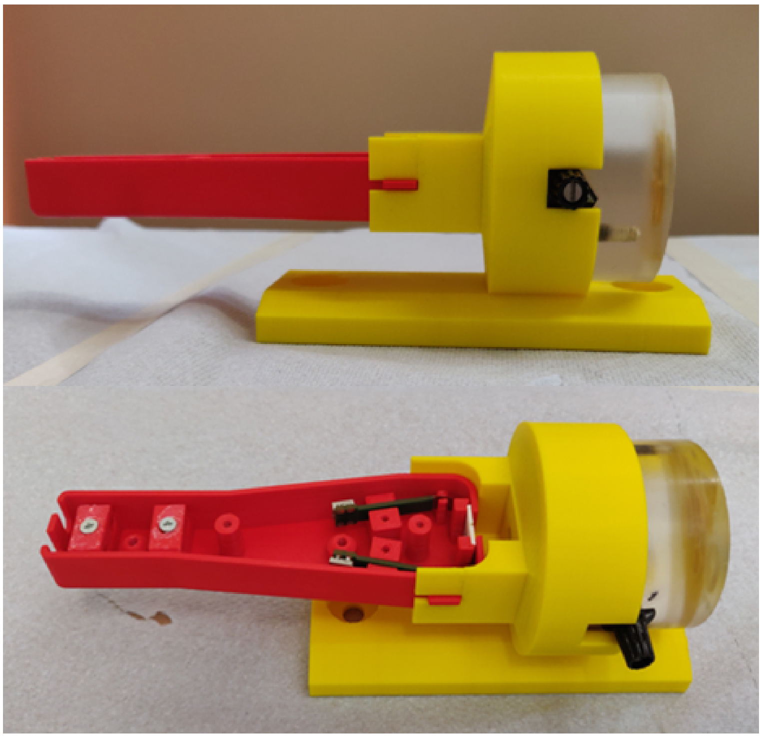

Figure 2.19: First setup of the probe and ^{90}Y source for the first measurements in our laboratory. The red hand-held probe is fixed to the yellow source holder structure. On one side it is possible to fix the probe well aligned with the source at a fixed distance and a collimator can be placed in between.

Chapter 3

GEANT4 Simulations

In this chapter we describe the computer simulations carried out to study the response of the APiX probe prototype, under some different measurement conditions.

In many fields of physics research and applications the Monte Carlo (MC) techniques is a standard tool, mainly used to simulate particle generation, transport and interactions in media. From the knowledge of the physics of the elementary collision processes, the Monte Carlo simulations create and track a large number of primary particles, as well as the secondaries created in the interactions. During these simulations, a certain amount of information is stored and analyzed. The main advantage of this approach is that it permits to study various different configurations before (or even without) performing specific measurements. The other use of simulations is to support experimental data comprehension, by helping to recognize unexpected structures and phenomena.

MC techniques find wide applications also in medicine, and in particular in nuclear medicine. Each radiotherapeutic treatment is in fact preceded by MC simulations aimed at verifying the exact localization of energy deposition inside the body.

The platform used for our simulations is Geant4 (GEometry ANd Tracking). It uses Monte Carlo methods for the generation and the passage of particles through matter. It is the latest of the GEANT series of software toolkits developed by The Geant4 collaboration (with the participation of CERN), and the first simulation code uses object oriented programming (in C++). Its development, maintenance and user support are taken care by the international Geant4 Collaboration. Application areas include high energy physics and nuclear experiments, medical, accelerator and space physics studies.

Geant4 includes facilities for handling geometry, tracking, detector response, run management, visualization and user interface. The geometry consists of an analysis of the physical layout of the experiment, including detectors, absorbers, etc., and considering how this layout will affect the path of particles in the experiment. The tracking consists of simulating the passage of particles through matter. This involves considering possible interactions and decay processes. Detector response is recorded when a particle passes through the detector volume, and this normally approximates well how a real detector would respond. During run management the details of each run (a set of events), is recorded, as well as the setup of the experiment in different configurations between runs. Geant4 offers a number of options for visualization, including OpenGL, and a familiar user interface, based on Tcsh (i.e. it is a Unix shell based on and compatible with the C shell).

Geant4 provides a wide set of tools for all the domains of detector simulation, such as geometry modeling, detector response, run and event management, tracking, visualisation and user interface. An abundant set of physics processes handle the diverse interactions of particles with matter across a wide energy range, as required by Geant4 multi-disciplinary nature; for many physics processes a choice of different models is available. In Geant4 a run is a collection of events which share the same detector conditions. At the beginning of a run, the geometry is optimized for navigation and cross-section tables are calculated according to materials specified in the geometry and the cutoff and threshold values defined. G4Event class represents an event. At beginning of processing, an event contains primary particles. These primaries are pushed into a stack and an event is over when the stack becomes empty.

In Geant4, some classes are mandatory. In particular, these are: G4VUserDetectorConstruction, G4VUserPhysicsList (invoked at the initialization) and G4VUserPrimaryGeneratorAction (invoked during an event loop); respectively, they define the geometry and the characteristics of the detector, the physical properties of particles and materials for the simulation of particle-matter interactions and generate primary vertices and primary particles for each event during the simulation.

In this thesis, a number of simulations were carried out using different the simulations using point source and volume source geometries to study the intrinsic efficiency of two different detector prototype (APiX 2.4 x 1.2 mm^2 and APiX 5.0 x 5.0 mm^2) under different conditions.

The efficiency of a detector is an estimator of its ability to detect radiation. It is measured by placing a source of radiation in the vicinity of the detector and dividing the number of particles ($N_{particle}$) or photons detected by the number of those emitted:

$$efficiency = \frac{N_{particle} detected}{N_{particle} emitted} = \frac{N_{particle} reaching\ detector}{N_{particle} emitted} \cdot \frac{N_{particle} detected}{N_{particle} reaching\ detector}$$

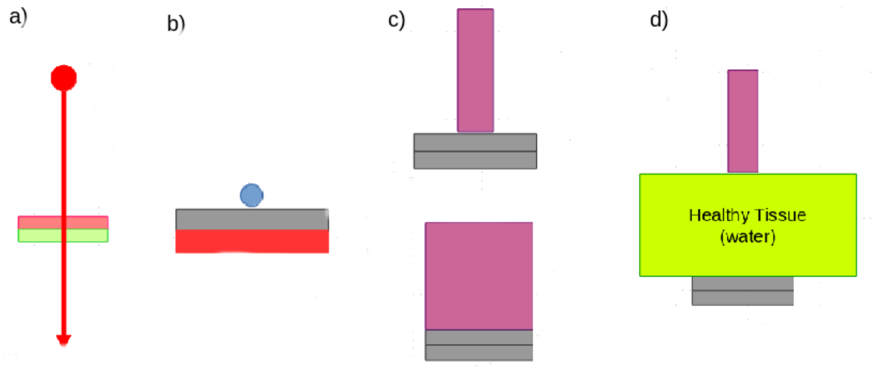

Figure 3.1: The main configurations used in the simulation are: a) the fixed energy electron beam; b) point source; c) **top** volumetric source with radius of 1 mm and **bottom** volumetric source with radius of 5 mm , both without absorber medium between the detector and the source; d) volumetric source with radius of 1 mm and absorber medium (water) between the detector and the source.

Therefore, the detection efficiency is the product of two terms, the geometric efficiency, that is the fraction of emitted particles or photons hitting the detector, and the intrinsic efficiency, which is the fraction of those particles or photons that reach the detector that are detected. The geometric efficiency is determined by the geometric relationship between the source and the detector. It increases as the source is moved toward the detector and for a source placed inside a "well" detector (i.e a detector containing a cavity for the insertion of samples) the geometric efficiency becomes closer to 1, because most of the particles or photons are intercepted by the detector.

The intrinsic efficiency of a detector in detecting photons, often called the quantum detection efficiency (QDE), is determined by the energy of the photons and the atomic number, density, and thickness of the detector. For charged particle detectors, the intrinsic efficiency is governed by a number of parameters. For instance, for avalanche detectors they include the efficiency of generating the avalanche and the collection efficiency of the signal.

3.1 Geometry and Environment Settings

G4VUserDetectorConstruction is a mandatory class, to be included in the main function, that specify the detector geometry. This is where the user describes the entire detector setup, including its geometry, the materials used in its construction, a definition of its sensitive regions and their readout. There are two landmarks used in defining the geometry of the setup in Geant4:

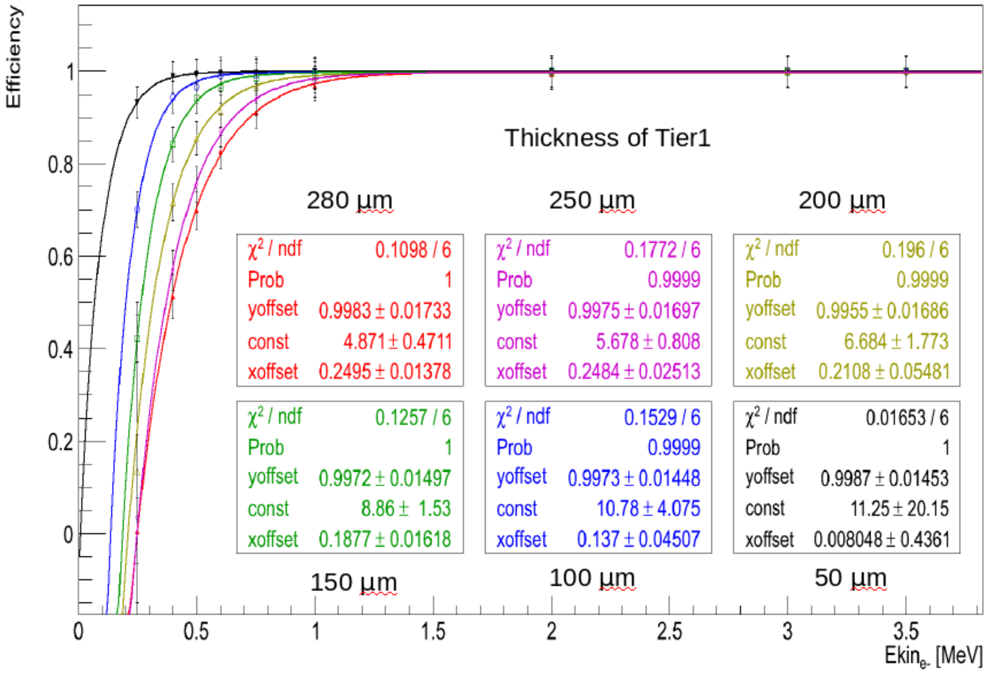

Figure 3.2: Intrinsic efficiency versus electron energy, for different thickness of first layer of the detector (in different colors). The efficiency increases with the energy of the incident electrons and by decreasing the thickness of the first layer.

the "world" volume and the internal reference frame of the simulation. The first single element is the volume that includes all the three-dimensional space that the simulation has to consider and the second one is a cartesian system that has its origin at the centre of the "world". Each volume is created by describing its shape and its physical characteristics, and then placing it inside a containing volume. This is done defining the three volume types: solid, logical, and physical. After creating a solid volume (e.g. box, cylinder), to create a logical volume it is necessary to assign to this solid volume a material. This is defined as an element or a compound. The latter are defined by their atomic composition as given by a chemical formula or weight fractions, their density at a given temperature and pressure and their mean excitation energy. The physical volume is simply a placed instance of the logical volume, with the specification where to place its center within that volume, and how to rotate it.

In general, the term geometry in Geant4 refers to the volumes built in the simulation, whether these are sensitive components registering hits or merely pieces of material the particles traverse. The part of the system that generates the primary particles is not included in the geometry definition but in the ‘primary event definition’, that will be explained in the next sections.

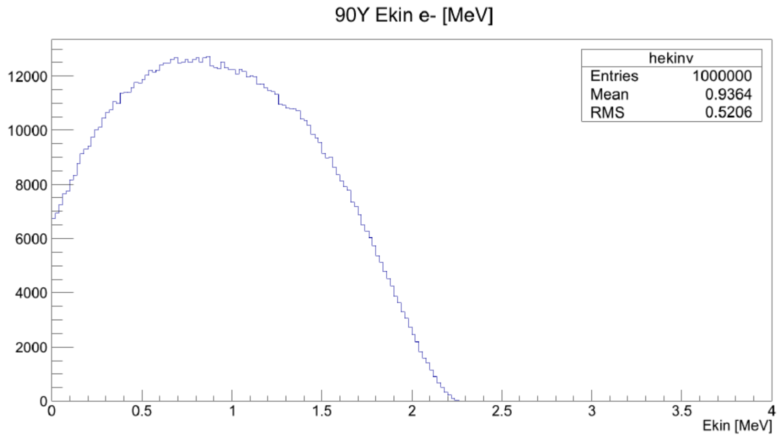

Figure 3.3: The emission spectrum of ^{90}Y is shown with peak emission at 1 MeV and end-point at 2.2 MeV

In the simulations reported here, the detector is a parallelepiped, immersed in an air world volume. The parallelepiped is composed of two o three tiers and each one has two different sizes: 2.4 x 1.2 mm^2 and 5.0 x 5.0 mm^2. Thus, for each size, two types of detector are simulated: type 1 composed of two tiers and type 2 composed of three tiers. In both of them one tier has a fixed thickness of 280 μm, while the other tiers have different thickness from 50 μm to 280 μm. Therefore the detector has a total maximum and minimum thickness of 560 μm and 330 μm, respectively, if it is composed of two tiers, and 840 μm and 380 μm if it is composed of three tiers.

3.2 Physics List

The physics list is one of the mandatory class to run a Geant4 simulation. It describes all the physics that control the behavior and generation of the particles. This part of the simulation consists in defining the initial state of the simulation, i.e. the ‘primary particles’. Once this is done, Geant4 will track the particles through the system (following the definition of physics processes) until they stop, decay or are transported beyond the limits of the world volume.

The generation of the primary event can be done using an interface to an event generator or the particle "gun" class, which creates a beam of particles by defining their type, position, direction of motion and kinetic energy. In these simulations the generation of the primary event is done by using the particle gun class, for three different source setups: a fixed energy

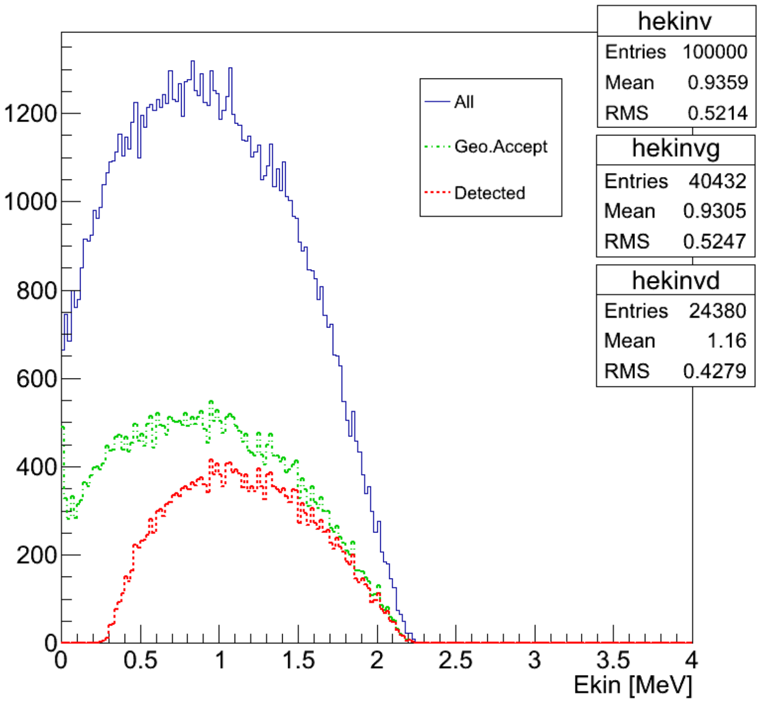

Figure 3.4: The spectra of the emitted electrons of a ^{90}Y point source: the blue curve refers to all emitted electrons, while the green curve shows the events falling inside the geometrical acceptance and the red curve the electrons detected by the APiX sensor.

electron beam, a point-like isotropic source and a volume isotropic one. For each type of the source setups there are various configurations. In particular for the point source there are two of them where electrons are simulated, first with fixed vertex position and momentum direction, changing the kinetic energy of the electron from 0.25 MeV to 3.5 MeV and, in the second case, electrons from ^{90}Y or ^{106}Ru radioactive sources. Both isotropic point-like sources placed on top of the detector.

These two radioactive sources are used to simulate a volume source in different setups. In particular, the volume source is embedded in air or water, with or without absorber (i.e. the absorber simulates the healthy tissue between the detector and the source), at different distances from the surface of the detector.

3.3 Simulation results

In the next subsection we show the results obtained with different source configurations for both detector prototypes (2.4 x 1.2 mm^2 and 5.0 x 5.0 mm^2) in terms of the intrinsic efficiency of the detector, calculated as the ratio of the events detected versus the ones that reach the detector, versus the energy of the impinging particle at different depths inside the detector.

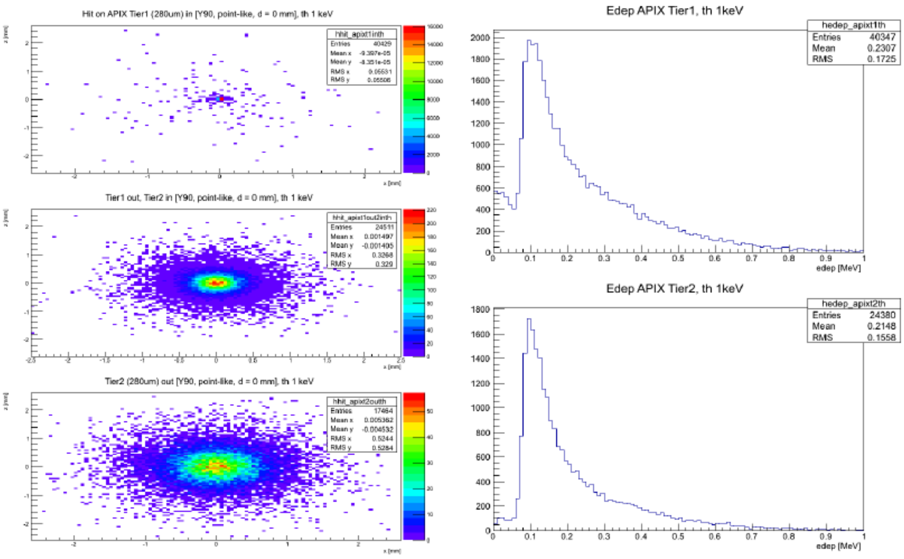

Figure 3.5: An example of the ^{90}Y point source spatial distribution of the hits on the APiX detector in different tiers (on the left) and their energy spectra (on the right). The three plots on the left (from the top to bottom) show the hits on the first tier, at the exit of the first tier and on the second tier, respectively.

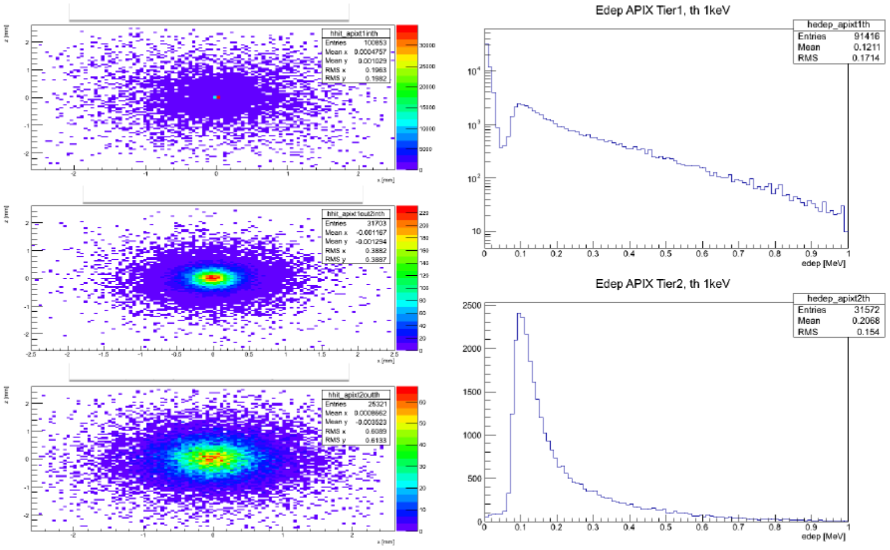

Figure 3.6: An example of the ^{106}Ru point source spatial distribution of the hits on the APiX detector in different tiers (on the left) and their energy spectra (on the right). The three plots on the left (from the top to bottom) show the hits on the first tier, at the exit of the first tier and on the second tier, respectively.

3.3.1 Fixed energy electron beam

The primary particle in this setup configuration is simulated as belonging to a fixed energy electron beam. It has a given vertex position and distance from the detector and a fixed momentum direction. In the simplest case it has a normal incidence on the detector and the energy simulated are in total 9 values (0.25, 0.4, 0.5, 0.6, 0.75, 1.0, 2.0, 3.0 and 3.5 MeV). For each value of the energy, 1000 events are simulated. The geometric efficiency is almost 100%. A hit is defined as an event that passes through the two tiers of the detector. In Fig.3.2 we show the intrinsic efficiency of the detector as a function of its thickness. In this plot we can see that for electrons with energy larger than 1.2 MeV, the intrinsic efficiency is almost 100% for all the different thicknesses of the detector (from the thinner one of 230 μm to the thicker one of 560 μm).

The intrinsic efficiency increases with the energy of the electrons and is inversely proportional to the thickness of the upper layer (Tier 1) of the detector at a given energy. For example there is an intrinsic efficiency exceeding 90% for a Tier 1 thickness of 50 μm and electrons energy larger than 0.2 MeV or for a thickness of 280 μm and electrons with energy > 0.75 MeV.

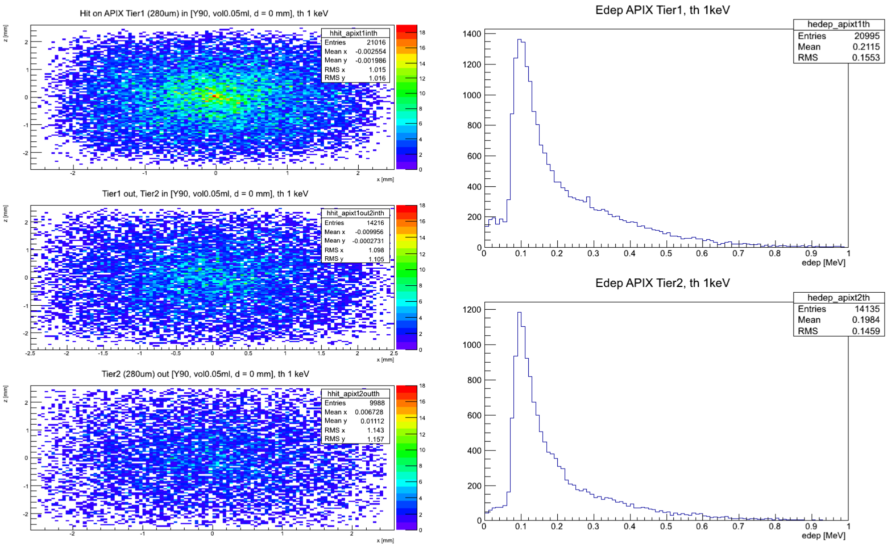

Figure 3.7: An example of the ^{90}Y volume source (in air) spatial distribution of the hits on the detector in different tiers (on the left) and the deposed energy inside tier one and tier two, for a detector threshold set at 1 keV (on the right). The three plots on the left (from the top to bottom) show the hits on the first tier, at the exit of the first tier and on the second tier, respectively.

3.3.2 Point source

Two different point sources were simulated: ^{90}Y and ^{106}Ru, positioned directly on the surface of a 5 x 5 mm^2 detector. It consists of two tiers of 280 μm. In this case the source is isotropic and the geometrical efficiency is different from 100% in the case of the previous setup. In particular the Fig.3.4 shows an example of 10^4 simulated events, and the detector has a geometrical efficiency of 40% and an intrinsic efficiency of 60%.

In Fig.3.3 the emission spectrum of ^{90}Y is shown with peak emission at 1 MeV and end-point at 2.2 MeV.

Fig.3.4 shows the spectra of the emitted electrons of a ^{90}Y point source: the blue curve refers to all emitted electrons, while the green curve shows the events falling inside the geometrical acceptance and the red curve the electrons detected by the APiX sensor. The ratios of the green/blue and red/blue curves as a function of electron energy (at the source) are representative of the geometrical and detector efficiencies, respectively.

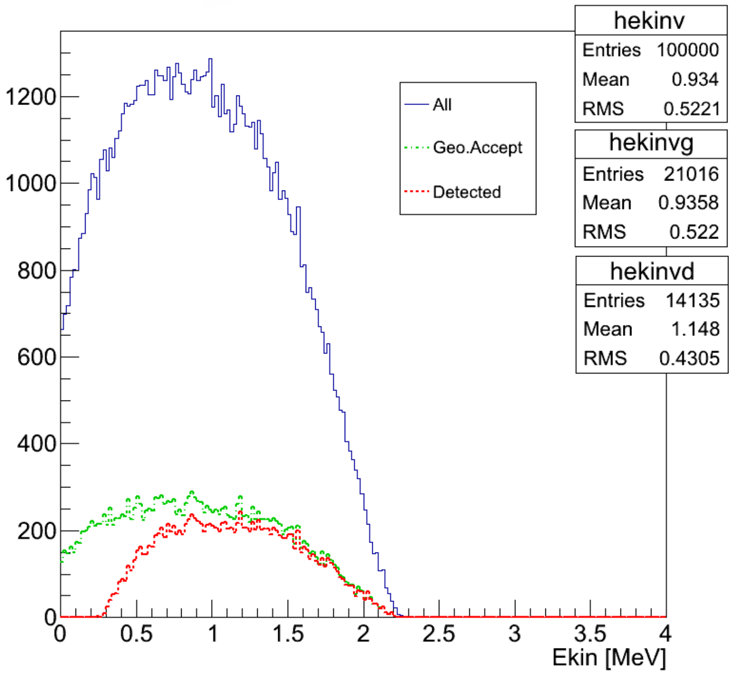

Figure 3.8: Spectral distribution of hits in the detector versus the kinetic energy of the ^{90}Y source electrons. Events from the source emission are shown (in blue), together with the ones that hit the surface of the detector (in green) and the ones detected (in red). These events are simulated assuming that the source is in air.

Figs.3.5 and 3.6 show the spatial distribution of the hits on the detector (on the left) and their energy spectra (on the right), respectively for a ^{90}Y point source and ^{106}Ru one. The spatial distribution is simulated considering (from the top to bottom) the hits on the first tier, at the exit of the first tier and on the second tier, respectively.

3.3.3 Volume source

Simulations were carried out with an isotropic volume source by changing the total volume of the source and the material in which it is embedded (air or water), with or without absorber material (water) between the detector and the source, to simulate the presence or not of the healthy tissue. All these simulations were done using the detector APiX of 5 x 5 mm^2.

In all the simulations the source volume is implemented as a cylindrical volume. In this volume one point is chosen randoml and the ^{90}Y source emits an electron isotropically.

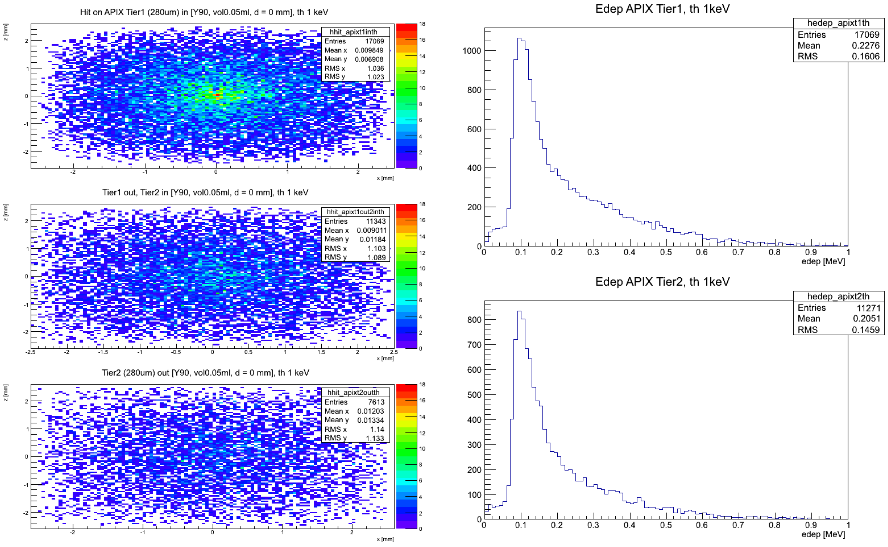

Figure 3.9: An example of the ^{90}Y volume source (in water) spatial distribution of the hits on the detector in different tiers (on the left) and the deposed energy inside tier one and tier two, for a detector threshold set at 1 keV (on the right). The three plots on the left (from the top to bottom) show the hits on the first tier, at the exit of the first tier and on the second tier, respectively.

3.3.3.1 Large cylindrical volume source

The first simulations were done using a cylindrical volume source of total volume 0.05 ml. The cylinder has a diameter of 5 mm and a height of 2.5 mm. This source is placed on the top surface of the detector (so there is no absorber between the source and the detector) and the

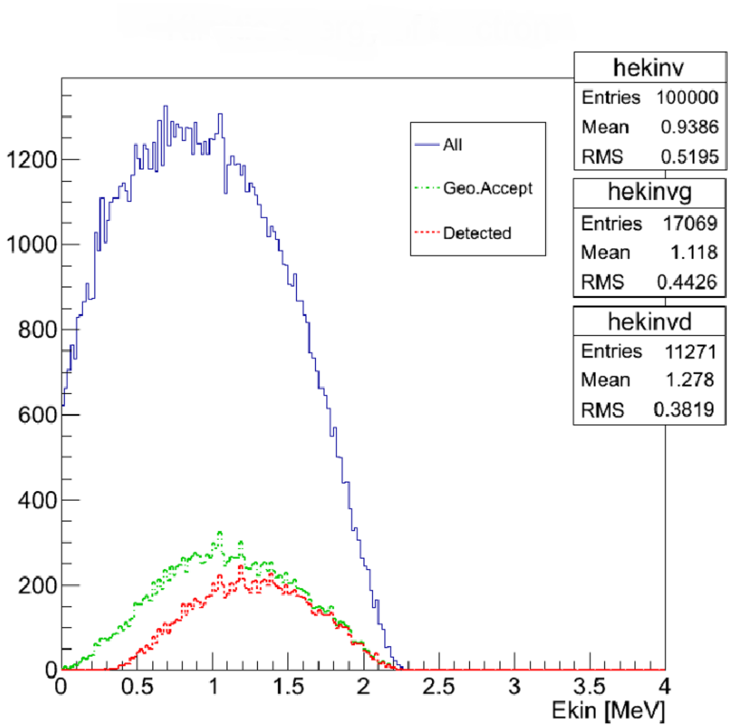

Figure 3.10: Spectral distribution of hits in the detector versus the kinetic energy of the ^{90}Y source electrons. Events from the source emission are shown (in blue), together with the ones that hit the surface of the detector (in green) and the ones detected (in red). These events are simulated assuming that the source is in water.

simulation is carried out with 10^4 events. The total thickness of the simulated detector is 280 + 280 μm and two different cases are considered: source in air and source in water. The second case is intended to simulate the presence of healthy tissue. The results of these simulations are shown in the Figs. 3.7, 3.8, 3.9 and 3.10, with plots of the hits, the energy spectra and the efficiency versus the energy of the electrons emitted, respectively in air and in water.

In the same configuration, values of geometrical and intrinsic efficiency are calculated when the source is simulated in air or in water. In particular, the intrinsic efficiency is almost the same 67% and 66%, respectively in air and water, instead the geometrical efficiency is 21% in air and 17% in water. When the first tier is thinner, for example 100 μm + 280 μm, the intrinsic efficiency increases to 85% and the geometrical one to 18%.

3.3.3.2 Small cylindrical volume source

These simulations are done using a smaller cylindrical volume source of total volume 0.002 ml (25 times smaller than in the case of the previous subsection). The cylinder has a diameter of

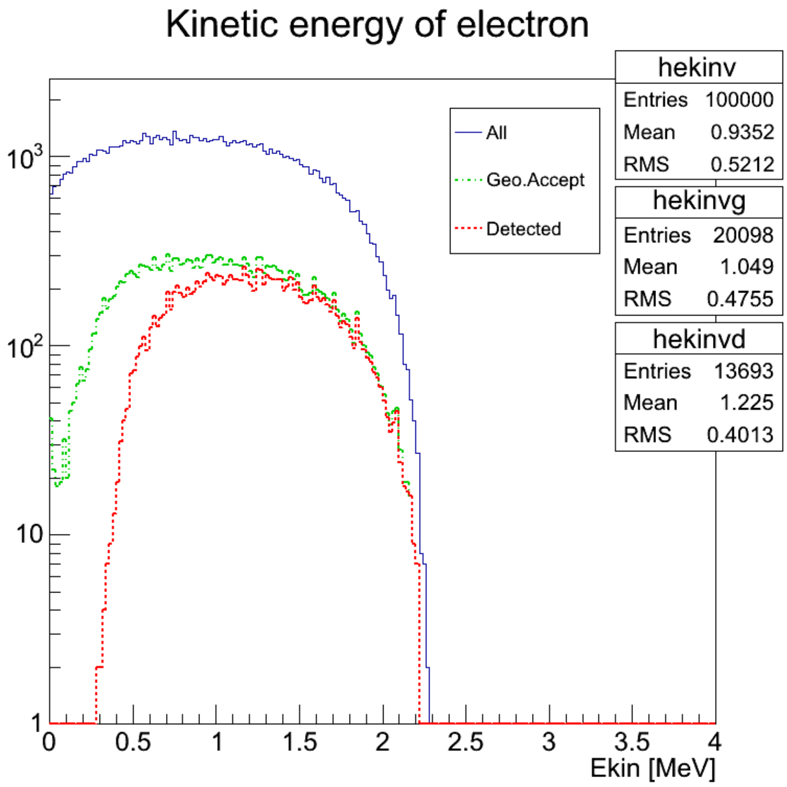

Figure 3.11: Small cylindrical source case 1. Spectra of hits on the detector versus the kinetic energy of the ^{90}Y source electrons: the total events simulated (in blue), the ones that hit the surface of the detector (in green) and the ones detected (in red). These events are simulated assuming that the source is in water and without absorber.

1 mm and a height of 2.5 mm. This source is embedded in water and 10^4 events are simulated.

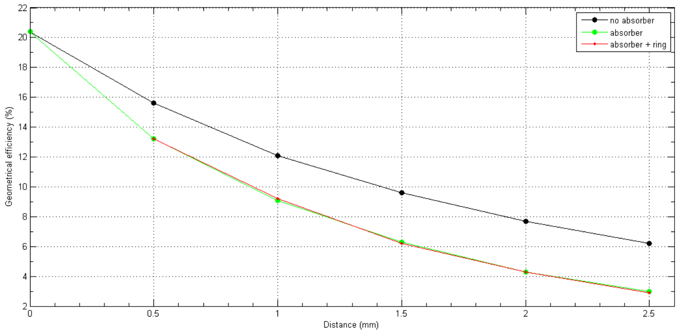

Figure 3.12: The geometric efficiency for different distances in the three different simulation conditions: in black the data without absorber, in green the ones with the absorber and the red ones simulating the absorber and the ring.

Three different simulations were carried out with this setup:

- The source is simulated to be at different distances from the top of the detector and there is air between the detector and the source. This setup is called "no absorber" case.
- The source is simulated to be at different distances from the top of the detector and between the two there is a given thickness of water. This setup is called "absorber" case.
- The source is simulated to be at different distances from the top of the detector, between the two there is a given thickness of water and the source is surrounded by a ring of water. This setup is called " absorber and ring" case.

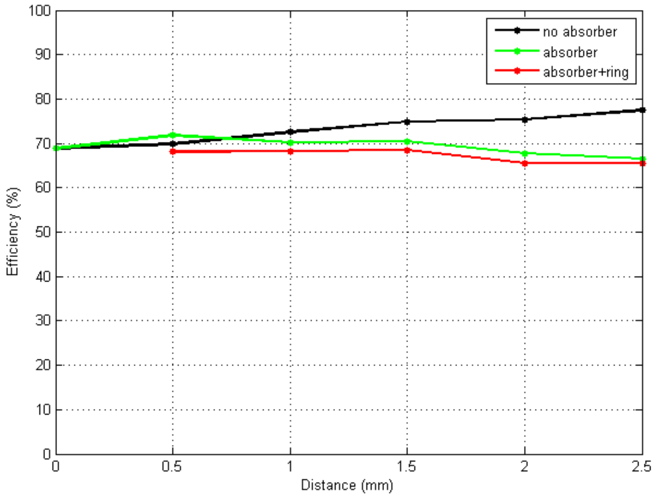

Figure 3.13: The intrinsic efficiency for different distances in the three different simulation conditions: in black the data without absorber, in green with the absorber and in red with the absorber and the ring.

For all the cases, the distances simulated are from 0 to 2.5 mm in steps of 0.5 mm. In the "no absorber" case the material between the source and the detector is air, instead for the other two cases the material is water to simulate the healthy tissue between the detector and the tumoral tissue. The difference between the second and the third case (without and with ring) is that in the third case there is a ring of water around the cylindrical source.

Fig.3.11 shows the spectra of electrons at the source (blue), those hitting the surface of the detector (green) and detected events (red), simulating the cylindrical source positioned on the top of the detector. Under these conditions a geometrical efficiency of 20% and an intrinsic efficiency of 68% are found.

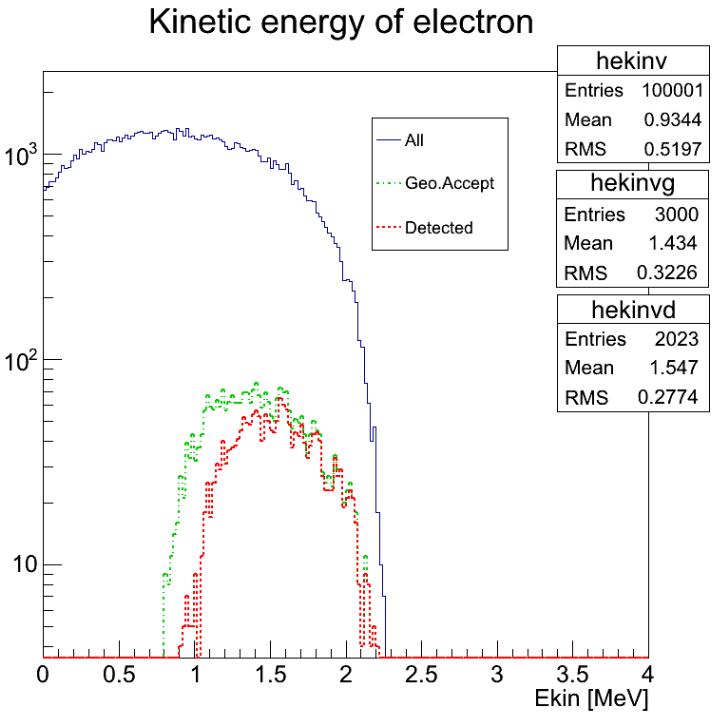

1

Figure 3.14: Small cylindrical source case 2. Spectra of hits on the detector versus the kinetic energy of the electrons: the total events simulated (in blue), the ones that hit the surface of the detector (in green) and the ones detected (in red). These events are simulated assuming that the ^{90}Y source is in water (to simulate the healthy tissue) and there is a thickness of 2.5 mm of absorber (water) between the source and the detector.

Next we study the geometrical and total efficiencies at different distances of the volume source from the detector, without absorber in between. In particular, the simulated distance is from 0 to 2.5 mm far from the top of the detector, in steps of 0.5 mm. The results are shown in the Figs.3.12 and 3.13, for the geometrical and intrinsic efficiency, respectively. As shown in these plots, in this case, moving the source from the top of the detector to a distance of 2.5 mm far from it, the geometrical efficiency varies from 20.4% to 6.2%, instead the intrinsic detector efficiency remains almost constant around 70% (Fig.3.13).

Considering the second case of the simulation (i.e. absorber case), inserting a water absorber of 2.5 mm to simulate the healthy tissue between the cylindrical source and the detector, the intrinsic efficiency is still 68%, but the geometrical one decreases from 20% (at the top of the detector) to 3%. The spectra of the hits in this condition are shown in the Fig.3.14.

The total efficiency is almost constant for different source-detector distances at fixed energy of the electrons and without absorber in between, as it is shown in the Fig.3.15.

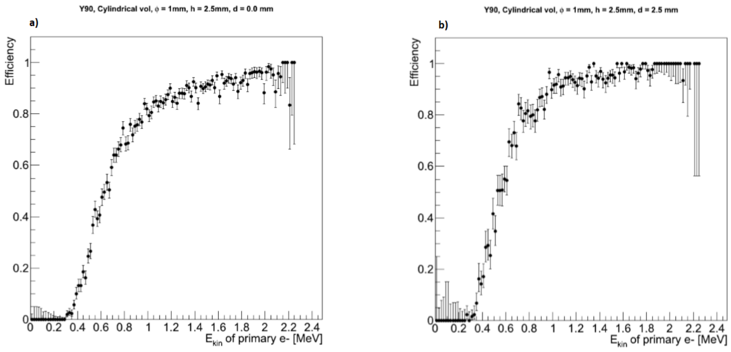

Figure 3.15: The intrinsic efficiency versus the kinetic energy of the electrons emitted from the ^{90}Y source positioned at two different distances from the detector: (a) on the top of the detector (d=0 mm) and (b) at a distance of 2.5 mm from the surface of the detector. As shown in this picture the intrinsic efficiency is almost the same for different source - detector distances.

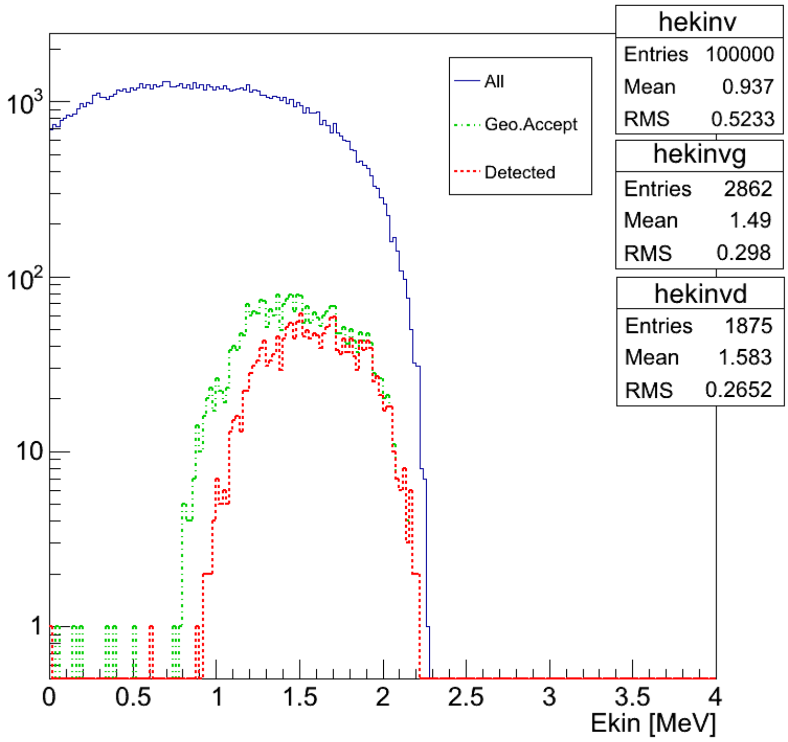

Figure 3.16: Small cylindrical source case 3. Spectra of hits on the detector versus the kinetic energy of the ^{90}Y source electrons: the total events simulated (in blue), the ones that hit the surface of the detector (in green) and the ones detected (in red). These events are simulated considering the source in water (to simulate the healthy tissue) and there is an absorber (water) of thickness 2.5 mm between the source and the detector and a ring of water of 2.5 mm around the source.

In the third case, the source is surrounded by a "ring" of water and the other conditions are the same as in the second case. In the Fig.3.16, there is an example of the result of a simulation at a distance of 0.5 mm from the top of the detector. As shown in the Figs.3.12 and 3.13 (in red colour) the efficiencies are almost similar to the second case.

Chapter 4

Laboratory tests with a radioactive source

This chapter summarizes the measurements carried out in our laboratory with a radioactive beta source to characterize the APiX detector under test. Dark counts and source counts were recorded using the trigger mode, with and without collimator. The data were corrected for the dark counts background and images of the detector area illuminated through the collimator were reconstructed.

4.1 Dark count rate

In order to study the dark count rate, random trigger mode measurements are taken in two different ways: using an external scintillator and with a pulse generator. In the first case the trigger is built using the signal of an external scintillator irradiated with a ^{106}Ru disk source, but placed far away from the detector in order to simulate a Poissonian dark count rate. Instead, in the pulsed random mode, the trigger that simulates a random dark count trigger is provided by an Agilent pulse generator at a fixed frequency.

The trigger mode is studied by varying the main readout parameters, in particular the reset time, monostable length and the daq mode. The third parameter defines the clock frequency. Data were recorded using the daq mode with 0.05 MHz and 20 MHz and reset time of 10 μs or 100 μs.

First, dark counts were recorded under different conditions to study the detector and to choose the best set of the parameters to be used for the acquisitions. In particular the parameters under study are:

- the bias of the detector: 19.5 V (23.0 V) versus 20.5 V (24.0 V).
- the DAQ mode: 20 MHz versus 0.05 MHz.

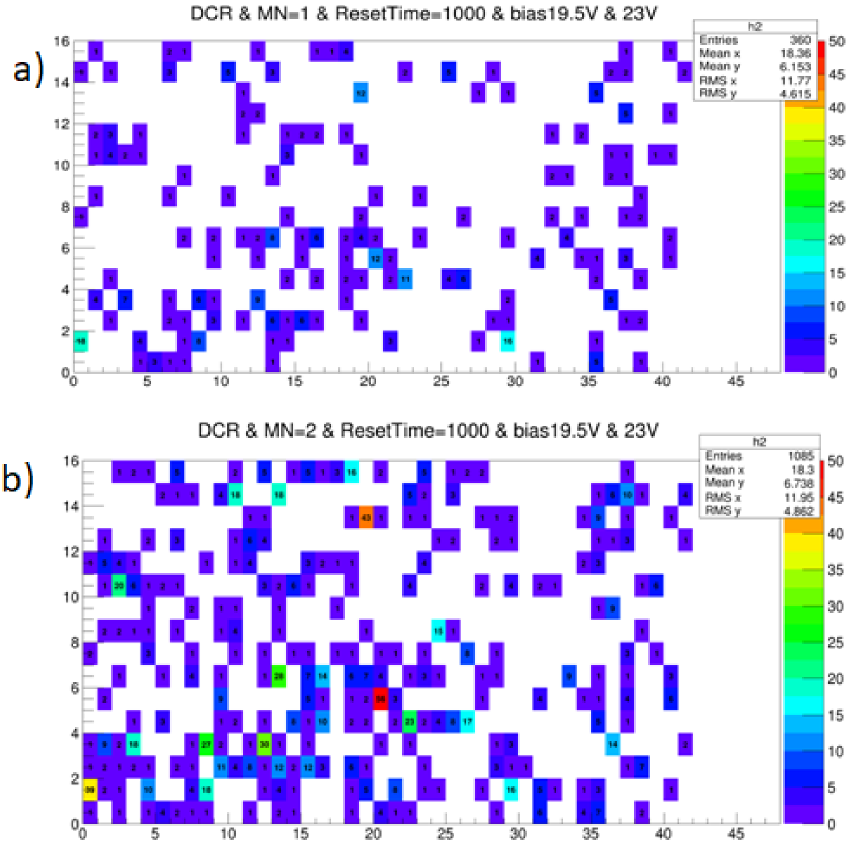

Figure 4.1: In this example the monostable length was changed from 0.75 ns (case a) to 1.5 ns (case b) and the total dark counts increased from 360 to 1085 in a run with 10^6 triggers recorded.

- the monostable length: 0.75 ns versus 1.5 ns.
- the reset time: 1000 (10 μs) versus 10000 (100 μs)

For these preliminary measurements 10^6 total triggers were recorded. The data for each selected parameter are shown: in Fig. 4.1 (monostable length), in Fig. 4.2 (reset time) and in Fig 4.3 (bias of the detector) and summarized in Tab. 4.1.

Varying the DAQ mode from 20 MHz to 0.05 MHz (using 11 different values), the dark count rate is found to be almost the same (as an example for 10^4 triggers we have around 160 ± 10 hits). So, the DAQ mode does not affect the dark count rate as expected.

Using these preliminary results we have chosen a default set of parameters to derive a background correction for all the measurements in the same conditions independently of the overall time duration of the acquisition run. The parameters used are:

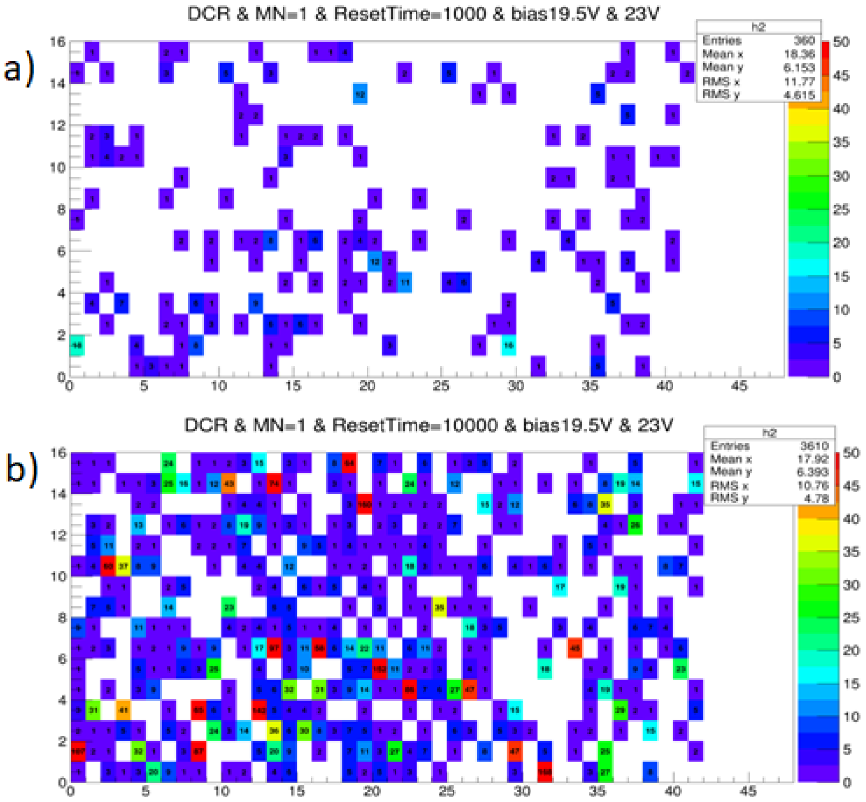

Figure 4.2: In this example the reset time was changed from 10 μs (case a) to 100 μs (case b) and the total dark counts increased from 360 to 3610 in a run with 10^6 triggers recorded. In general, when all other parameters are kept fixed, an increases of the reset time corresponds to a proportional increase of the dark counts, as expected.

- Detector bias at 20.5 V (C1 type detector) and 24.0 V (C2 type detector), that corresponds to about 3.0 V of overvoltage for both sub-sectors of the detector.
- Monostable length 1, equivalent to 0.75 ns.
- Reset time 1000, equivalent to 10 μs.
- Daq mode 0.05 MHz.
- Total triggers $5 \cdot 10^6$.

The total live time of the measurement is 27.2 s corresponding to $5 \cdot 10^6$ random triggers. Fig.4.4 shows the distribution of the dark count rate of the detector. The total hits on the APiX detector are about $1.5 \cdot 10^4$.

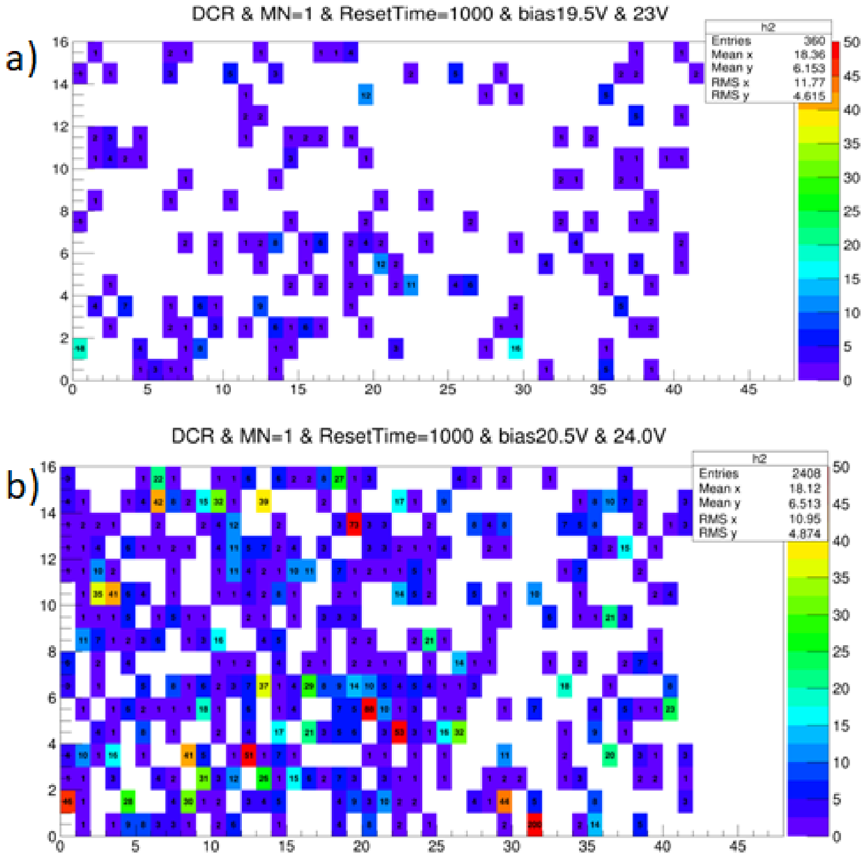

Figure 4.3: In this example, when the overvoltage is increased by 1 V (from 19.5 V to 20.5 V in one sector and from 23.0 V to 24.0 V in the other one), the total dark count events increases from 360 to 2408 in a run with 10^6 triggers recorded. As expected, when all other parameters are kept fixed, increasing the overvoltage produces an increase in the dark count rate.

Fig.4.5 shows the pixel map distribution of the dark count rate in Hz and Fig.4.6 the pixel dark count rate distribution in Hz. In these plots we can notice that 92% of the pixels have less than 20 Hz and 84% have less than 10 Hz occupancy.

The matrix plotted in Fig.4.5 is used to correct the data collected with the radioactive source by subtracting the dark counts. In this way it is not necessary to acquire the dark count spectrum each time. In order to be able to apply a background subtraction procedure the run configuration parameters have to be the same for the background data and when the source is positioned above the detector. We can use this background correction matrix to discard the "hot pixels" (with occupancy larger than a threshold value, for example 20 Hz).

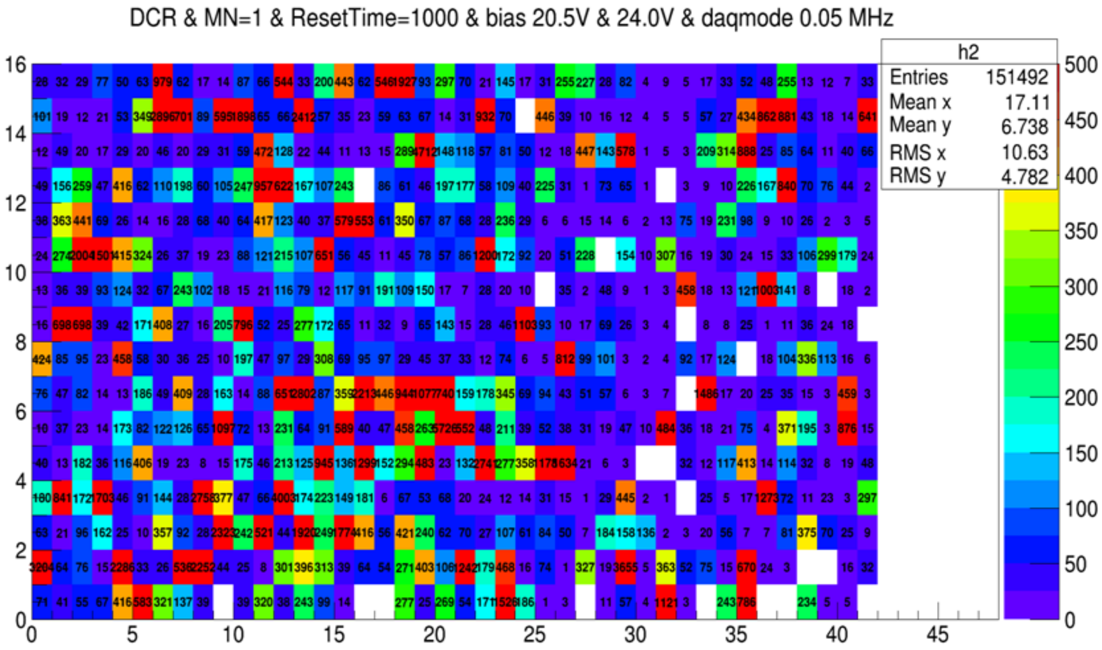

Figure 4.4: Pixel count map of the dark count spatial distribution on the detector using an external scintillator placed far away from the APiX sensor to generate uncorrelated triggers. Pixel counts correspond to a run where 5 $\cdot 10^6$ triggers were collect for a total live time of 27.2 seconds. The rate of the external scintillator was 650 Hz and the measurement parameters are: monostable length 0.75 ns, reset time 1000 and DAQ mode 0.05 MHz.

COMMENTS	**Dark counts**
Coincidence window 0.75 ns vs 1.5 ns	360 vs 1085
Reset time 1000 vs 10000	360 vs 3610
Bias 19.5 V (23.0 V) vs 20.5 V (24.0 V)	360 vs 2406

Table 4.1: Measurements of dark counts as a function of some selected parameters as: monostable length, reset time and the bias of the detector. The total trigger recorded are 10^6 for a live time of about 5 seconds and DAQ mode of 20 MHz. The distributions are shown in Figs. 4.1, 4.2 and 4.3.

4.2 Measurements with a radioactive source

Measurements were carried out with a disk shaped ^{106}Ru radioactive source, whose geometric parameters are shown in Fig.4.7. It is a sealed (β, γ) disk source with diameter of

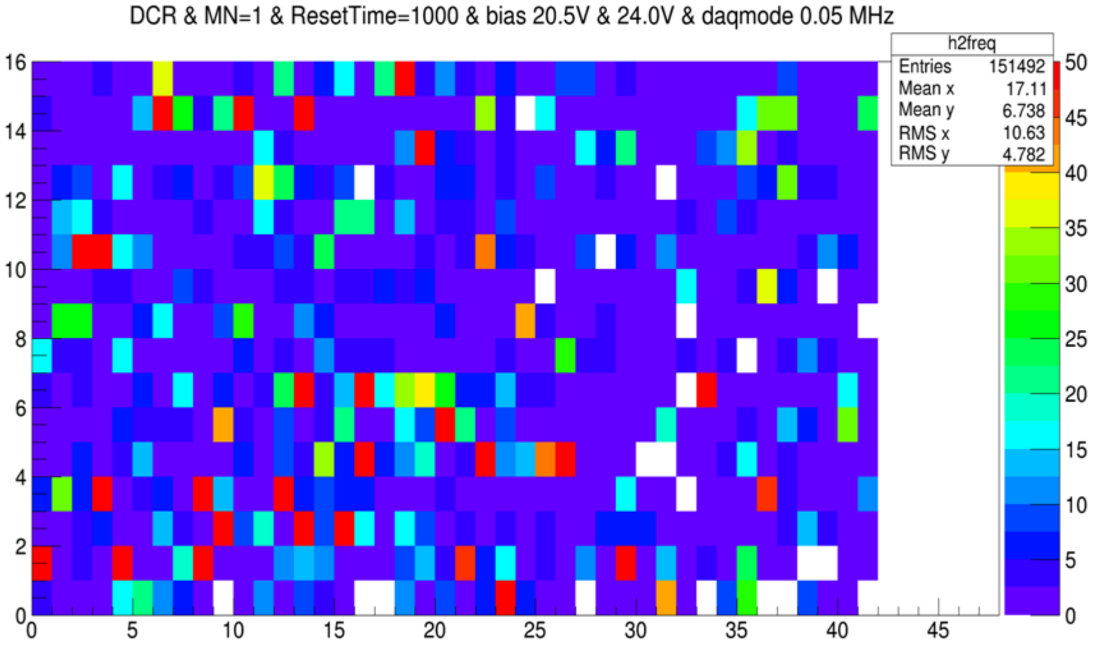

Figure 4.5: Pixel map of the dark count rate distribution (in Hz) of the detector using an external scintillator to generate uncorrelated triggers for the LAC board. In this run 5 $\cdot 10^6$ triggers were collect for a total live time of 27.2 seconds. The rate of the external scintillator is 650 Hz and the measurement parameters are: monostable length 0.75 ns, reset time 1000 and DAQ mode 0.05 MHz.

(25.654 ± 0.254) mm and thickness of 3.175 mm. It had a 37 kBq activity in March 2020.

The Fig.4.8 shows a picture of the final setup used in laboratory measurements. In the picture, it is shown: (a) the source setup using the first position transaltor, (b) the cross-section view of the setup, in (c) the picture of the translational stage in which the source, with or without a collimator, is placed, (d) the cross-section view of the scintillator NE102 (3.6 x 3.7 mm^2), coupled to a SiPM NUV FBK (4.0 x 4.0 mm^2), that is used to generate uncorrelated triggers for the LAC board.

Three main different setups were used to characterize the detector where each is the evolution of the previous one. The first translation stage is the one on the top-left of Fig.4.9 (case a), it was made using a 3D printer and it is possible to shift the source or collimator + source only in one direction x or y. In the second version, shown on the top-right of the Fig.4.9 (case b), the translation stage is more stable than the previous one, but we can move the source only in one direction x or y, as in case a). With the last version, shown in the the bottom of the Fig.4.9 (case c), it is possible to move the source with respect to the detector along the x or y directions, independently.

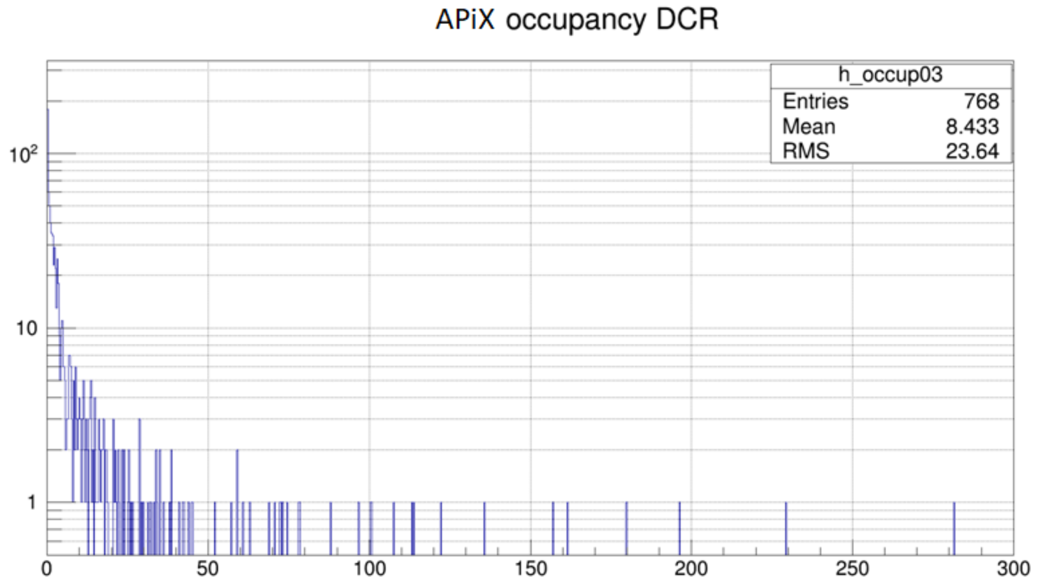

Figure 4.6: Pixel dark count rate distribution (in Hz) of the detector using an external scintillator (placed far away from the detector) to trigger on a Poissonian distribution of the detector uncorrelated external events. A total of 5 $\cdot 10^6$ triggers are recorded for a total live time of 27.2 seconds. The rate of the external scintillator is 650 Hz and the measurement parameters used are: monostable length 0.75 ns, reset time 1000 and daq mode 0.05 MHz.

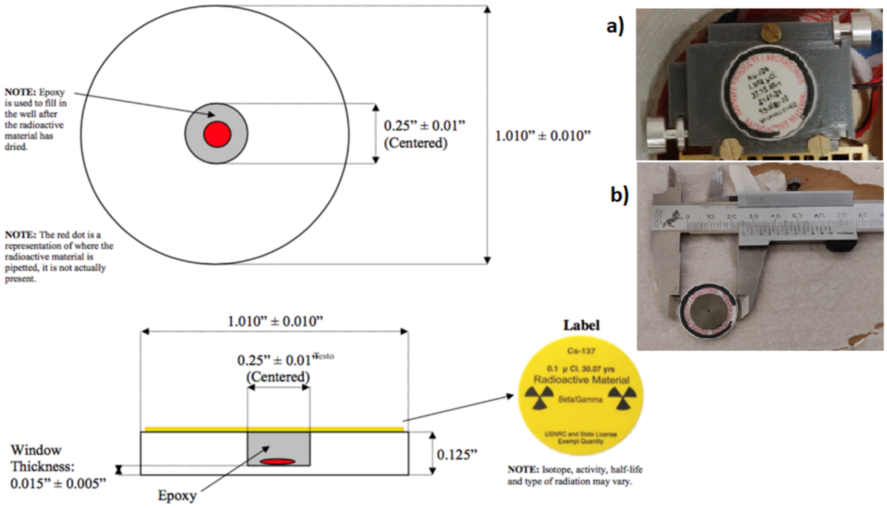

Figure 4.7: Schematic geometry of the sealed (β, γ) disk source used for the measurements. It has a diameter of (25.654 ± 0.254) mm and a thickness of 3.175 mm. In a) the source placed in the translation stage used to move it, instead in b) the source and one of the collimators used during the measurements are shown.

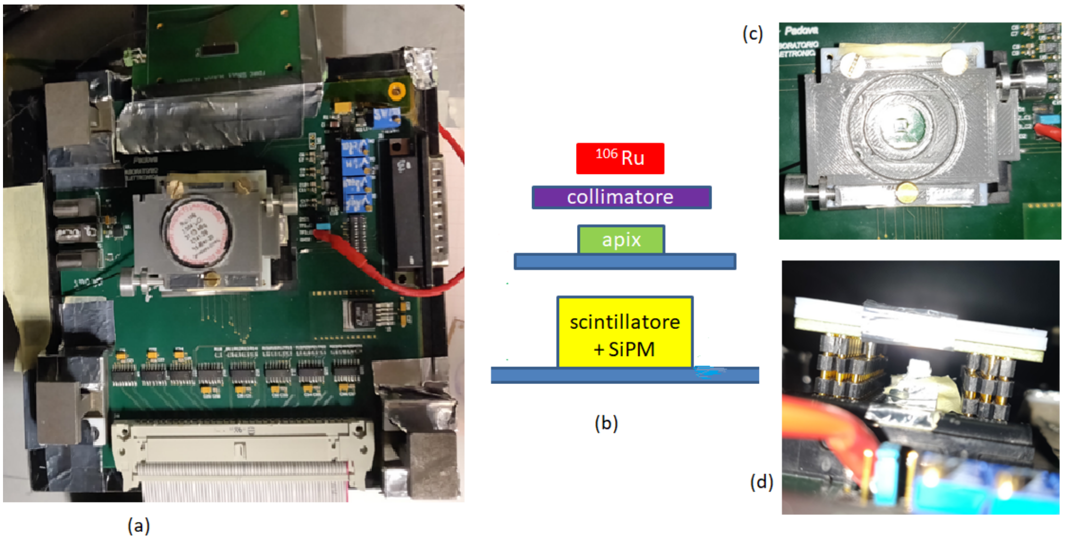

Figure 4.8: a) source setup using the first translation stage, (b)cross-section view of the setup, (c) picture of the translation stage in which the source and collimator are placed and (d) cross-section view of the scintillator that is used to generate the trigger for the LAC board.

We used two different setups for these measurements that are schematized in Fig.4.10. As it is shown in this figure, there are two different relative distances between the source (or source + collimator) and the detector of 1.5 mm (setup 1) and 5.7 mm (setup 2). The distance between the detector and the scintillator (that generates the trigger for the acquisition) was 5.0 mm or 3.5 mm.

4.3 Sensor measurements with a collimated radioactive source

In this section we describe the measurements that were carried out with a collimated source. First, we used a large collimator (1 mm diameter) in the geometrical arrangement labelled as “setup2” in Fig.4.10, where the collimator-sensor distance was 5.7 mm and the plastic scintillator, positioned immediately downstream the sensor and interfaced to a SiPM, provided the trigger. Using the final version (c) of the translation stage, the source could be moved independently along two orthogonal directions and aligned with the sensor. The collimator could be inserted and removed without affecting the reproducibility of the alignment.

The pixel hit map in Fig.4.11 shows the illumination of the detector when the source is positioned approximately at the center of the main sub-section of the sensor. This area is shown (in pale blue color) on the left side of the insert at the bottom of the same picture, where the pixel partitioning of the first prototype is schematically described. This is the area where we

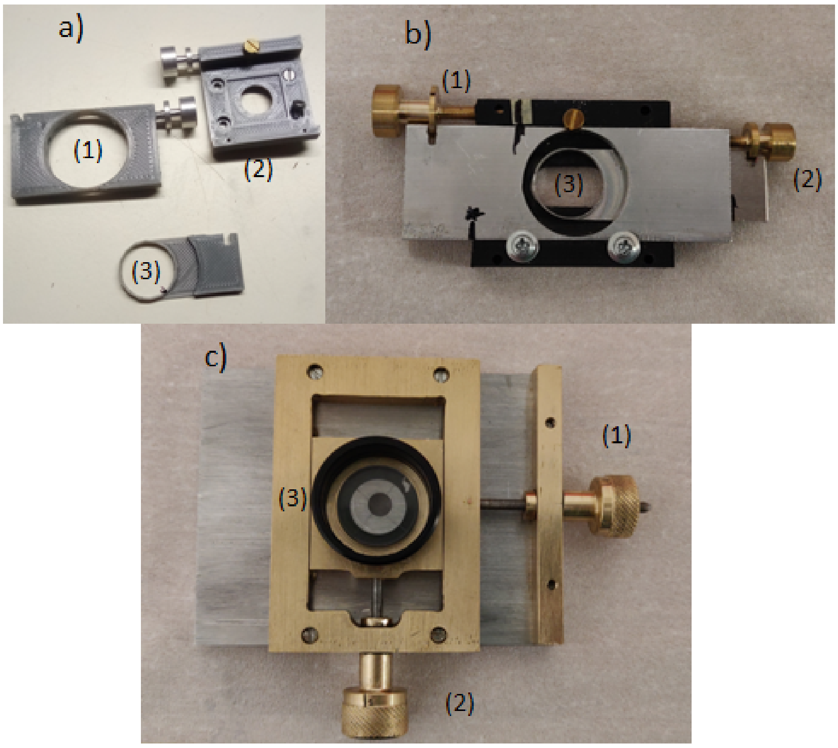

Figure 4.9: Three different setups to characterize the detector: a), b) and c). Each one is the evolution of the previous one and consists of one mechanical part where the source (or the set source+collimator) is held at (3), and of a mechanical gauge for the movement, (1) and (2). With the simplest one, case a), made with a 3D printer it is possible to shift the translation stage only in one direction x or y. In the second version, case b), we can move the source only in one direction x or y, as in case a). Using the last version, case c), it is possible to move the source with respect to the detector independently along the x and y directions using the knobs (1) and (2).

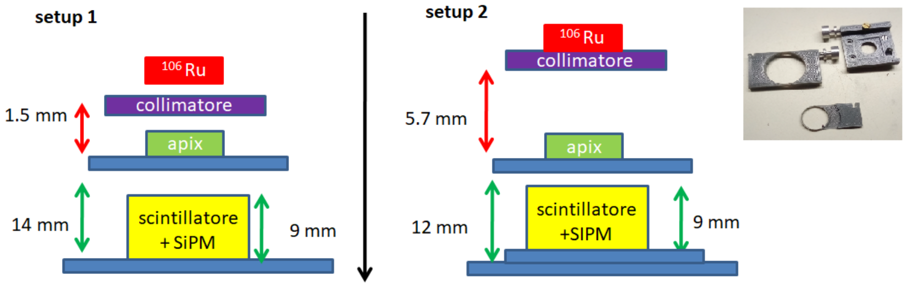

Figure 4.10: The first measurements were done using two different relative distances between the source (or source + collimator) and the detector, of 1.5 mm (setup 1) and 5.7 mm (setup 2), and the distance between the detector and the scintillator (that generates the trigger for the acquisition), of 5.0 mm and 3.5. The translation stage used in both setups is the first version of it (the one produced using the 3D printer).

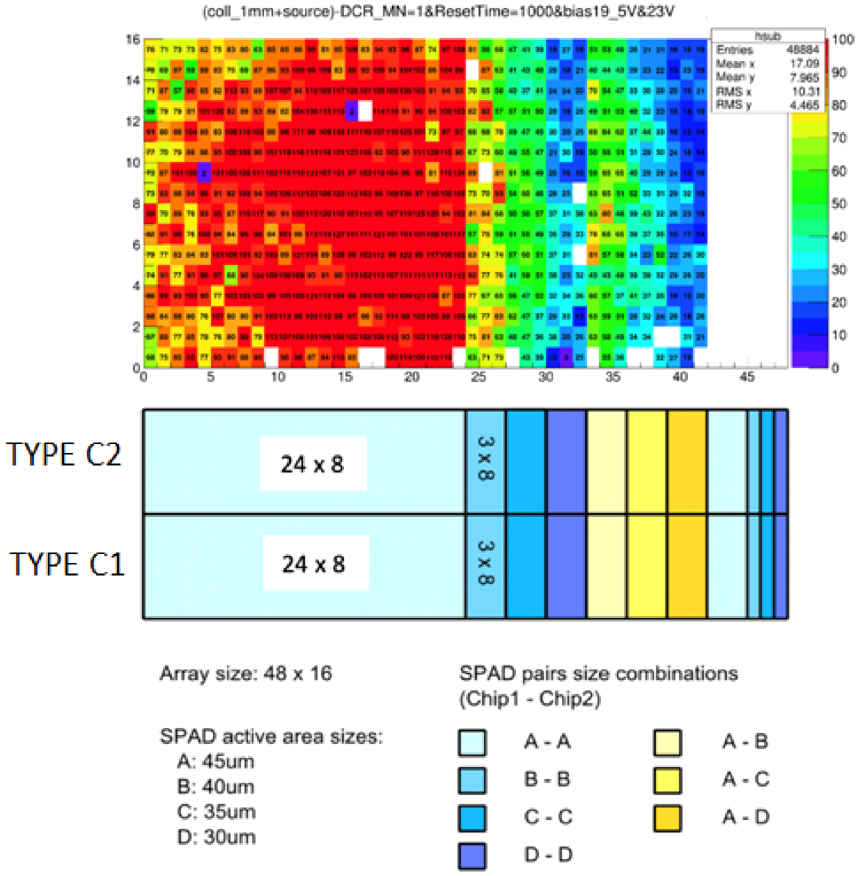

Figure 4.11: This picture shows: (top) pixel hit map when the sensor is illuminated by the source via a 1 mm diameter collimator; (bottom) schematic partitioning of the total sensor area in sub-sections with different pixel size.

focus our attention and it is partitioned into 24 x 16 pixels of size 45 μm x 45 μm, while the right-hand part of the sensor is partitioned into pixels of smaller dimensions according to the color scheme shown in the same picture.

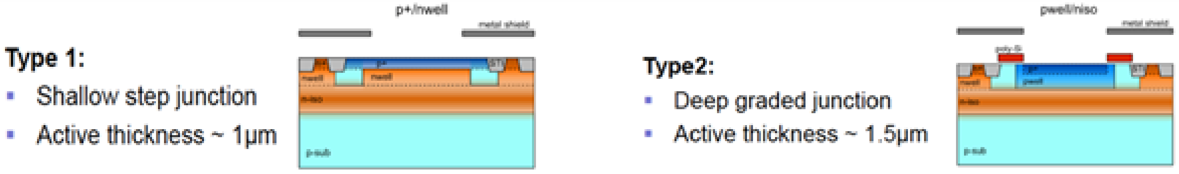

Figure 4.12: Two different fabrication techniques employed for the 45 um x 45 um pixels sensor sub-sections. Each area contains 24 x 8 pixels.

The main area with 45 μm x 45 μm pixels is further subdivided into two regions with 24 x 8 pixels each (Type C1 and C2, respectively). The pixel size is the same for both, but Type

C1 pixels have a shallow step junction with a typical active region depth of 1 um, while Type C2 pixels were manufactured using a deep graded junctions and a slightly thicker active region (1.5 μm) as shown in Fig.4.12.

The large collimator illuminates most of the main sub-section of the sensor and its round edge is visible on the left-hand side of Fig.4.11. This picture was obtained from a data sample of 1 million triggers. The DAQ parameters were: daq mode 20 MHz, reset time 1000, monostable length 0.75 ns. The sensors bias was 19.5V (23.0V) for Type1 (Type2) sections.

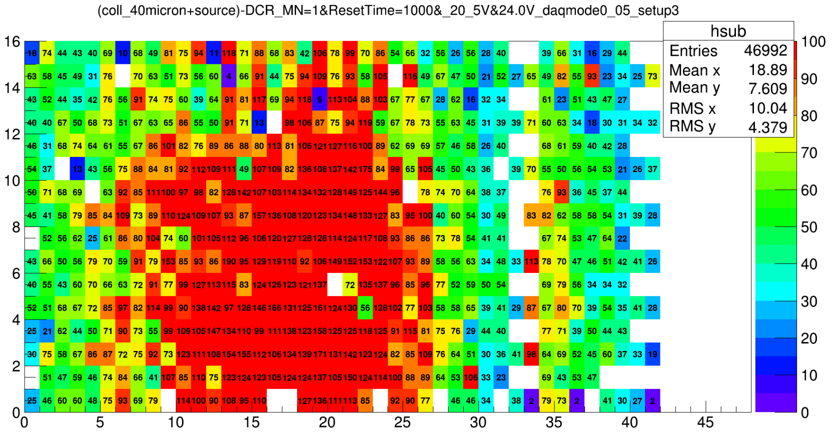

Figure 4.13: Pixel hit map when the sensor is illuminated by the source via a 400 μm diameter collimator.

By illuminating the sensor through a smaller collimator (0.4 mm diameter), the shadow of the collimator is visible in Fig.4.13.

Both pictures were obtained from data samples each corresponding to 10^6 triggers.The DAQ parameters were: DAQ mode 0.05 MHz, reset time 1000, coincidence window 0.75 ns. The sensor bias was 20.5 V (24.0 V) for the Type 1 (Type 2) sections, respectively.

4.4 Measurements with a non collimated radioactive source

In this section we describe the measurements that were carried out without the collimator in order to have an homogeneous radioactive fluence on the detector. All the source data are corrected by applying the DCR background subtraction procedure. The background data are taken with the same parameters used for the runs with the radioactive source.

We have chosen a default set of parameters to collect data to study the response of the pixels of the detector and to equalize it. The selected parameters are:

COMMENTS	**APiX**	**APiX-DCR**	**%**
collimator 1 mm	69448	47703	7.0
collimator 0.4 mm	89656	46992	6.5

Table 4.2: Measurements with the collimated source: the first column gives the raw counts; the DCR background subtracted counts are shown in the second column; the efficiency (averaged over the region of interest of the detector) is shown in the third column where the background subtracted counts are normalized to the number of triggers. Please note that this is NOT the detector efficiency but the effective efficiency (in this run configuration) dominated by the geometric efficiency, trigger efficiency and fill factor.

- Detector bias at 20.5 V (C1 type detector) and 24.0 V (C2 type detector), that corresponds to about 3.0 V of overvoltage for both sub-sectors of the detector.
- Monostable length 1, equivalent to 0.75 ns.
- Reset time 1000, equivalent to 10 μs.
- Daq mode 0.05 MHz.
- Total triggers $5 \cdot 10^6$.

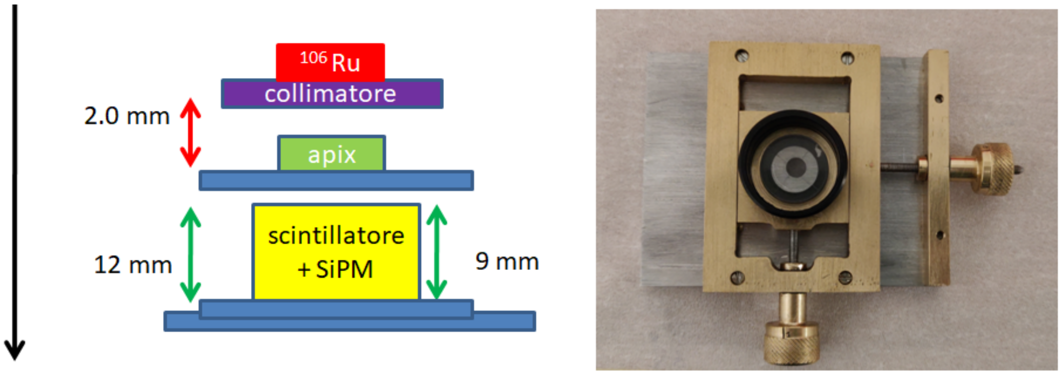

Figure 4.14: The final setup used to collect data with a radioactive source disk above the APiX detector. In this setup the source is closer to the top of the detector and the relative distance between the detector and the translation stage (shown on the right) is 2.0 mm.

The total live time of the measurement is 25.2 s, for $5 \cdot 10^6$ total number of triggers and the data are shown in Fig.4.15. These data are collected using the final setup, shown in Fig.4.14

where the relative distance between the detector and the translation stage (shown on the right) is 2.0 mm.

Fig.4.15 shows the distribution of source data on the detector after the dark count correction. The total hits on the APiX detector, due to the radioactive source, are about $1.4 \cdot 10^5$, and we used these data to calculate the equalization factor for each pixel of the detector.

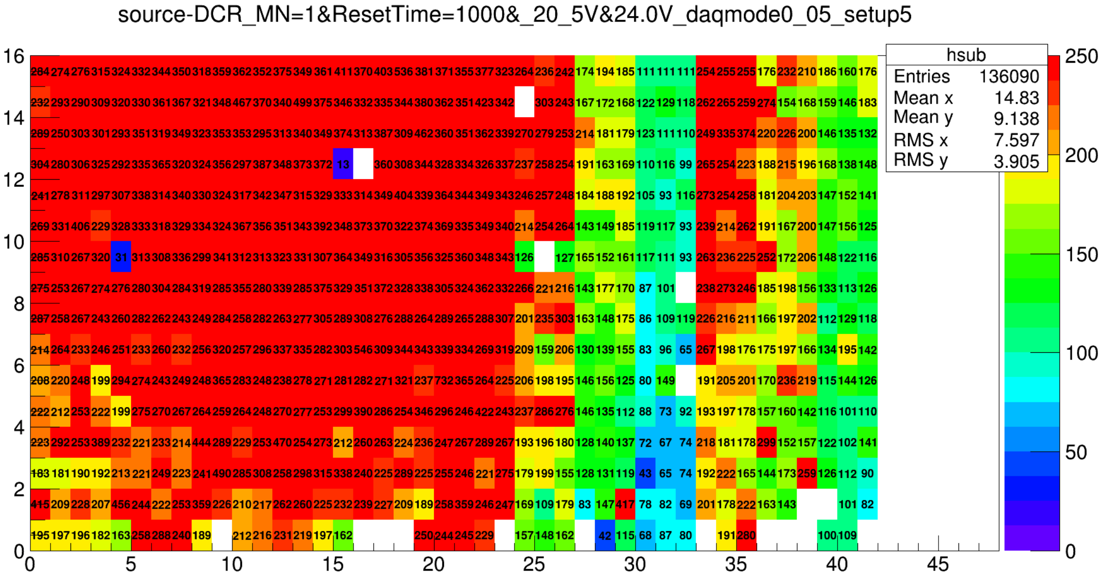

Figure 4.15: Pixel map of $5 \cdot 10^6$ total triggers using the final setup, biasing the detector at 20.5 V (C1 type detector) and 24.0 V (C2 type detector), that corresponds to about 3.0 V of overvoltage for both sub-sectors of the detector. The DAQ parameters are: monostable length 0.75 ns, reset time 1000 and daq mode 0.05 MHz. These data are corrected for the dark count rate.

First, from the data shown in Fig.4.15 the uniformity factor c_i are calculated using the formula 4.1:

$$c_i = \frac{hit_i}{mean_{ROI}} \tag{4.1}$$

where hit_i are the hits of i-th pixel and $mean_{ROI}$ is the mean value of the hits of all the pixels inside our Region of Interest (45 x 45 μm^2 pixels).

Fig.4.17 shows the distribution of the uniformity factor for each pixel for the whole detector. The 45 x 45 μm^2 pixels belonging to the ROI (with pixel number lower than 400) show an almost uniform distribution close to unity. The smaller pixels (with pixel number above 400) have a more complicated distribution due to their variable geometry. The uniformity factor of each pixel in the Region of Interest of the detector is shown in Fig.4.16.

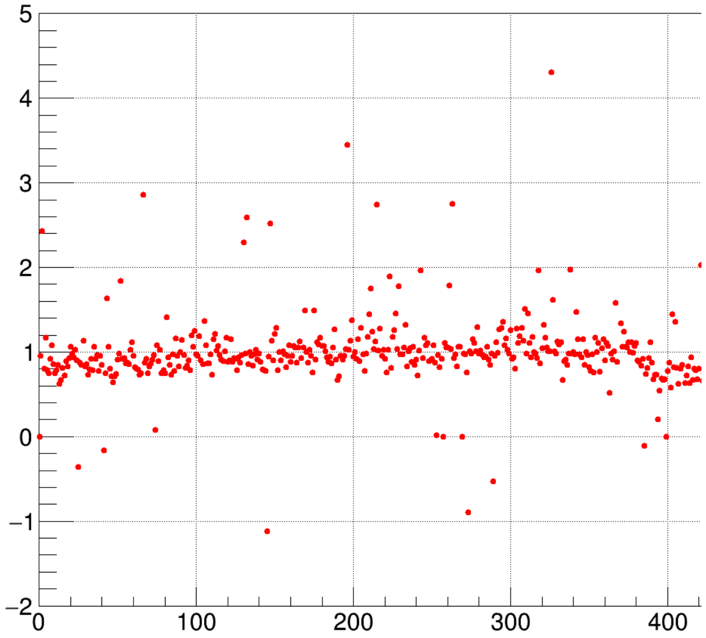

Figure 4.16: The uniformity factor (y-axis) of each pixel in the Region of Interest of the detector.

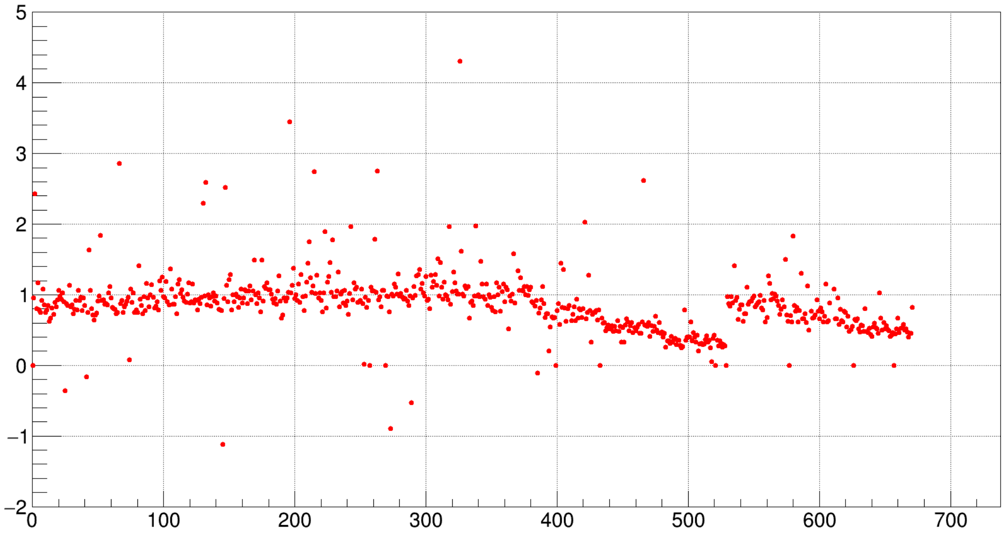

Figure 4.17: The uniformity factor for each pixel (x-axis) versus the pixel number for the whole detector. The 45 x 45 μm^2 pixels belonging to the ROI (with pixel number lower than 400) show an almost uniform distribution of uniformity factors close to unity. The smaller pixels (with pixel number above 400) have a more complicated distribution due to their variable geometry.

We use these uniformity factors to calculate the equalization factor for each pixel of the detector defined as:

$$Keq_i = \frac{1}{c_i}$$

Fig.4.18 shows the pixel map of the equalization factor over the whole detector. It can be noticed that the equalization factor is almost uniform and close to 1.0 inside the ROI, (see Fig.4.16).

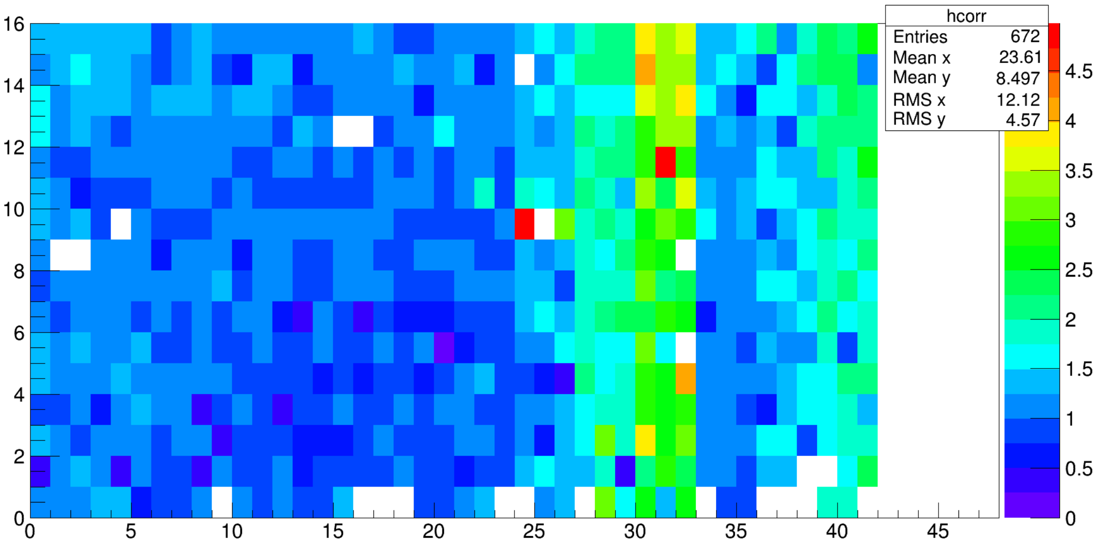

Figure 4.18: Pixel map of the equalization factor over the whole detector. It can be noticed that the equalization factor Keq_i is almost uniform and close to 1.0 inside the ROI, (see Fig. 4.16), while for smaller pixels it assumes larger values because of their lower uniformity factor c_i (see Fig. 4.17).

In conclusion, our present laboratory tests with a beta source confirm that the first APiX prototype is able to image the spatial distribution of the electrons that pass through the collimator. Though the detector efficiency is relatively high (as confirmed by the BT measurements) the effective overall efficiency obtained during the radioactive source tests is less than 10% (dominated by the geometrical factor of the setup) therefore, given the large granularity of the detector, a very large statistics is needed to get a high resolution profile of the edge of the collimator. The preliminary image in Fig.4.13 with the small (0.4 mm) collimator can be largely improved in terms of contrast, but this requires significantly longer acquisition times.

Chapter 5

5.1 Conclusion and perspectives

This thesis describes the development and characterisation of a novel CMOS digital imaging sensor for the detection of ionizing radiation, which was developed by the ASAP collaboration, within the framework of the R&D activities supervised by the Scientific Commission 5 of INFN (Istituto Nazionale di Fisica Nucleare).

The APiX sensor has a number of attractive features for its potential application in radio-guided surgery (RGS). Its self-triggering capability allows its use as a stand-alone handheld device (RGS probe). It can be operated without an external triggering system. However, it may be convenient to integrate the sensor with an external scintillator of larger size, placed downstream the sensor and optically coupled to a SiPM (as implemented in the prototype described in paragraph 2.7). This configuration allows to perform a quick scan of the surgery field, by recording simultaneously the information provided by an integrating counter with visual mapping from the imaging device. In this way, the counting rate of the large scintillator is available at any moment during surgery allowing the identification of the position and overall size of a region-of-interest (ROI), while simultaneously imaging the same field with the CMOS sensor. In this way, after a quick scan to assess the general morphology of the radiation field on the basis of the counting rates, the surgeon can decide in real time to stop the scan and acquire data in a given location in order to build a detailed image of a particular sub-structure or to examine the boundaries of a lesion.

In principle, the CMOS probe described in this thesis can provide high resolution images, given its high granularity with small pixels of 75 μm. However, as we shall discuss in more detail below, the image contrast depends dramatically on the local activity of the β^- radiation field emitted from the ROI and this poses severe limitations to the image sharpness, given to the very limited time (a few seconds) available to the operator to acquire an image while the sensor is kept at a fixed position during a scan.

Another advantage is that the sensor provides an intrinsic directional sensitivity to the impinging β^- radiation within a limited field of view (of about $\pm 15°$). This is due to the working principle of the detector which is based on the coincidence of pairs of vertically aligned pixels located on two layers spaced by the thickness of the first layer (typically from 50 to 150 μm). The auto-collimation capability of the detector can be of advantage in order to discriminate electrons emerging from a portion of the tissue, located just below the entrance window, against the diffuse background due to the ionizing radiation emitted in all directions from the nearby sources.

The sensor threshold depends entirely on the thickness of the first layer which has to be totally traversed by the incident electron in order to be able to generate a coincidence on the second layer (the sensitive region in the second layer is just a few micron below the surface). The current detector prototype is 150 μm thick with a threshold close to 0.5 MeV which is adequate for a source spectrum as the one from a 90^Y or 106^Ru radiation source (the latter peaking at 1 MeV and with an endpoint at about 3 MeV). However, the detector threshold can be lowered if the first layer is thinned down to 100 μm or less (a thickness as low as a few tens micron can be achieved). This is due to the fact that the sensor works in avalanche mode whereby charge multiplication takes place in a shallow region 1 or 2 micron thick, located near the junction. In principle, the detector is "window-less" in that no significant amount of absorbent material is located at the entrance window of the probe. However, it is recommended to place a very thin plastic film on top of the entrance window to protect the sensor during its operation in the surgery field.

5.1.1 Sensor requirements

In order to establish the requirements for an improved version of the present probe prototype we have first to take at face-value the limited available activity of the source of β^- radiation in a realistic RGS scenario. In the following, we refer to the clinical studies performed by [29] with an integrating probe, providing counting rates but having no imaging capabilities. The probe, equipped with a cylindrical scintillator (Φ = 5 mm, depth=3mm), was employed during the RGS resection of a pancreatic tumor in the presence of a residual activity of 105 MBq (for 70 Kg body mass) after 24 hrs from the administration of ^{90}Y DOTATOC. The typical observed count rates ranged from few tens to hundreds Hz/mm2 with a large variability. Within the limits of an order-of-magnitude estimate, we can assume a signal rate (from the tumoral tissue) with a large variability from about 20 to 200 cps (or more) with a background rate from healthy tissue in the range 10-20 cps.

In the above study, the authors suggest that a "realistic" exposure time for each scan position of the probe should be limited to 10 seconds (a reference value of 3 s is recommended). Is is straightforward to calculate the expected rates for a CMOS sensor of larger size than our present prototype with square pixels of 100 micron/side, taking into account that "super-pixels" of even larger size can be easily obtained by pixel re-summation in real-time with negligible effect on image processing dead-time and S/N degradation. By scaling the measured rates reported in [29] (which were obtained with a probe with nominal sensitive area of $\sim 20 mm^2$), to an effective area of 100 mm2 for a CMOS probe with super-pixels of 0.5 x 0.5 mm^2, we get an expected median pixel count rate of about 500 cps. A spatial resolution of the order of 1 mm could in principle be achieved, but the image contrast has to be evaluated carefully, as it depends critically on the exposure time.

5.1.2 Implementation of the RGS imaging probe

The front-end coincidence circuits integrated in the sensor require a completely negligible amount of power. A small-sized interface board located inside the probe body relays LVDS signals to the external readout system along a single cable stemming from the tail of the probe. Alternatively, a wireless readout system has been implemented in a prototype under development by the group at University of Pavia participating in the ASAP project. The only significant source of power comes from the cooling system of the sensor head based on small Peltier cells. Cooling is not mandatory, but it can be of advantage as the DCR can be reduced approximately by a factor 2 for each decade of temperature drop thereby increasing the signal-to-noise ratio.

5.2 The role of the candidate in the present work

Arta Sulaj joined the experimental group directed by prof. P.S. Marrocchesi at the University of Siena and INFN Pisa, after achieving a degree in Physics at the University of Pisa and a Specialisation Diploma in Medical Physics. She first worked with silicon strip and pixels sensors that were used as the building blocks of a particle tracker developed by the group and employed during several beam test campaigns at CERN. In particular, the high dynamic range of the pixel sensors and of the associated readout electronics [30] allows the charge identification of individual elements in a beam of ion fragments at the SPS [31], [32], [33], where elements from proton to iron can be individually identified (the charge range of the system allows to identify elements up to atomic number Z=40).

Arta Sulaj participated in the development, characterization and beam test of a scintillation hodoscope for the CALET experiment [34] which was installed on the International Space Station (ISS) in 2015. She also contributed in the development of scintillator prototypes with optical readout by Silicon Photo-Multipliers [35], in the direct detection of charged ions with SiPMs [36], and in the construction and test of a prototype of an FDIRC (Focused Internal Reflection Cherenkov) detector optically readout by an array of 1024 SiPMs [37].

During this period, she gained considerable skills in mastering lab instrumentation and its remote operation and control with LabView, detector data readout/monitoring, and offline analysis. She focused her PhD thesis work by actively participating in the development of the first APiX protoype [24], [26], [38] and of the mechanical and electronics interfaces for its characterisation and test in Pisa and Siena laboratories. The construction of several improved versions of a 3-D printed probe was accompanied by a large series of lab tests with a radioactive source and by a beam test at CERN where four APiX stations were integrated in the beam tracker [39].

The laboratory test of the APiX sensor required the setup of a special test stand (as described in this thesis) where the relative geometry of the source, collimator, APiX sensor and SiPM-coupled scintillator could be kept under control in a reproducible way. This required the development of precision mechanics and custom translational stages which were developed at the University of Siena by L.Stiaccini. The design and 3-D printing of the probe was carried out by A.Basti at INFN - Pisa. The expected performances of the APiX sensor were valuated on the basis of a Monte Carlo code, based on GEANT4, which was developed by J.E.Suh and P. Brogi.

Given the small geometrical size of the first prototype of the APiX sensor ($\sim 1mm^2$), the laboratory tests with a Ru source, had to be very accurate in terms of geometrical alignment and control of the solid angle. A long campaign of tests was carried out by A.Sulaj who tested the performance of the sensors under different geometrical conditions, trigger conditions (external SiPM trigger or self-triggered) and run modes ("triggered-mode" or in the so-called "Geiger mode", a free-running mode where events are acquired continuously and the corresponding images refreshed at regular intervals on the monitor display). A complementary set of accurate measurements were carried out by A.Sulaj relative to the study of the DCR under different experimental conditions in order to maximize the signal-to-noise ratio.

The offline analysis of the data was performed by A.Sulaj and the results were compared with the MC simulations. Predictions on the expected performances of the probe in a realistic scenario of RGS were also derived. Currently, a second-generation APiX sensor, with a larger active area, has successfully passed all characterisation tests and will be integrated in a second probe prototype.

List of Figures

List of Tables

Bibliography

[1] P. Waelkens, M. N. van Oosterom, N. S. van den Berg, N. Navab, and F. W. van Leeuwen, "Surgical navigation: An overview of the state-of-the-art clinical applications", in *Radioguided Surgery*, Springer, 2016, pp. 57–73.

[2] S. P. Povoski, "The history of radioguided surgery: Early historical milestones and the development of later innovative clinical applications", in *Radioguided Surgery*, Springer, 2016, pp. 3–12.

[3] E. J. Hoffman, M. P. Tornai, M. Janecek, B. E. Patt, and J. S. Iwanczyk, "Intraoperative probes and imaging probes", *European journal of nuclear medicine*, vol. 26, no. 8, pp. 913–935, 1999.

[4] T. Wendler, U. Eberlein, and M. Lassmann, "Physics of radioguided surgery: Basic principles and methods of radiation detection", in *Radioguided Surgery*, Springer, 2016, pp. 15–33.

[5] S. R. Cherry, J. A. Sorenson, and M. E. Phelps, *Physics in nuclear medicine e-Book*. Elsevier Health Sciences, 2012.

[6] L. Katz and A. S. Penfold, "Range-energy relations for electrons and the determination of beta-ray end-point energies by absorption", *Reviews of Modern Physics*, vol. 24, no. 1, p. 28, 1952.

[7] A. Bunschoten, N. S. van den Berg, R. A. V. Olmos, J. A. Blokland, and F. W. van Leeuwen, "Tracers applied in radioguided surgery", in *Radioguided Surgery*, Springer, 2016, pp. 75–101.

[8] S. P. Povoski, R. L. Neff, C. M. Mojzisik, D. M. O'Malley, G. H. Hinkle, N. C. Hall, D. A. Murrey, M. V. Knopp, and E. W. Martin, "A comprehensive overview of radioguided surgery using gamma detection probe technology", *World journal of surgical oncology*, vol. 7, no. 1, p. 11, 2009.

[9] V. E. Strong, J. Humm, P. Russo, A. Jungbluth, W. D. Wong, F. Daghighian, L. Old, Y. Fong, and S. M. Larson, “A novel method to localize antibody-targeted cancer deposits intraoperatively using handheld pet beta and gamma probes”, *Surgical Endoscopy*, vol. 22, no. 2, pp. 386–391, Feb. 2008, ISSN: 1432-2218. DOI: `10.1007/s00464-007-9611-3`. [Online]. Available: `https://doi.org/10.1007/s00464-007-9611-3`.

[10] D. A. Heuveling, A. van Schie, D. J. Vugts, N. H. Hendrikse, M. Yaqub, O. S. Hoekstra, K. H. Karagozoglu, C. R. Leemans, G. A. van Dongen, and R. de Bree, “Pilot study on the feasibility of pet/ct lymphoscintigraphy with 89zr-nanocolloidal albumin for sentinel node identification in oral cancer patients”, *Journal of Nuclear Medicine*, vol. 54, no. 4, pp. 585–589, 2013.

[11] F. Collamati, A. Pepe, F. Bellini, V. Bocci, G. Chiodi, M. Cremonesi, E. De Lucia, M. E. Ferrari, P. M. Frallicciardi, C. M. Grana, *et al.*, “Toward radioguided surgery with β- decays: Uptake of a somatostatin analogue, dotatoc, in meningioma and high-grade glioma”, *Journal of Nuclear Medicine*, vol. 56, no. 1, pp. 3–8, 2015.

[12] J. T. Bushberg and J. M. Boone, *The essential physics of medical imaging*. Lippincott Williams & Wilkins, 2011.

[13] M. Tsuchimochi and K. Hayama, “Intraoperative gamma cameras for radioguided surgery: Technical characteristics, performance parameters, and clinical applications”, *Physica Medica*, vol. 29, no. 2, pp. 126–138, 2013.

[14] S. Vidal-Sicart, M. Rioja, P. Paredes, M. Keshtgar, and R. V. Olmos, “Contribution of perioperative imaging to radioguided surgery”, *Quarterly Journal of Nuclear Medicine and Molecular Imaging*, vol. 58, no. 2, pp. 140–160, 2014.

[15] M. Noguchi, M. Inokuchi, and Y. Zen, “Complement of peritumoral and subareolar injection in breast cancer sentinel lymph node biopsy”, *Journal of surgical oncology*, vol. 100, no. 2, pp. 100–105, 2009.

[16] J.-F. Rodier, M. Velten, M. Wilt, P. Martel, G. Ferron, V. Vaini-Elies, H. Mignotte, A. Brémond, J.-M. Classe, F. Dravet, *et al.*, “Prospective multicentric randomized study comparing periareolar and peritumoral injection of radiotracer and blue dye for the detection of sentinel lymph node in breast sparing procedures: Fransenode”, *Journal of clinical oncology*, vol. 25, no. 24, pp. 3664–3669, 2007.

[17] F. Daghighian, J. C. Mazziotta, E. J. Hoffman, P. Shenderov, B. Eshaghian, S. Siegel, and M. E. Phelps, "Intraoperative beta probe: A device for detecting tissue labeled with positron or electron emitting isotopes during surgery", *Medical physics*, vol. 21, no. 1, pp. 153–157, 1994.

[18] S. Bonzom, L. Menard, S. Pitre, M. Duval, R. Siebert, S. Palfi, L. Pinot, F. Lefebvre, and Y. Charon, "An intraoperative beta probe dedicated to glioma surgery: Design and feasibility study", *IEEE Transactions on Nuclear Science*, vol. 54, no. 1, pp. 30–41, 2007.

[19] E. S. Camillocci, G. Baroni, F. Bellini, V. Bocci, F. Collamati, M. Cremonesi, E. De Lucia, P. Ferroli, S. Fiore, C. Grana, *et al.*, "A novel radioguided surgery technique exploiting β- decays", *Scientific reports*, vol. 4, p. 4401, 2014.

[20] F. Collamati, V. Bocci, P. Castellucci, M. De Simoni, S. Fanti, R. Faccini, A. Giordano, D. Maccora, C. Mancini-Terracciano, M. Marafini, *et al.*, "Radioguided surgery with β radiation: A novel application with ga 68", *Scientific reports*, vol. 8, no. 1, pp. 1–9, 2018.

[21] S. Vidal-Sicart, R. V. Olmos, O. Nieweg, R. Faccini, M. Grootendorst, H. Wester, N. Navab, B. Vojnovic, H. van der Poel, S. Martınez-Román, *et al.*, "From interventionist imaging to intraoperative guidance: New perspectives by combining advanced tools and navigation with radio-guided surgery", *Revista Española de Medicina Nuclear e Imagen Molecular (English Edition)*, vol. 37, no. 1, pp. 28–40, 2018.

[22] N. D'Ascenzo, P. Marrocchesi, C. Moon, F. Morsani, L. Ratti, V. Saveliev, A. S. Navarro, and Q. Xie, "Silicon avalanche pixel sensor for high precision tracking", *Journal of Instrumentation*, vol. 9, no. 03, p. C03027, 2014.

[23] L. Pancheri, D. Stoppa, and G.-F. Dalla Betta, "Characterization and modeling of breakdown probability in sub-micrometer cmos spads", *IEEE Journal of Selected Topics in Quantum Electronics*, vol. 20, no. 6, pp. 328–335, 2014.

[24] L. Pancheri, A. Ficorella, P. Brogi, G. Collazuol, G.-F. Dalla Betta, P. Marrocchesi, F. Morsani, L. Ratti, A. Savoy-Navarro, and A. Sulaj, "First demonstration of a two-tier pixelated avalanche sensor for charged particle detection", *IEEE Journal of the Electron Devices Society*, vol. 5, no. 5, pp. 404–410, 2017.

[25] P. Brogi, G. Bigongiari, C. Checchia, G. Collazuol, G. Dalla Betta, A. Ficorella, P. Marrocchesi, F. Morsani, M. Musacci, G. Torilla, *et al.*, "Apix, a two-tier avalanche pixel sensor for digital charged particle detection", *Nuclear Instruments and Methods in Physics*

Research Section A: Accelerators, Spectrometers, Detectors and Associated Equipment, p. 162 546, 2019.

[26] A. Ficorella, L. Pancheri, P. Brogi, G. Collazuol, G.-F. Dalla Betta, P. S. Marrocchesi, F. Morsani, L. Ratti, and A. Savoy-Navarro, “Crosstalk characterization of a two-tier pixelated avalanche sensor for charged particle detection”, *IEEE Journal of Selected Topics in Quantum Electronics*, vol. 24, no. 2, pp. 1–8, 2017.

[27] P. Marrocchesi, P. Brogi, G. Bigongiari, C. Checchia, G. Collazuol, G. Dalla Betta, A. Ficorella, L. Lodola, F. Morsani, M. Musacci, *et al.*, “Apix: A geiger-mode avalanche digital sensor for particle detection”, in *2017 IEEE Nuclear Science Symposium and Medical Imaging Conference (NSS/MIC)*, IEEE, 2017, pp. 1–4.

[28] L. Ratti, P. Brogi, G. Collazuol, G.-F. Dalla Betta, A. Ficorella, L. Lodola, P. Marrocchesi, S. Mattiazzo, F. Morsani, M. Musacci, *et al.*, “Dark count rate degradation in cmos spads exposed to x-rays and neutrons”, *IEEE Transactions on Nuclear Science*, vol. 66, no. 2, pp. 567–574, 2019.

[29] F. Collamati, D. Maccora, S. Alfieri, V. Bocci, A. Cartoni, A. Collarino, M. De Simoni, M. Fischetti, I. Fratoddi, A. Giordano, *et al.*, “Radioguided surgery with β- radiation in pancreatic neuroendocrine tumors: A feasibility study”, *Scientific reports*, vol. 10, no. 1, pp. 1–10, 2020.

[30] M. Bagliesi, C. Avanzini, G. Bigongiari, A. Caldarone, R. Cecchi, M. Kim, P. Maestro, P. Marrocchesi, F. Morsani, and R. Zei, “Front-end electronics with large dynamic range for space-borne cosmic ray experiments”, *Nuclear Physics B-Proceedings Supplements*, vol. 172, pp. 156–158, 2007.

[31] P. Marrocchesi, C. Avanzini, M. Bagliesi, A. Basti, K. Batkov, G. Bigongiari, A. Caldarone, R. Cecchi, M. Kim, T. Lomtatze, *et al.*, “Beam test results of pixelated silicon sensors for the charge identification of cosmic rays”, in *Proceedings of the 30th International Cosmic Ray Conference, ICRC 2007*, Citeseer, 2007, pp. 321–324.

[32] P. S. Marrocchesi, O. Adriani, C. Avanzini, M. G. Bagliesi, A. Basti, K. Batkov, G. Bigongiari, L. Bonechi, R. Cecchi, M. Y. Kim, *et al.*, “A silicon array for cosmic-ray composition measurements in calet”, *Journal of the Physical Society of Japan*, vol. 78, no. Suppl. A, pp. 181–183, 2009.

[33] P. Maestro, M. Bagliesi, G. Bigongiari, S. Bonechi, M. Kim, and P. Marrocchesi, “Beam test performance of a pixelated silicon array for the charge identification of cosmic rays”, *Nuclear Instruments and Methods in Physics Research Section A: Accelerators, Spectrometers, Detectors and Associated Equipment*, vol. 679, pp. 7–13, 2012.

[34] P. Marrocchesi, O. Adriani, Y. Akaike, M. Bagliesi, A. Basti, G. Bigongiari, S. Bonechi, M. Bongi, M. Kim, T. Lomtadze, *et al.*, “Beam test performance of a scintillator-based detector for the charge identification of relativistic ions”, *Nuclear Instruments and Methods in Physics Research Section A: Accelerators, Spectrometers, Detectors and Associated Equipment*, vol. 659, no. 1, pp. 477–483, 2011.

[35] M. Bagliesi, C. Avanzini, G. Bigongiari, R. Cecchi, M. Kim, P. Maestro, P. Marrocchesi, and F. Morsani, “A custom front-end asic for the readout and timing of 64 sipm photosensors”, *Nuclear Physics B-Proceedings Supplements*, vol. 215, no. 1, pp. 344–348, 2011.

[36] P. S. Marrocchesi, M. G. Bagliesi, S. Bonechi, G. Bigongiari, P. Brogi, G. Collazuol, A. Ferri, P. Maestro, C. Piemonte, A. Sulaj, *et al.*, “Charged particle detection with nuv-sensitive sipm in a beam of relativistic ions”, *IEEE Transactions on Nuclear Science*, vol. 61, no. 5, pp. 2786–2793, 2014.

[37] P. Marrocchesi, M. Bagliesi, A. Basti, G. Bigongiari, S. Bonechi, P. Brogi, C. Checchia, G. Collazuol, P. Maestro, F. Morsani, *et al.*, “Digital fdirc: A focused differential internal reflection cherenkov imaged by sipm arrays”, *Nuclear Instruments and Methods in Physics Research Section A: Accelerators, Spectrometers, Detectors and Associated Equipment*, vol. 824, pp. 635–639, 2016.

[38] M. Musacci, G. Bigongiari, P. Brogi, C. Checchia, G. Collazuol, G.-F. Dalla Betta, A. Ficorella, P. Marrocchesi, S. Mattiazzo, F. Morsani, *et al.*, “Radiation tolerance characterization of geiger-mode cmos avalanche diodes for a dual-layer particle detector”, *Nuclear Instruments and Methods in Physics Research Section A: Accelerators, Spectrometers, Detectors and Associated Equipment*, vol. 936, pp. 695–696, 2019.

[39] P. Brogi, G. Bigongiari, C. Checchia, G. Collazuol, G. Dalla Betta, A. Ficorella, P. Marrocchesi, F. Morsani, M. Musacci, G. Torilla, *et al.*, “Apix, a two-tier avalanche pixel sensor for digital charged particle detection”, *Nuclear Instruments and Methods in Physics Research Section A: Accelerators, Spectrometers, Detectors and Associated Equipment*, vol. 958, p. 162 546, 2020.